The Continuous Wavelet Transform in MRS

Aimamorn Suvichakorn,[1] Christina Lemke,[2]
Adalberto Schuck Jr.[3] and Jean-Pierre Antoine [4]

Institut de Recherche en Mathématique et Physique
Université catholique de Louvain
B-1348 Louvain-la-Neuve, Belgium

April 19, 2011

[1]Former FAST ER fellow, *E-mail:* aimamorn@gmail.com
[2]Former FAST ER fellow, *E-mail:* christina.lemke@gmail.com
[3]Permanent address: Electrical Eng. Department (DELET), Federal University of Rio Grande do Sul (UFRGS). Av. Oswaldo Aranha, 103, Porto Alegre, RS, CEP 90.035-190, Brazil; *E-mail:* schuck@ufrgs.br
[4]*E-mail:* jean-pierre.antoine@uclouvain.be

Abstract

This tutorial text reviews some applications of the Continuous Wavelet Transform (CWT) in Magnetic Resonance Spectroscopy (MRS), focusing on the problems of spectral line estimation, namely, apodization, random noise, baseline, solvent peak, nonstandard lineshapes. First, we use a standard wavelet, namely the Morlet wavelet. Next, we introduce a new type of wavelet, derived from the autocorrelation function of a model signal. Finally, we apply this new technique for constructing adapted wavelets, generated from the metabolite data themselves. A short compendium on the basics of the CWT and some explicit numerical programs are given in two Appendices.

Contents

Chapter 1

Introduction

In Magnetic Resonance Spectroscopy (MRS), a signal is acquired when the nuclei in a substance are excited by a radio-frequency pulse and re-radiate it. This results in a decaying wave, which has, in the simplest case, a so-called Lorentzian lineshape in the frequency domain. The frequency of each peak of the signal depends upon the nucleus and is therefore typical for each substance. The amplitude of the peak in the time domain, i.e., its area in the frequency domain, depends on the amount of those nuclei, that is, the concentration of the substance. Therefore, a good quantification technique is essential for the interpretation of the MRS signals.

For this purpose, a number of techniques have been proposed, which work either in the time domain (see Poullet et al. (2008) for a review) or in the frequency domain (see Mierisov and Ala-Korpela (2001) for a review). However, there also exist techniques that analyse a signal in the two domains simultaneously and are therefore more efficient than, say, the Fourier transform, which gives only spectral information. The result is a time-scale and or a time-frequency representation, such as provided by the wavelet transform (WT) and the Short-Time Fourier transform (STFT). In addition, both transforms are local, in the sense that a small perturbation of a signal which may occur during the data acquisition will result only in a small, local modification of the transform.

Figure 1.1 (a) illustrates the characteristics of an *in vivo* MRS spectrum. Although it can give useful information about the concentration of the metabolites, the signal also contains noise, solvent peaks, and a baseline which appears as a broad pattern frequency response due to contributions from large molecules. Besides, the peaks of metabolites overlap in places such as those in the blocks A and B. The assumption of Lorentzian profile is also dubious. On the other hand, Figure 1.1 (b) demonstrates the benefits of seeing the signal in both time and frequency domains. The similar representation of frequency (or scale) of the signal along the y-axis and time along the x-axis with the amplitude displayed in shades will be used throughout this e-book. The standard Morlet wavelet used in this example is able to zoom in and reveal more details of the overlapping block B. It can also clearly distinguish the signal and noise which appears randomly in time. The illustration inspires us to exploit more the benefits of the time-frequency representation in MRS quantification.

In fact, a number of wavelet-based techniques have been proposed for spectral line estimation in MRS, including the continuous wavelet transform (Guillemain et al., 1992; Delprat et al., 1992; Serrai et al., 1997) and the wavelet packet decomposition (Mainardi et al., 2002). Among the various possibilities, we will concentrate our discussion on the continuous wavelet transform (CWT). We will begin with the well-known Morlet wavelet. The latter, being complex, is efficient at detecting characteristic *frequencies* in a signal, which is exactly our purpose here. Next, we introduce a new class of wavelets, derived from the autocorrelation function of a model signal.

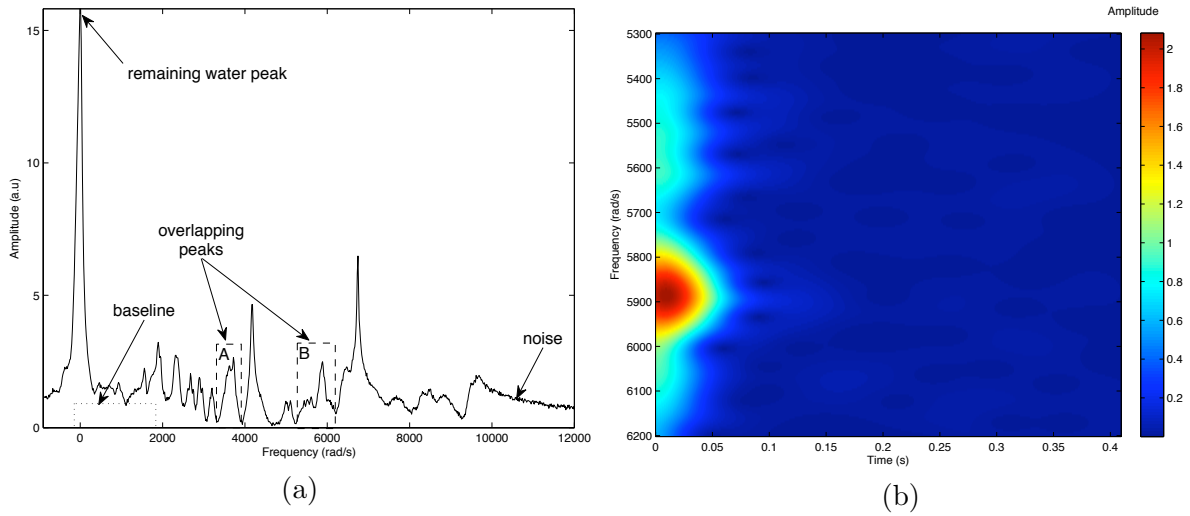

(a) (b)

Figure 1.1: (a) The *in vivo* MRS spectrum from a rat's brain at 9.4T; (b) the Morlet WT representation of block B.

Finally, we apply this new technique for constructing adapted wavelets, derived from the metabolite data themselves. Here we face the additional problem that data are by necessity discrete, and thus also their autocorrelation function. Therefore an extra step, based on interpolation, is needed for using such discrete wavelets for a *continuous* wavelet transform. The outcome is that these wavelets look promising for the analysis of MRS signals. In particular, they are able to detect without ambiguity the presence of a given metabolite in a superposition of several metabolites and/or lipids.

Note that band-limited wavelets matching specific signal spectra (not necessarily NMR spectra) have been designed e.g. in (Chapa and Rao, 2000) and (Bahrampour et al., 2008), then adapted to the *discrete* wavelet transform (DWT), using an orthonormal multiresolution scheme, which is a strong restriction. On the other hand, NMR spectra have been analyzed in (Neue, 1996) with a standard orthonormal DWT. But in both cases, using the DWT leads to dificulties, because the technique is not adapted to the analysis process (Daubechies, 1992; Torrésani, 1995; Antoine et al., 2004). With our approach, on the contrary, we have much more freedom, since we use the CWT. We can choose the best analysing wavelets for the problem at hand and we do not need them to be orthonormal. We will elaborate on this point in Section A.4.

For the convenience of the readers we have collected in Appendix A the basic features and properties of the CWT. Then Appendix B presents several MATLAB© programs for computing various quantities of the theory. Note that all wavelet calculations have been performed by our own wavelet toolbox, called YAWTb (Jacques et al., 2007) and can be downloaded from `http://rhea.tele.ucl.ac.be`. Readers who want to perform time-domain analysis can also download the jMRUI Graphical User Interface from our Marie Curie FAST project's website `http://www.fast-mrs.eu`. The current version includes the Gabor transform (Antoine et al., 2001), another time-frequency technique developed by our group.

Chapter 2

Wavelet analysis in MRS: Standard wavelets

In this chapter, we introduce the standard wavelet-based method to estimate parameters that together enable reconstuction of a measured MRS signal (spectral line) c onsisting of a single damped sinusoid. The method is studied in various situations resembling real MRS environments, e.g. discrete implementation, baseline, solvent peaks, non-Lorentzian lineshapes and noise. The technique can be applied in *in vivo* MRS practice which usually pertains to estimation of concentrations (only) of metabolites, under some limitations such as edge effects and overlapping frequencies, however. In Section 2.2 we discuss how to cope with these limitations and in Section 2.3 we present how the standard Morlet wavelet works in the real life environment.

2.1 Spectral line estimation

The WT of a signal $s(t)$ with respect to a basic wavelet $\psi(t)$ is

$$\begin{aligned} S(\tau, a) &= \frac{1}{\sqrt{a}} \int \overline{\psi\left(\frac{t-\tau}{a}\right)}\, s(t)\, \mathrm{d}t \\ &= \frac{1}{2\pi}\sqrt{a} \int \overline{\Psi(a\omega)}\, S(\omega)\, e^{i\omega\tau}\, \mathrm{d}\omega, \end{aligned} \tag{2.1}$$

where $S(\omega)$ is the asymmetric Fourier transform of the signal, $a \in \mathbb{R}$ is a dilation parameter that characterises the frequency of the signal (since $1/a$ is essentially a frequency), $\tau \geqslant 0$ is a translation parameter that indicates the localisation in time and $\overline{\Psi(a\omega)}$ is the complex conjugate of the (scaled) Fourier transform of $\psi(t)$. We can think of the basic wavelet as a window which slides through the signal, giving the information at instantaneous time τ. As a result, the WT becomes a function of both time and frequency (scale), allowing us to see the information in the two domains simultaneously. Its window is also dilated by a such that a small a corresponds to a high frequency of the signal, and *vice versa*. This means that at high frequency the WT can localise individual peaks better than the Short-Time Fourier Transform (STFT), which has a fixed window and tends to smear these information. For more details, see Appendix A.1.

Guillemain et al. (1992) have proposed a technique based on the CWT that can extract the information from MRS signals directly without any decomposition or pre-processing. The technique proceeds in two st : (i) detection of the frequency of the peaks in MRS signals and (ii) characterisation at each detected frequency.

Detection

Let us denote $S_a(\tau) \equiv S(\tau, a)$ as the WT at a particular value of a and represent it in terms of modulus $|S_a(\tau)|$ and phase $\Phi_a(\tau) := \arg S(\tau, a)$, namely,

$$S_a(\tau) = |S_a(\tau)| e^{i\Phi_a(\tau)}, \tag{2.2}$$

with an instantaneous frequency

$$\begin{aligned} \Omega_a(\tau) &= \frac{\mathrm{d}}{\mathrm{d}\tau}\Phi_a(\tau) \\ &= \frac{\mathrm{d}}{\mathrm{d}\tau}\mathrm{Im}[\ln S_a(\tau)] \\ &= \mathrm{Im}\left[\frac{1}{S_a(\tau)}\frac{\mathrm{d}}{\mathrm{d}\tau}S_a(\tau)\right]. \end{aligned} \tag{2.3}$$

Notice that $\Omega_a(\tau)$ can be used to estimate the frequencies of the signal. For instance, given a two-frequency signal $s(t)$ defined by

$$s(t) = A_1 e^{i\omega_1 t} + A_2 e^{i\omega_2 t}, \tag{2.4}$$

that is, $S(\omega) = 2\pi A_1 \delta(\omega - \omega_1) + 2\pi A_2 \delta(\omega - \omega_2)$, its CWT is

$$\begin{aligned} S(\tau, a) &= \sqrt{a}\int \left[A_1\delta(\omega-\omega_1)\Psi(a\omega)e^{i\omega\tau} + A_2\delta(\omega-\omega_2)\Psi(a\omega)e^{i\omega\tau}\right]\,\mathrm{d}\omega \\ &= \sqrt{a}\left[A_1\Psi(a\omega_1)e^{i\omega_1\tau} + A_2\Psi(a\omega_2)e^{i\omega_2\tau}\right]. \end{aligned} \tag{2.5}$$

Putting $C(a) = \frac{A_2\Psi(a\omega_2)}{A_1\Psi(a\omega_1)}$, we obtain

$$\begin{aligned} \frac{1}{S_a(\tau)}\frac{\mathrm{d}}{\mathrm{d}\tau}S_a(\tau) &= \frac{i\omega_1 A_1\Psi(a\omega_1)e^{i\omega_1\tau} + i\omega_2 A_2\Psi(a\omega_2)e^{i\omega_2\tau}}{A_1\Psi(a\omega_1)e^{i\omega_1\tau} + A_2\Psi(a\omega_2)e^{i\omega_2\tau}} \\ &= i\omega_1\left[\frac{1+\frac{\omega_2}{\omega_1}C(a)e^{i(\omega_2-\omega_1)\tau}}{1+C(a)e^{i(\omega_2-\omega_1)\tau}}\right]. \end{aligned} \tag{2.6}$$

Hence, the instantaneous frequency is

$$\Omega_a(\tau) = \omega_1 \mathrm{Re}\left[\frac{1+\frac{\omega_2}{\omega_1}C(a)e^{i(\omega_2-\omega_1)\tau}}{1+C(a)e^{i(\omega_2-\omega_1)\tau}}\right]. \tag{2.7}$$

For $\tau \to \infty$, it converges toward three different limits, depending on the value of $C(a)$, namely,

$$\Omega_a(\tau\to\infty) = \begin{cases} \omega_1, & \text{if } C(a) \ll 1 \\ \frac{\omega_1+\omega_2}{2}, & \text{if } C(a) = 1. \\ \omega_2, & \text{if } C(a) \gg 1 \end{cases} \tag{2.8}$$

In other words, the instantaneous frequency of the WT of an input signal $s(t)$ will converge into the frequencies of that signal, independently of A_1 or A_2. Thus, the frequencies ω_1 and ω_2 can now be estimated, including the amplitudes A_1 and A_2, respectively.

As an example, Figure 2.1 illustrates how the instantaneous frequencies of a signal can be seen along the scale axis of the WT. Obviously, the instantaneous frequencies converge (along the

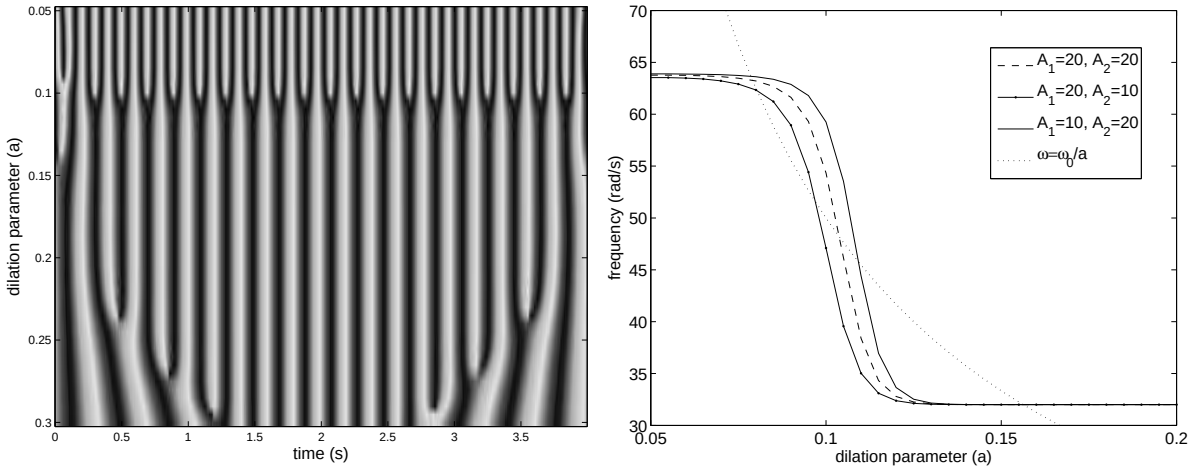

(a) (b)

Figure 2.1: (a) Phase of the Morlet WT of $s(t) = A_1 e^{i32t} + A_2 e^{i64t}$ which clearly shows two different values along the scale axis, and also some distortion at edge of the time axis; (b) its instantaneous frequency as a function of scale a when Eq. (2.3) is used. It converges to the two frequencies of $s(t)$. Here the parameters of the Morlet WT are $\sigma = 1, \omega_0 = 5$ rad/s, sampling frequency $F_s = 256$ s^{-1}, data length $L = 1024$ points.

scale axis) towards two values: 32 and 64 rad/s, which are the two frequencies of the signal. In addition, knowing the dilation parameter a that gives $C(a) = 1$, e.g. $\Omega_a = (32 + 64)/2 = 48$ rad/s in this example, the information on the ratio between A_2 and A_1 can be derived, and therefore their values. Although the Morlet wavelet (A.9) with $\sigma = 1$ and $\omega_0 = 5$ rad/s is used in this illustration, the amplitude and frequencies of the signal can be calculated by using *any* progressive wavelet function.

For a signal with n peaks, the lowest Ω_a is the most obvious, as seen in Figure 2.2. In such cases we can remove the lowest frequency component from the signal, i.e. by multiplying it with $e^{-i\omega t}$, to enhance the higher frequencies. The derived Ω_a then becomes the difference between the lowest frequency and the second-lowest. The process can continue iteratively as long as the difference between the two frequencies is not too small. However, the derivation of amplitude described above is applicable only to a two-frequency signal and therefore we need another methodology for the n-frequency signal.

Characterisation

By now, we can see that there is a relation between the frequency of a signal and the instantaneous phase of its wavelet coefficients. Next, let us consider an MRS signal with a Lorentzian damping function, namely,

$$s_L(t) = Ae^{-Dt}e^{i(\omega_s t+\varphi)} \;\Leftrightarrow\; S_L(\omega) = 2\pi A e^{i\varphi}\delta(\omega - (\omega_s + iD)), \tag{2.9}$$

where D and φ denote the damping factor and the phase of the signal.[1] Clearly, this Lorentzian profile is characterised by two parameters: the damping factor D and the amplitude A. Using a

[1]Here we use the Fourier transform formula $\mathcal{F}\{e^{i\alpha t}\} = 2\pi\delta(\omega - \alpha)$. Many MRS publications use instead the relation $\mathcal{F}\{e^{-\alpha t}\theta(t)\} = (\alpha + i\omega)^{-1}$, where θ is the Heaviside function, but we prefer the former, because of the simplification due to the Dirac delta function $\delta(\omega)$. Note that, in both cases, the derivation requires the parameter α to be complex (either $\alpha = \omega_s + iD$ or $\alpha = D - i\omega_s$).

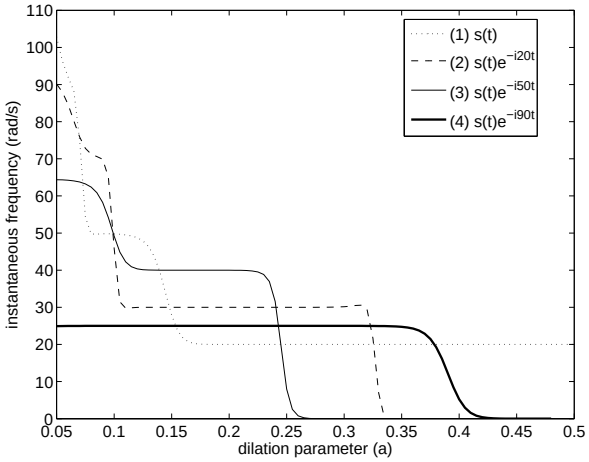

Figure 2.2: The instantaneous frequency of $s(t) = \exp(i20t) + \exp(i50t) + \exp(i90t) + \exp(i115t)$, as derived by the Morlet wavelet, has the lowest frequency as the most obvious. After subtracting the lowest frequency component, the instantaneous frequency then shows the frequency difference between the lowest and the second lowest ones. The second-lowest frequency can then be derived. The process can continue iteratively as long as the frequency difference is not too small.

Morlet function scaled by a dilation parameter a (we omit the negligible correction term, see Eq. (A.9)), namely,

$$\Psi_M(a\omega) = e^{-\frac{\sigma^2}{2}(a\omega-\omega_0)^2}, \tag{2.10}$$

the modulus of its Morlet WT is maximum along the scale $a_r = \omega_0/\omega_s$, given that $a \in \mathbb{R}$ and the assumption that $\omega_s \gg D$. This can be seen as a *horizontal ridge* in the (τ, a) plane. Substitute $S_L(\omega)$ and $\Psi_M(a\omega)$ in Eq. (2.1) we have the Morlet WT of the Lorentzian profile at the scale a_r, namely,

$$S_{a_r}(\tau) \;=\; \sqrt{a_r}\exp\left(\frac{\sigma a_r D}{\sqrt{2}}\right)^2 s_L(\tau), \tag{2.11}$$

identical to the signal $s_L(t)$ multiplied by a coefficient. This shows that the Morlet WT can *see* the lineshape at each frequency separately. The Gaussian function of the Morlet WT (as well as the Gaussian-windowed STFT called the Gabor Transform) is also known to have the optimal window shape that gives the least Fourier uncertainty in time and frequency spaces. In addition, Eq. (2.11) allows us to derive the damping factor for the Lorentzian profile as follows:

$$\begin{aligned} |S_{a_r}(\tau)| &= \sqrt{a_r}\exp\left(\frac{\sigma a_r D}{\sqrt{2}}\right)^2 |s_L(\tau)| \\ \ln|S_{a_r}(\tau)| &= \frac{1}{2}\ln a + \left(\frac{\sigma a_r D}{\sqrt{2}}\right)^2 + \ln A - D\tau \\ D &= -\frac{\partial}{\partial\tau}\ln|S_{a_r}(\tau)|. \end{aligned} \tag{2.12}$$

Knowing D can now lead to the estimation of the amplitude resonance A of the signal by

$$A = \; |s(t)|e^{Dt}. \tag{2.13}$$

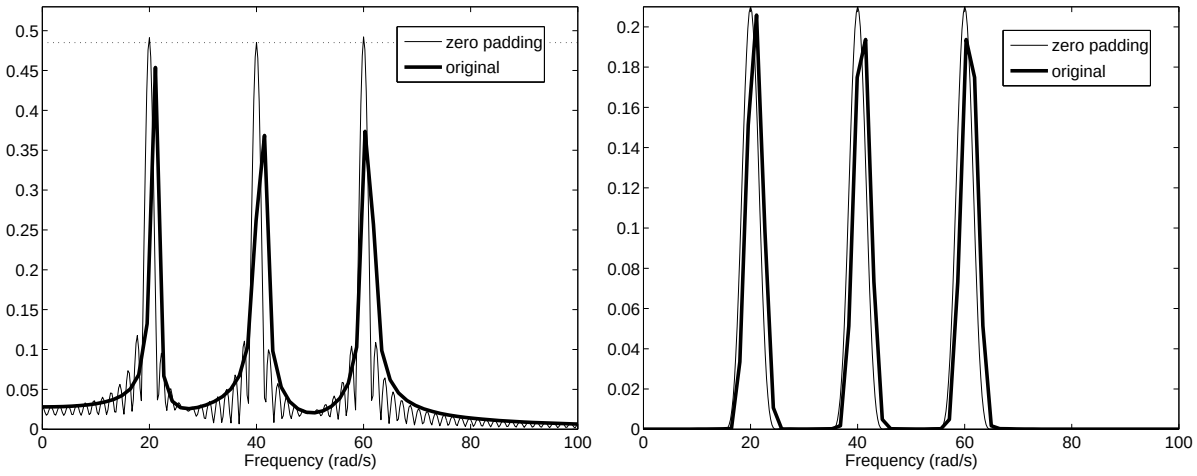

(a) (b)

Figure 2.3: (a) The discrete Fourier transform of $s(t) = \sin(20t) + \sin(40t) + \sin(60t)$ before and after zero padding. The amplitude at each frequency is well resolved; (b) the same signal after using a tapering window to suppress the ringing effect.

As $S_{a_r}(\tau)$ is a function of time, therefore the derived D is also a function of time. This is beneficial for analysing any signals that do not have a steady damping function. In addition, by Eq. (2.3), we have

$$\Omega_{a_r}(\tau) = \frac{\partial}{\partial \tau} \Phi a_r(\tau) = \omega_s.$$

In other words, the derivative of the phase at the scale a_r of the Morlet WT is ω_s. This is already observed in Figure 2.1, i.e., the instantaneous frequency Ω_a intersects the line ω_0/a twice at $a = \omega_0/\omega_s$ where ω_s=32 and 64 rad/s are the frequencies of the signal. The equation is useful for analysing an n-frequency signal; it tells the actual frequencies of the signal and indicates the scale a that we should consider. In addition, if the frequencies are *sufficiently* far away from each other that $\overline{\Psi(a\omega)}$ treats each spectral line independently (Barache et al., 1997), the amplitude at each frequency can thus be derived. The phase of the signal $\varphi \in (-\pi, \pi)$ can also be derived from the phase of the WT, if needed.

In the following sections, we will study the performance of the WT, in particular with a Morlet wavelet, on five major aspects in MRS: apodisation, baseline, solvent, and non-Lorentzian lineshapes and noise.

2.1.1 Apodisation

In general, using the Fourier transform to analyse a signal in the frequency domain can lead to erroneous results due to discrete implementation, e.g. aliasing,[2] picket-fence effect,[3] etc. Basically,

[2] *Aliasing* is the time-domain distortion that occurs when the signal has frequencies larger than half of the sampling rate. To avoid aliasing, the sampling rate should be greater than twice the highest frequency presented in the signal, known as the Nyquist sampling rate.

[3] *Picket-fence effect* is the effect that normally occurs when using the discrete Fourier transform on a finite interval, since it can observe the spectrum only at particular frequencies. Some major peaks that lie between two of the frequencies might not be detected. In addition, the peak does not lie at the correct frequency if the frequency is not an integer multiple of the sampling period. To reduce this effect, the time signal should be long enough. Likewise, zeros can also be added at the end of the time signal in order to change its period, increase the frequency resolution and shift the frequencies to points where they can be observed.

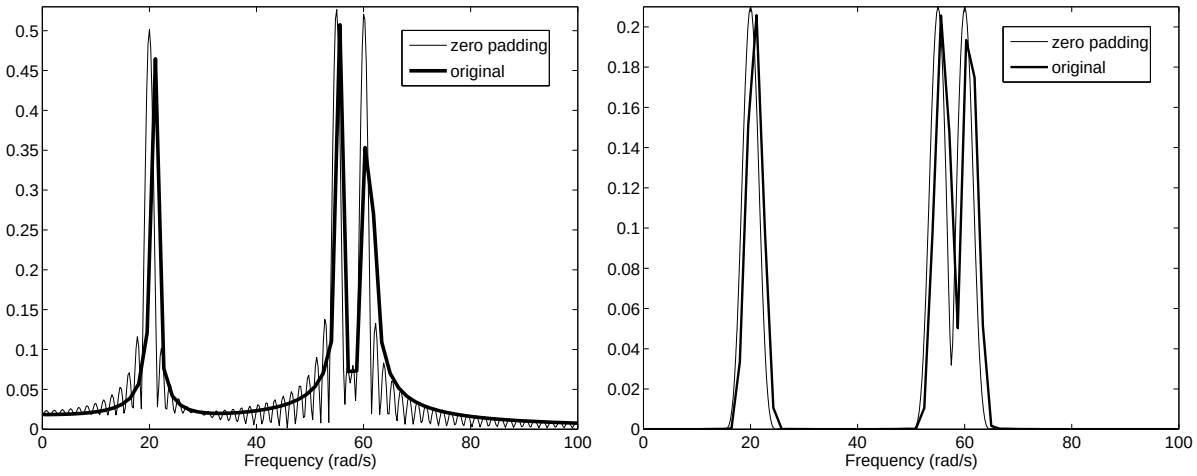

(a) (b)

Figure 2.4: (a) The discrete Fourier transform of $s(t) = \sin(20t) + \sin(55t) + \sin(60t)$ before and after zero padding. The amplitude is more distorted when the frequencies are close to each other; (b) the same signal after using a tapering window.

this means that the sampling frequency (F_s) and the length of the signal (L) need to be carefully selected. As illustrated in Figure 2.3 (a), the amplitude and the lineshape at each frequency of the signal $s(t) = \sin(20t)+\sin(40t)+\sin(60t)$ are corrupted when the sampling points in the frequency domain are equal to those in the time domain. The frequency resolution can be increased by zero-padding the signal. The true amplitudes are then revealed. However, zero-padding also gives rise to a ringing effect, which is another consequence of a finite data set (this is called a *boundary effect*, see Appendix A.1). The problem becomes more severe when two frequencies are close together as seen in Figure 2.4 (a). To reduce this effect, a number of techniques such as decay padding, data-tapering window or wrap-around can be applied (Addison, 2002). Figure 2.3 (b) and Figure 2.4 (b) show that the lineshapes become much better when the Blackman tapering windows are used. Although the amplitudes are decreased, all peaks are visually the same. In MRS, the Gaussian or Lorentzian window is commonly used and the windowing process is known as *apodisation*.

For the CWT, the boundary effect appears as a cone in the (τ, a) plane at the beginning in time (τ) axis and increases linearly with a. This has been noticed in Figure 2.1 (a). However, by using the derived parameters outside this cone, a tapering window is not required. Without any pre-processing, the original profile of the signal is likely to be preserved, giving a true information for analysis. More details about the boundary effect in the WT can be found in Section 2.2.1 (see also Appendix A.1).

2.1.2 Baseline

The baseline corresponds to contributions from large molecules, with a broad pattern frequency response in the MRS spectrum. Thus, it becomes a major obstruction in the quantification of the MRS signals. First, we model the baseline by cubic splines to study the performance of the WT when the baseline is present. As shown in Figure 2.5, the modelled baseline slightly affects the instantaneous frequency derived from the WT at high a (or low frequencies) and has no effect at all at the scale $a_r = \omega_0/\omega_s$. We also used a baseline $B(t)$ modelled by 50 randomly-distributed Lorentzian profiles with a large damping factor. Figure 2.6 shows the resulting signal $s_L(t) + B(t)$

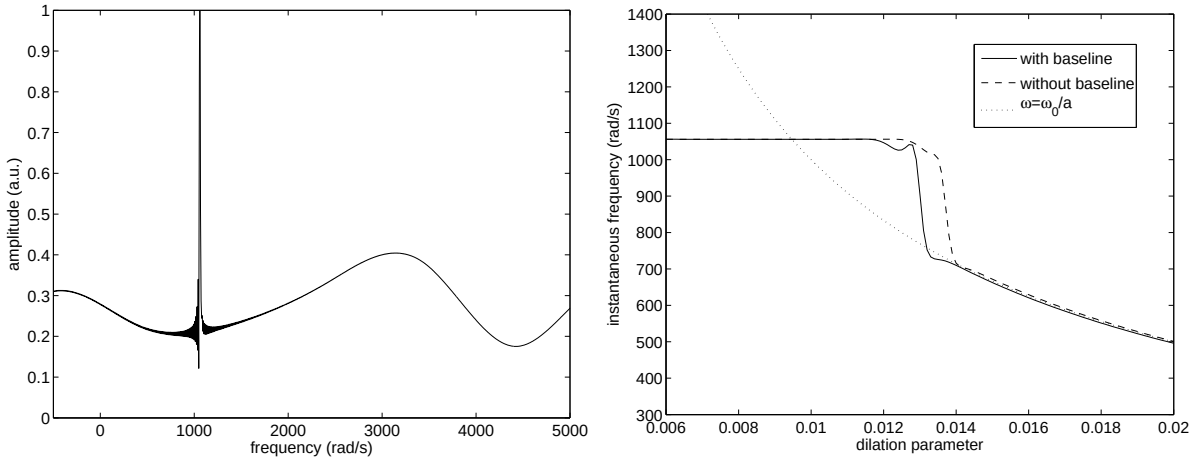

(a) (b)

Figure 2.5: (a) The Fourier transform of a 1056-rad/s signal with a spline-modelled baseline; (b) Its instantaneous frequency derived with the Morlet wavelet ($\omega_0 = 10$ rad/s, $\sigma = 1$) is slightly affected by the baseline at high a (or low frequencies) and has no effect at all at the scale $a_r = \omega_0/\omega_s$.

where $s_L(t) = \exp(-10t)\exp(i\omega_s t)$ is a signal-of-interest with the frequency $\omega_s = 3447$ rad/s and $B(t) = \exp(-50t)[0.2\exp(i\omega_s t) + 0.3\exp(i2000t) + \ldots]$. The first component of $B(t)$ has the same frequency as the signal, in order to imitate the overlap between the baseline and the signal. It is found that the modelled baseline does not prevent an accurate estimation of both the damping factor and the amplitude derived from the Morlet WT, provided one waits until the effect of the baseline has died out (and also the edge effect discussed later). In the example shown here, the waiting time is approximately 0.2s.

This means that the baseline can be assumed to decay faster than the pure signal and affects only the beginning of the transform in the time (τ) axis. Therefore, the method described should still be effective without removing the baseline beforehand. Such an assumption has been widely used in spectroscopic signal processing (Rabeson et al., 2006), where several authors proposed truncation of the initial data points in the time domain, which are believed to contain a major part of the baseline. However, some information of the metabolites could be lost and a strategy for properly selecting the number of data points is needed (see Rabeson et al. (2007) for examples and further references).

Next, in order to study the characteristics of the real baseline by the Morlet wavelet, an *in vivo* macromolecule MRS signal was acquired on a horizontal 4.7T Biospec system (BRUKER BioSpin MRI, Germany). The data acquisition was done by Hélène Ratiney, Adriana Bucur and Sophie Cavassila[4], using the differences in spin-lattice relaxation times (T1) between low molecular weight metabolites and macromolecules (Behar et al., 1994; Cudalbu et al., 2007).

As seen in Figure 2.7, the metabolite-nullified signal from a volume-of-interest (VOI) centralised in the hippocampus of a healthy mouse[5] was a combination of residual water, baseline

[4]CREATIS-LRMN, CNRS UMR 5220, Villeurbanne F-69621, France; Inserm, U630, Villeurbanne F-69621, France; INSA-Lyon, Villeurbanne F-69621, France; Université de Lyon, Lyon, F-69003, France; Université Lyon 1, Villeurbanne F-69622, France.

[5]An Inversion-Recovery module was included prior to the PRESS sequence (echo-time = 20ms, repetition time = 3.5s, bandwidth of 4kHz, 4096 data-points) in order to measure the metabolite-nullified signal. The water signal was suppressed by variable power RF pulses with optimised relaxation delays (VAPOR). All first- and second-order shimming terms were adjusted using the Fast, Automatic Shimming technique by Mapping Along Projections

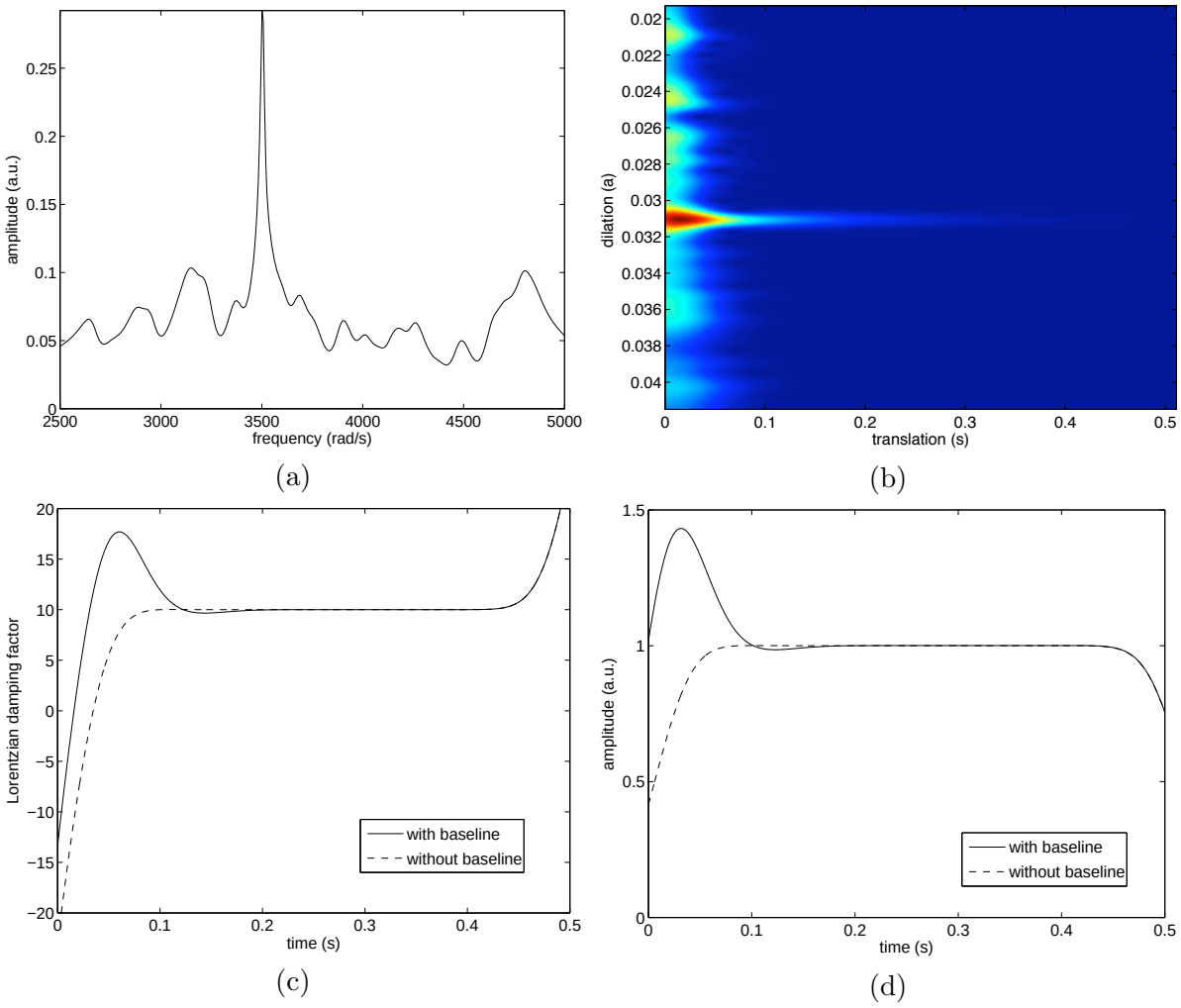

Figure 2.6: (a) The Fourier transform of a 3447-rad/s Lorentzian signal with 50 broad Lorentzian baselines; Its Morlet WT (b) and the derived parameters: damping factor (c) and amplitude (d) are affected by the baselines only at the beginning of time axis. The actual parameters are 10 s^{-1} and 1 a.u. for the damping factor and amplitude, respectively. (The Morlet wavelet parameters are $\omega_0 = 100$ rad/s, $\sigma = 1$).

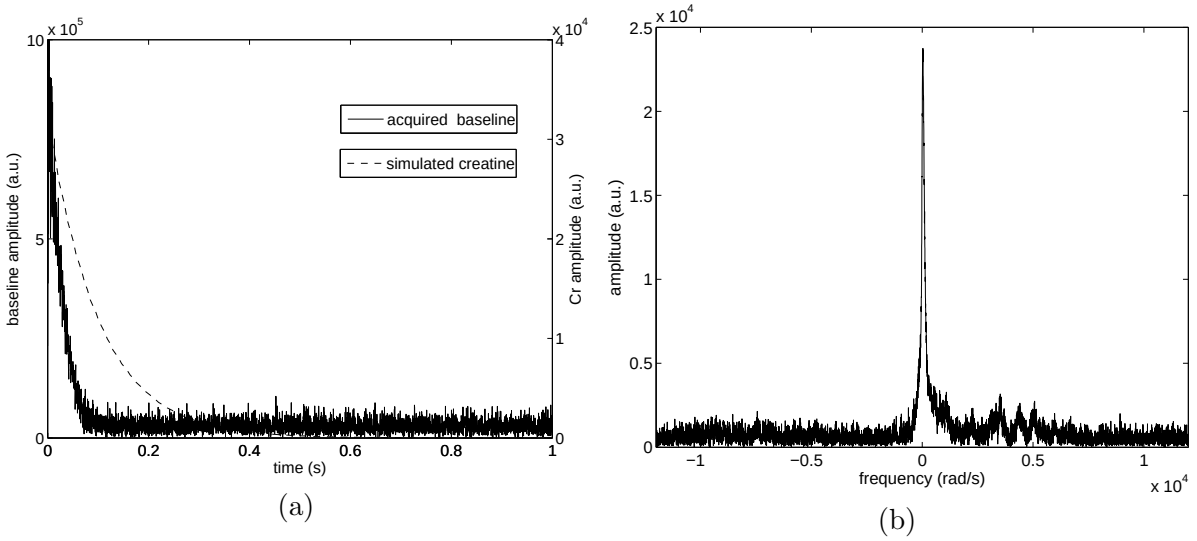

Figure 2.7: The signal of baseline + residual water (a) in time domain; and (b) in frequency domain.

and noise. Compared to the simulated signal of Creatine, whose frequency response and Morlet WT are shown in Figure 2.8, the signal decays much faster, making it suitable to use the Morlet wavelet to analyse the MRS signal as described earlier. For justifying this, the two signals are normalised to the same amplitude and added together. Then the amplitude of the Creatine is derived with the Morlet WT. Next, we multiply the simulated, normalised Creatine by 0.5, 1, 1.5,.... For each of these values, we rederive the amplitude and plot the result in Figure 2.9. The recovery of the (simulated) Creatine at each multiplication, after adding it to the baseline signal, reveals that the amplitude of the metabolite can be correctly derived. We also see that at the beginning of the time axis ($t < 0.2$s), the derived amplitude is less than the actual value due to the boundary effect. Later it is also over-shadowed by noise. Therefore, the time to monitor the amplitude of the metabolite should be properly selected. Although one might expect some left-over Creatine from the nullifying process, the simulated signal of Creatine possibly has a different decaying time from that of the residual Creatine in the baseline, resulting in a correct quantification. Another data set of the baseline[6] acquired at 9.4T has similar characteristics (see Figure 2.10) and does not give very different results.

(FASTMAP) for each VOI ($3 \times 3 \times 3$ mm^3). Inversion time = 700 ms.

[6] received from Cristina Cubaldu, Laboratory for Functional and Metabolic Imaging (LIFMET), Ecole Polytechnique Fédérale de Lausanne (EPFL).

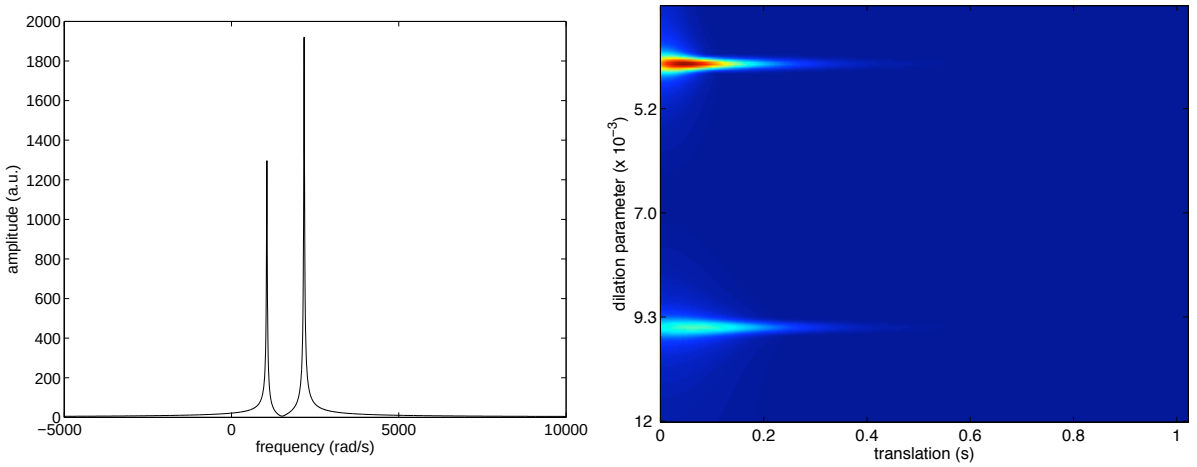

(a) (b)

Figure 2.8: (a) Frequency response of Creatine at 4.7 Tesla and (b) its Morlet WT ($\omega_0 = 10$ rad/s, $\sigma = 1$, $F_s = 4006.41$ s^{-1}). The parameters derived from the Morlet transform are $D = 10$ s^{-1}, $\omega_1 = 1056$ rad/s, $A_1 = 1330$ a.u. and $\omega_2 = 2168$ rad/s, $A_1 = 1965$ a.u.

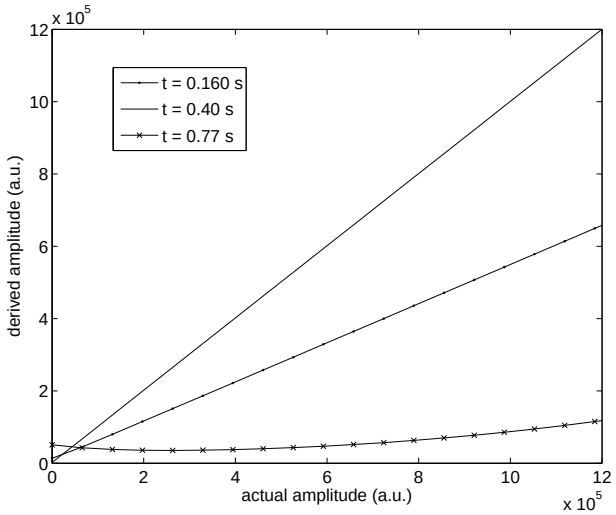

Figure 2.9: Derived amplitude at $\omega = 1056$ rad/s, using $\omega_0 = 100$ rad/s and $\sigma = 1$.

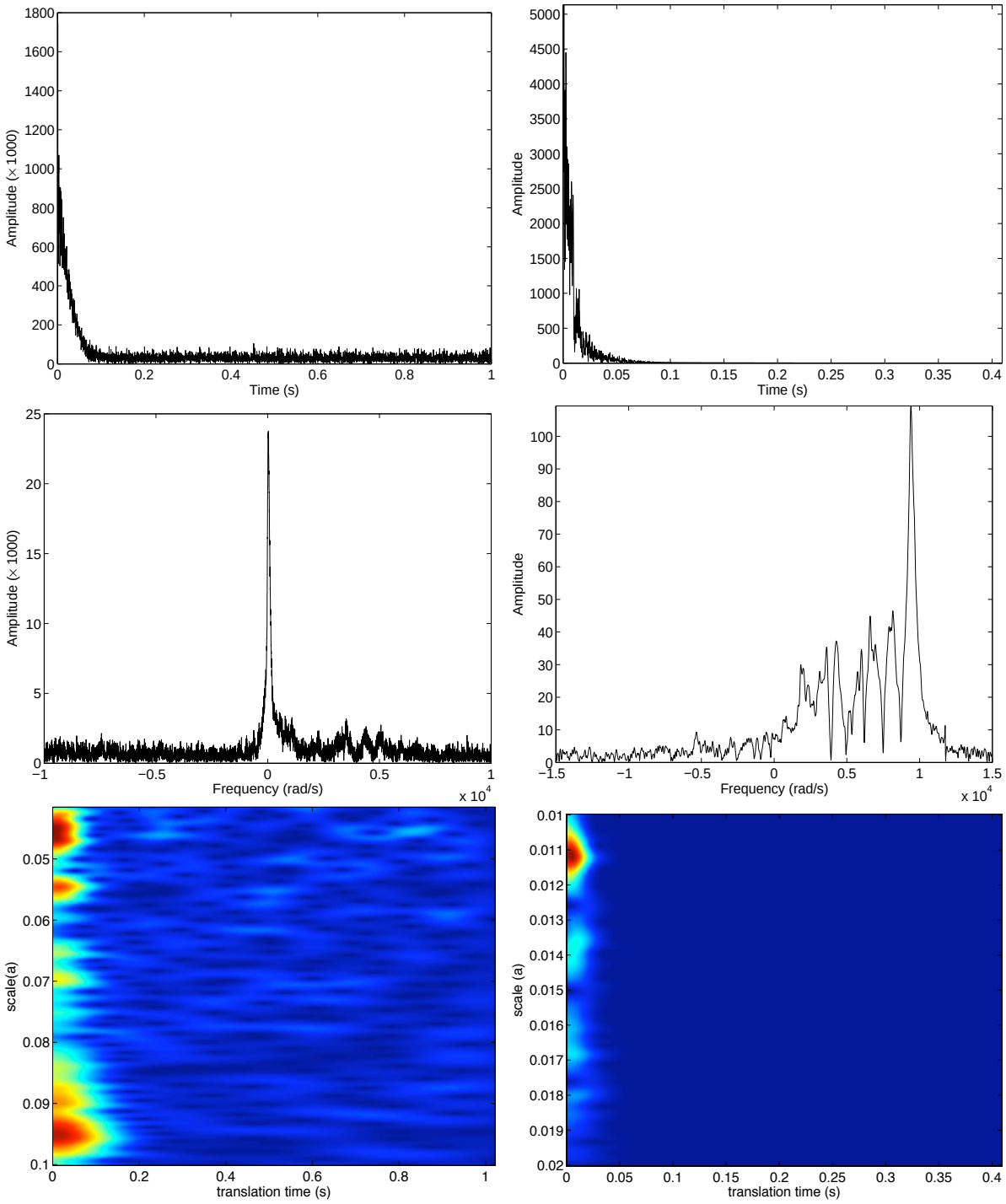

Lyon
(with residual water)

Lausanne
(water suppressed)

Figure 2.10: Macromolecules and their Morlet WT.

2.1.3 Solvent

The Morlet WT sees the signal at each frequency individually, therefore it can work well even if the amplitudes at various frequencies are hugely different, which normally occurs when there is a solvent peak in the signal. As an example, the Morlet WT has been applied to a signal

$$s(t) = 100e^{-8.5t}e^{i32t} + e^{-1.5t}e^{i60t} + e^{-0.5t}e^{i90t} + e^{-t}e^{i120t} + e^{-2t}e^{i150t}, \tag{2.14}$$

as seen in Figure 2.11 (a). This signal has an amplitude of 100 at 32 rad/s and 1 elsewhere. The high amplitude can affect other frequencies if they are close to each other. This is illustrated in Figure 2.11 (b) when a Hann window is applied to the signal in order to separate each frequency. Using the aforementioned method, the amplitude of 1 is derived as 0.980, 0.911, 0.988 and 0.974 respectively. The error ranges within 1.2-8.9 %, without any preprocessing. Note that the Morlet wavelet does not allow us to process at $\omega_s = 0$ ($a \to \infty$), one needs to shift the signal to higher frequency in order to remove any water peaks.

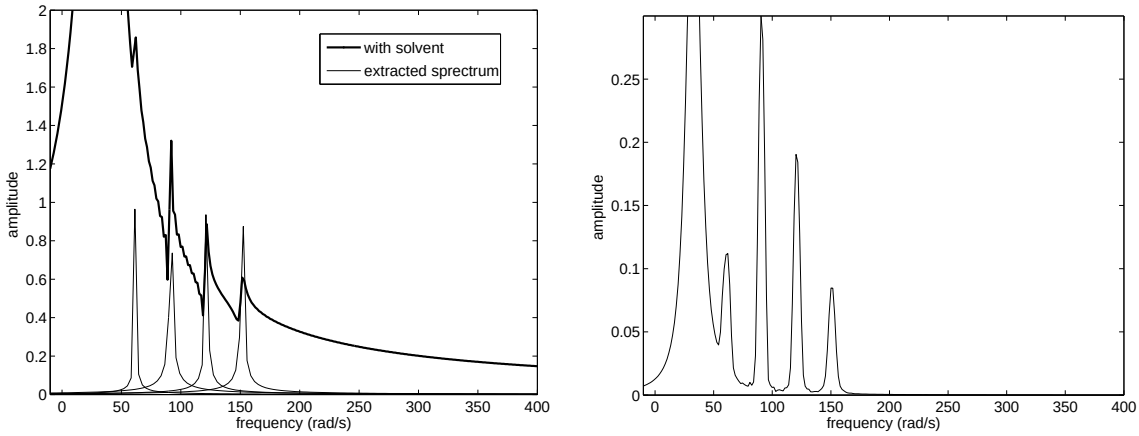

(a) (b)

Figure 2.11: (a) The Fourier transform of a signal with different amplitudes and the spectrum extracted by the Morlet wavelet and (b) by a Hann window.

We can also reconstruct a signal from the Morlet WT coefficients (see Eq. (A.6)). Therefore, in the case where a residual water peak is large and could cover other details such as that in Figure 2.7, the Morlet WT can magnify and unveil these details. The result when applied to this signal is illustrated in Figure 2.12. However, one should be aware that, although the high ω_0 can better separate each frequency component, it can also introduce noise in the result. Therefore, it should be used only for visualisation.

2.1.4 Non-Lorentzian lineshape

The ideal Lorentzian lineshape assumes that the homogeneous broadening is equally contributed from each individual molecule. However, molecules have different relaxation rates in general. In addition, there are other sources, such as inhomogeneous distribution of the molecules, Doppler shift or site differences of molecules in the solution, that can cause the inhomogeneous broadening. These effects are typically modelled by a Gaussian lineshape (Franzen, 2002; Hornak, 1997). Since the inhomogeneous broadening is often significantly larger than the lifetime broadening, the Gaussian lineshape is generally dominant. If the lineshape is intermediate between a Gaussian and a Lorentzian form, the spectrum can be fitted to a convolution of the two functions. Such

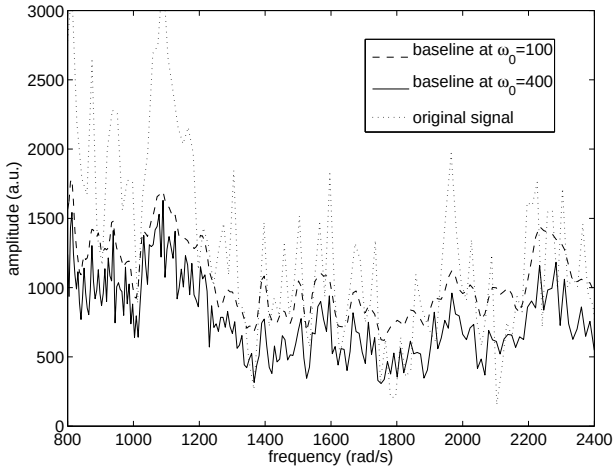

Figure 2.12: The baseline derived by the Morlet WT using the reconstruction formula in Eq. (A.6). The Morlet WT can see the signal at each frequency separately and therefore neglect the effect of solvent peaks.

a lineshape is known as a *Voigt profile* and can be used to resolve the lineshape into either homogeneous (Lorentzian) or inhomogeneous (Gaussian) components.

Next we will explore how the Morlet WT can deal witht the Gaussian and Voigt lineshapes. Consider a pure Gaussian function modulated at the frequency ω_s, namely,

$$s_G(t) = Ae^{-\gamma t^2} e^{i\omega_s t}. \tag{2.15}$$

Its Morlet WT is

$$\begin{aligned} S_G(\tau, a) &= \frac{1}{\sqrt{a}} \int s_G(t)\, \overline{\psi_M\left(\frac{t-\tau}{a}\right)}\, \mathrm{d}t \\ &= \frac{A}{2\pi\sqrt{a}\sigma} \int e^{-\gamma t^2} e^{i\omega_s t} e^{-\left(\frac{t-\tau}{\sqrt{2}\sigma a}\right)^2} e^{-i\omega_0\left(\frac{t-\tau}{a}\right)}\, \mathrm{d}t \\ &= \frac{A}{2\pi\sqrt{a}\sigma} \int e^{-(k_1 t^2 + k_2 t + k_3)}\, \mathrm{d}t, \end{aligned} \tag{2.16}$$

where

$$\begin{aligned} k_1 &= \gamma + \frac{1}{2\sigma^2 a^2} \\ k_2 &= -i(\omega_s - \frac{\omega_0}{a}) - \frac{\tau}{\sigma^2 a^2} \\ k_3 &= -i\frac{\omega_0 \tau}{a} + \frac{\tau^2}{2\sigma^2 a^2}. \end{aligned}$$

Eq. (2.16) is known as a Gaussian integral and can be computed explicitly:

$$\int_{-\infty}^{\infty} e^{-(k_1 t^2 + k_2 t + k_3)}\, \mathrm{d}t = \sqrt{\frac{\pi}{k_1}} e^{\frac{k_2^2}{4k_1} - k_3}. \tag{2.17}$$

As a result, the Morlet WT at the scale $a_r = \omega_0/\omega_s$ is

$$S_{G,a_r}(\tau) = k_4 A e^{-k_5 \tau^2} e^{i\omega_s \tau}, \tag{2.18}$$

where

$$k_4 = \sqrt{\frac{a_r}{2\pi(2\gamma\sigma^2 a_r^2 + 1)}}$$
$$k_5 = \frac{\gamma}{2\gamma\sigma^2 a_r^2 + 1},$$

which is also a Gaussian function at the frequency ω_s. The width and amplitude of this new Gaussian function are functions of ω_s and of the width of the original Gaussian signal $s_G(t)$. Therefore, similarly to the process of the Lorentzian lineshape, the amplitude (A) and the width of the Gaussian function (inversely proportional to γ) can be obtained as follows:

1. Find $\omega_s = \frac{\partial}{\partial\tau} \arg S_{G,a_r}(\tau)$.
2. Find γ from the second derivative of $\ln|S_{G,a_r}(\tau)|$, which yields

$$\gamma = -\frac{0.5}{\left(\frac{\partial^2}{\partial\tau^2} \ln|S_{G,a_r}(\tau)|\right)^{-1} + \sigma^2 a_r^2}. \tag{2.19}$$

3. Find A from the calculated ω_s and γ.

Remark: Given the Gaussian profile

$$s_G(t) = Ae^{-\gamma t^2} e^{i\omega_s t}, \qquad S_G(\omega) = A\sqrt{\frac{\pi}{\gamma}} e^{-\frac{(\omega-\omega_s)^2}{4\gamma}},$$

its Morlet WT in the frequency domain reads as

$$\begin{aligned}
S_G(\tau, a) &= \frac{1}{2\pi}\sqrt{a} \int S_G(\omega)\, \overline{\Psi(a\omega)}\, e^{i\omega\tau}\, \mathrm{d}\omega \\
&= \frac{A\sqrt{a}}{\sqrt{\pi\gamma}} \int e^{-\frac{(\omega-\omega_s)^2}{4\gamma}} e^{-\frac{\sigma^2(a\omega-\omega_0)^2}{2}} e^{i\omega\tau}\, \mathrm{d}\omega \\
&= \frac{A\sqrt{a}}{\sqrt{\pi\gamma}} \int e^{-\frac{x^2}{4\gamma}} e^{-\frac{\sigma^2(a(\omega_s+x)-\omega_0)^2}{2}} e^{i\omega_s\tau} e^{ix\tau}\, \mathrm{d}x, \\
S_{G,a_r}(\tau) &= \frac{A\sqrt{a_r} e^{i\omega_s\tau}}{\sqrt{\pi\gamma}} \int e^{-\frac{x^2}{4\gamma}} e^{-\frac{\sigma^2(a_r x)^2}{2}} e^{ix\tau}\, \mathrm{d}x \\
&= \frac{A\sqrt{a_r} e^{i\omega_s\tau}}{\sqrt{1+2\gamma\sigma^2 a_r^2}} e^{-\frac{\gamma\tau^2}{1+2\gamma\sigma^2 a_r^2}},
\end{aligned}$$

which coincides with Eq. (2.16).

On the other hand, the Morlet WT at the scale $a_r = \omega_0/\omega_s$ of a Voigt lineshape,

$$s_V(t) = Ae^{-\gamma t^2} e^{-Dt} e^{i\omega_s t}, \tag{2.20}$$

is given by

$$S_{V,a_r}(\tau) = k_6 A e^{-k_5(\tau-k_7)^2} e^{i\omega_s\tau}, \tag{2.21}$$

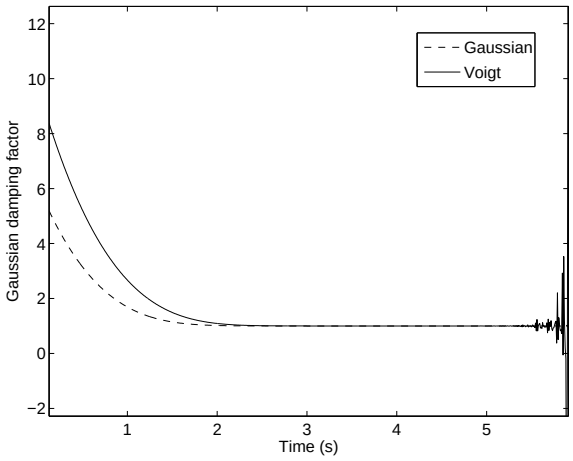

Figure 2.13: The Gaussian damping factor derived from the Morlet WT of Gaussian $s(t) = e^{-t^2}e^{i60t}$ and Voigt $s(t) = e^{-t}e^{-t^2}e^{i60t}$ lineshape.

where

$$k_6 = k_4 e^{\frac{-D^2}{4\gamma}}$$
$$k_7 = \frac{D}{2\gamma}.$$

That is, at the scale a_r, the Morlet WT of the Voigt lineshape is also a Gaussian function with the same width, but shifted in time, with the amplitude smaller than that of the Gaussian lineshape, and its instantaneous frequency is also equal to ω_s.

Note that the scale $a_r = \omega_0/\omega_s$ does not give exactly the maximum modulus of the WT. However, the modulus of the Morlet WT of a signal with a Lorentzian lineshape or a Gaussian lineshape (and also a Voigt lineshape) are maximal at the same scale a_r, provided that $a \in \mathbb{R}$ and $\omega_s \gg D$.

The parameter γ calculated from the second derivative of the modulus of the WT is equal to the MATLAB© solution for both Gaussian and Voigt lineshapes, as shown in Figure 2.13. It shows that the second derivative of the modulus of the Morlet WT can be used to described the second-order broadening of the lineshape, no matter whether it is Gaussian or Voigt. In the case of a Voigt lineshape, γ will give back a Lorentzian whose damping factor is obtained by Eq. (2.12).

Kubo's lineshape

There is also another model to describe the broadening of the lineshape which we would like to include here for the sake of completeness, although it is not well-known in the MRS community. The model is based on the fact that the interaction between homogeneous and inhomogeneous broadening of the lineshape depends on the time scale. For example, if the relaxation time (T_2) is much longer than any effect modulating the energy of a molecule, the lineshape will approach the homogeneous lineshape. On the contrary, if T_2 is short, the lineshape is likely to be Gaussian. Therefore, Kubo (1969) proposed a so-called Gaussian-Markovian modulation, namely

$$s(t) = Ae^{-\frac{\varsigma^2}{\gamma^2}\left(e^{-\gamma t}-1+\gamma t\right)}, \tag{2.22}$$

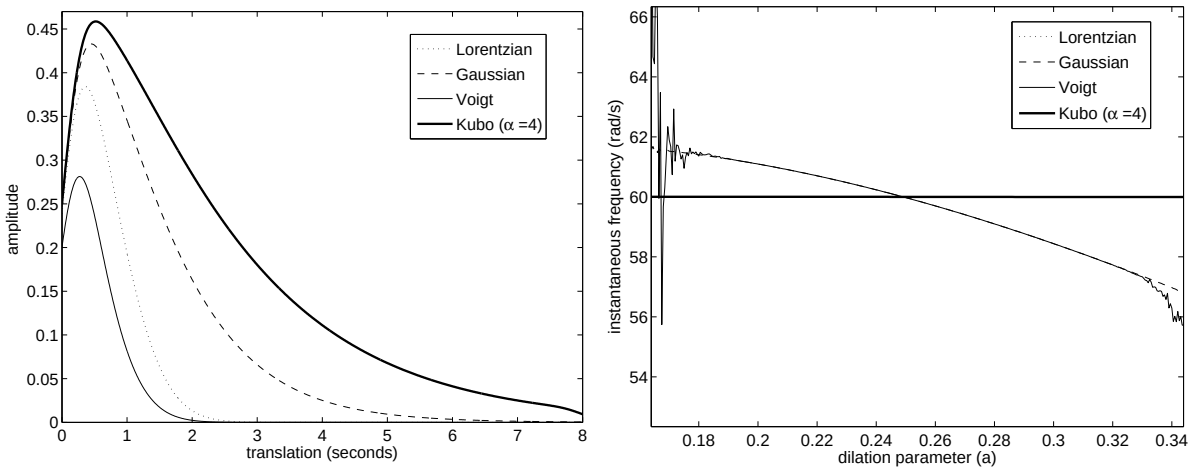

(a) (b)

Figure 2.14: (a) The modulus of the Morlet WT of a signal with different lineshapes, e.g. Lorentzian $s(t) = e^{-t}e^{i60t}$, Gaussian $s(t) = e^{-t^2}e^{i60t}$, Voigt $s(t) = e^{-t}e^{-t^2}e^{i60t}$ and Kubo $s(t) = e^{-0.25(e^{-t}-1+t)}e^{i60t}$ at $a_r = \omega_0/60$; (b) its corresponding instantaneous frequency at t= 4.7 s. Note: $\sigma = 1$, $\omega_0 = 15$ rad/s, $F_s = 800$ s^{-1}, $L = 1024$ points.

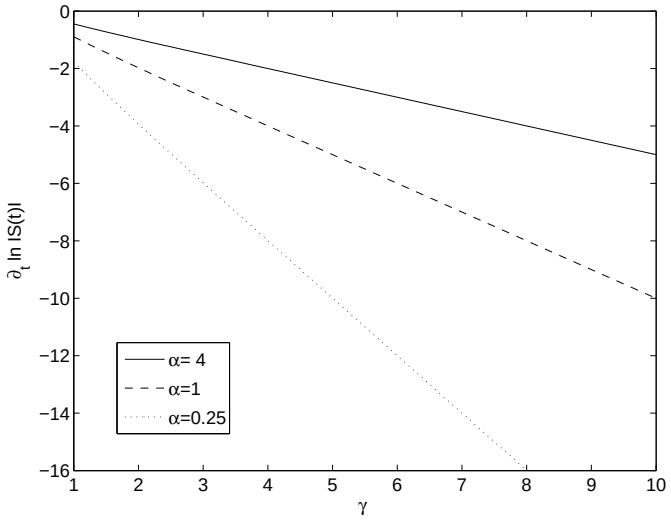

Figure 2.15: $\frac{\partial}{\partial\tau}\ln|S_{G,a_r}(\tau)|$ with respect to Kubo's γ.

to account for this time scale. The parameter γ is inversely proportional to T_2 and ς is the amplitude of the solvent-induced fluctuations in the frequency. If $\alpha = \gamma/\varsigma \ll 1$, the lineshape becomes Gaussian, whereas $\alpha \gg 1$ leads to Lorentzian. The width of the lineshape is $\varsigma^2\gamma$.

Solving Eq. (2.22) seems to be complicated, though may be possible. However, the maximum modulus of the Morlet WT of a Kubo lineshape occurs at the scale $a_r = \omega_0/\omega_s$ similar to those of the Gaussian and Lorentzian lineshapes, but broader, as shown in Figure 2.14 (a). Therefore, the instantaneous frequency Ω_a is still capable of deriving the ω_s, even better than the Gaussian lineshape. The result is presented in Figure 2.14 (b). The damping parameters can also be derived by a linear relation with $\frac{\partial}{\partial\tau}\ln|S_{G,a_r}(\tau)|$, as seen in Figure 2.15, whereas α is related directly to $\frac{\partial^2}{\partial\tau^2}\ln|S_{G,a_r}(\tau)|$.

Arbitrary lineshape

According to Eq. (2.18) and Eq. (2.21), $S_{a_r}(\tau)$ is actually the original profile broadened/ smoothened by a factor related to the σ of the Morlet function. If we iteratively apply the Morlet WT to $S_{a_r}(\tau)$, the original signal will then be broadened by the *same* factor. Therefore, we can extrapolate these broadened Morlet WT in order to resolve the orignal signal without using any prior assumption of the profile. This can be a solution for an arbitrary lineshape. The results in Figure 2.16 indicate that this method works well with the previously discussed lineshapes, including a triangular profile similar to Sima et al. (2009); it can resolve properly the original signal at $t > 0.04$ s when the edge effect vanishes.

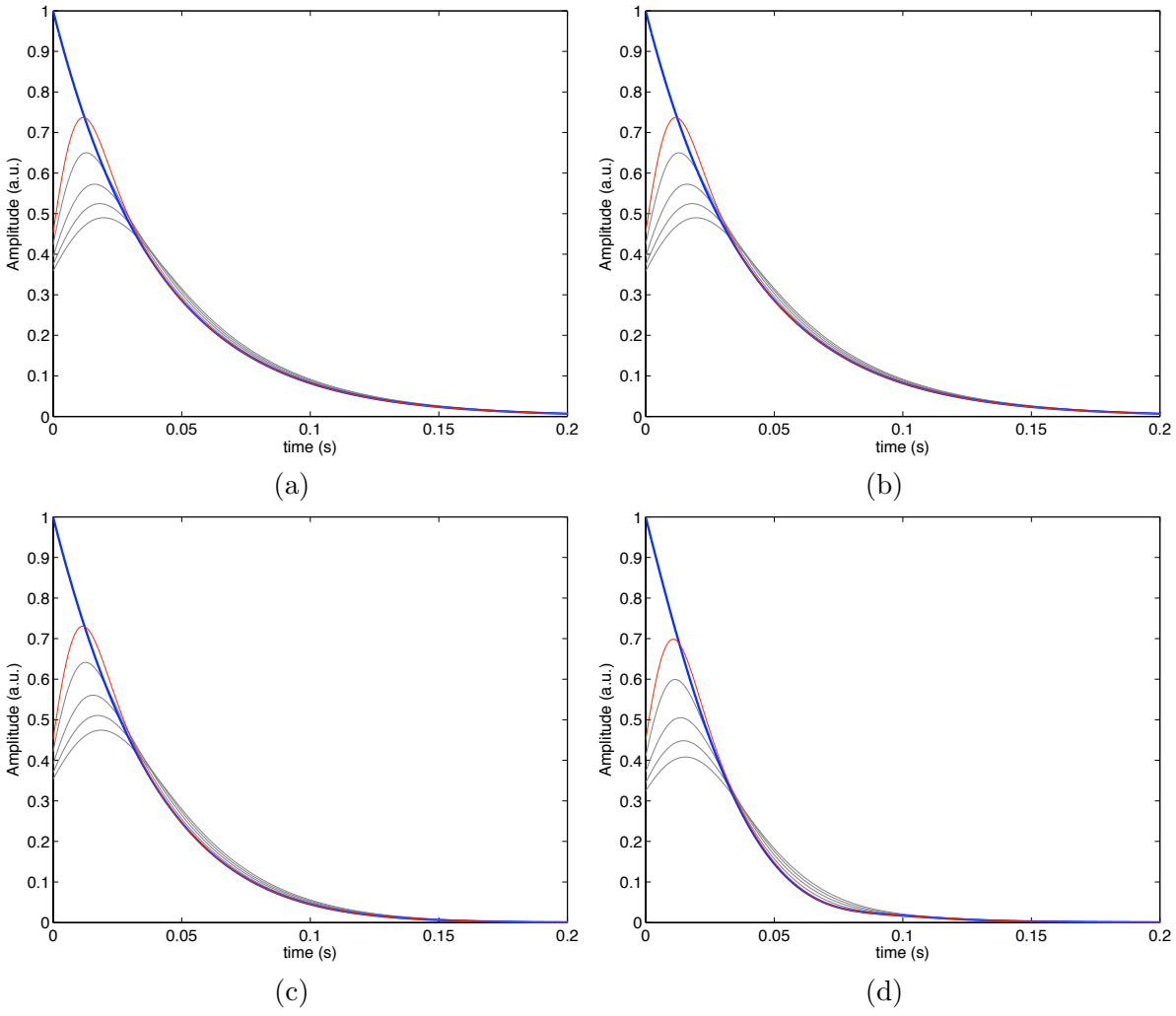

Figure 2.16: The Morlet WT applied iteratively to the Lorentzian (a), Gaussian (b), Voigt (c) and triangular (d) profiles are shown in grey levels. The result when using the extrapolation method (in red) gives a close approximation to the true profiles (in blue) after $t = 0.04$ s. ($\omega_s = 1056$ rad/s, $F_s = 4000$ s^{-1})

2.1.5 Random white noise

If a signal includes noise, Guillemain et al. (1992) suggested averaging in time the derived parameters, e.g. $\Omega_a(\tau)$, i.e.,

$$\overline{\Omega}_a \quad = \quad \frac{1}{T}\int_{\tau_0}^{\tau_0+T} \Omega_a(\tau)\,\mathrm{d}\tau, \tag{2.23}$$

where T is a time period large enough to cancel the noise effect. The randomness of the Gaussian noise appears only at a particular time, therefore averaging in time can reduce the noise effect and gives a more accurate estimation. This can be seen in Figure 2.17. Although the extrapolation method previously described can approximate the lineshape closely to the original signal, the lineshape is distorted by the additive Gaussian noise (SNR=6), resulting in a rough, oscillating damping function. Averaging the derived damping function can ameliorate the distortion; nevertheless the result is still difficult to interprete. One can try increasing T in order to decrease the estimation error, keeping in mind that the higher T leads to the loss of more data (at the beginning of the time axis). Therefore, averaging is not the ultimate solution to this problem and we recommend to denoise by more efficient methods before applying the Morlet WT.

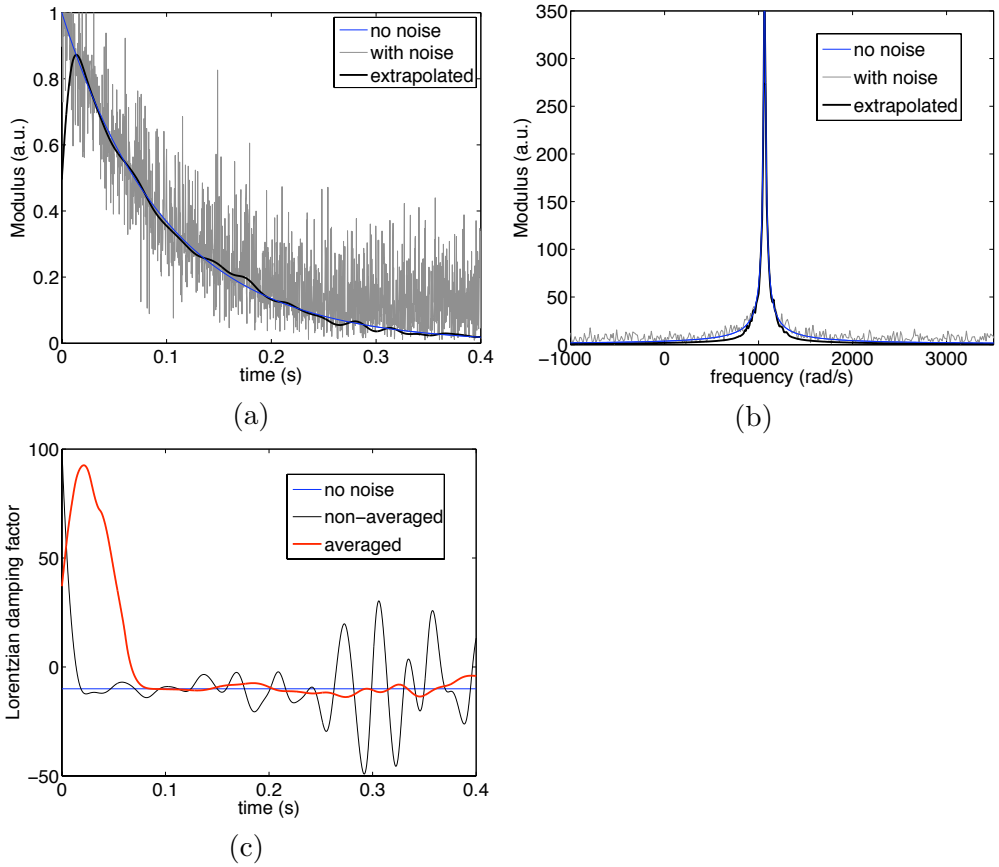

Figure 2.17: An additive Gaussian white noise can distort the derived signal using the extrapolation method to a Lorentzian signal of 1056 rad/s with SNR=6 as seen in both time (a) and frequency (b) domains. The derived Lorentzian damping factor can be smoothened by Eq. (2.23) ($T = L/20 = 0.05$ s) but the result is still ambiguous. ($L = 2048$ data points, $\omega_0 = 10$ rad/s, σ=1, $Fs = 4000$ s^{-1}).

2.2 Limitations of the Morlet wavelet transform

In the previous section, the Morlet WT shows its potential for analysing an MRS signal by means of its amplitude and phase, in addition to its time-frequency representation. However, the method suffers severely from noise and requires a good denoising technique. Another limitation we have already seen is the requirement of a proper ω_0 that should distinguish the signal from solvent, but would not introduce noise in the result. In this section, we will look further on some more limitations that prevent the use of the Morlet WT to quantify MRS signals directly and how to cope with these problems.

2.2.1 Edge effects

Errors in the wavelet analysis can occur at both ends of the spectrum due to the limited time series. The region of the wavelet spectrum in which effects become important[7] increases if the scale a increases, as already seen in Figure 2.1 (a). The size of the affected region is directly related to the frequency ω_0 of the Morlet wavelet function and inversely to the ratio between the frequency of the signal (ω_s) and the sampling frequency (F_s), as illustrated in Figure 2.18.

In practice, the working region is chosen so that the edge effects are negligible within and the characterisation of the MRS signals should be made inside this region, disregarding the presence of the macromolecular contamination.

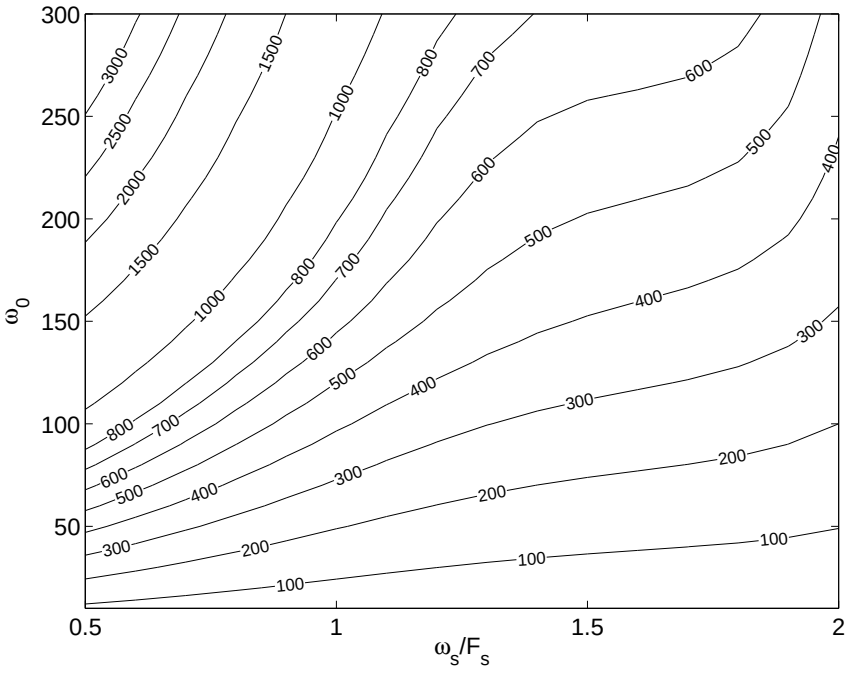

Figure 2.18: Lines showing the width (in number of sample points) of the forbidden regions where the boundary effect becomes important, as a function of ω_0 (rad/s) and the ratio between the signal frequency (ω_s) and the sampling frequency (F_s).

[7] defined as the e-folding time for the autocorrelation of wavelet power at each scale

2.2.2 Interacting/overlapping frequencies

If two frequencies of the signal are too close to each other, the wavelet can interact with both peaks at the same time. Barache et al. (1997) suggested the use of a linear equation system to solve the problem. In the sequel, the simulated N-Acetyl Aspartate (NAA) is used to illustrate how the problem could be solved. The spectrum of the NAA, shown in Figure 2.19 (a), is composed of two different regions – the high, single peak (NAA–acetyl part) and a group of overlapping frequencies (NAA–aspartate part). By using a high ω_0 to separate the overlapping frequencies, the Morlet WT reveals that there are eight frequency peaks in the group as seen in Figure 2.19 (b). The damping factors of the two parts of NAA when using Eq. (2.12) are shown in Figure 2.20 (a). The overlapping peaks cause an oscillation in the derived damping factor, compared to the smooth and stationary damping factor of the single peak. The size and frequency of the oscillation depends on the numbers of neighbours of each peak and the spectral distance to these neighbours. A proper damping factor can be easily achieved by averaging these oscillations in time.

Next, we will try to derive the amplitude of each peak. Let us consider an MRS signal composed of n Lorentzian lines $s(t) = e^{-Dt}\sum_n s_n(t)$, where $s_n(t) = A_n e^{i\omega_n t+\varphi_n}$ and $n = 1, 2, \ldots$ is an indexing number. Its Morlet WT gives local maxima *close* to the scales $a_1 = \omega_0/\omega_1$, $a_2 = \omega_0/\omega_2$, and so on. Therefore, we can establish a systematic relation between S_{a_r} and $s_n(t)$ at each scale as follows:

$$\begin{bmatrix} \frac{S_{a_1}(\tau)}{\sqrt{a_1}} \\ \frac{S_{a_2}(\tau)}{\sqrt{a_2}} \\ \frac{S_{a_3}(\tau)}{\sqrt{a_3}} \\ \vdots \end{bmatrix} = e^{-D\tau} \begin{bmatrix} C_1 & C_{12} & C_{13} & \cdots \\ C_{21} & C_2 & & \\ C_{31} & & \ddots & \\ \vdots & & & \end{bmatrix} \begin{bmatrix} s_1(\tau) \\ s_2(\tau) \\ s_3(\tau) \\ \vdots \end{bmatrix},$$

where

$$C_n = \exp\left(\frac{\sigma^2 a_n^2 D^2}{2}\right)$$

$$C_{mn} = \exp\left[-\frac{\sigma^2\omega_0^2}{2}\left(\frac{\omega_n - \omega_m - iD}{\omega_m}\right)^2\right].$$

The parameter C_{mn} decreases when $|\omega_m - \omega_n|$ is large. We can also see that the Morlet WT is more tolerant to overlapping frequencies when ω_m is high. If C_{mn} is not negligible, solving the linear equations could give the information for each $s_n(t)$. The linear equations can well separate and derive the amplitudes of NAA-aspartate part as seen in Figure 2.20 (b). There exists, however, a small bias from the estimation, depending on the numbers and distribution of overlapping frequencies, e.g. distance between each frequency and ω_0. For the NAA, the bias is approximately 1% of its amplitude (in time domain), when $\omega_0 = 200$ rad/s is used. *In practice*, the actual damping function is required to set up the linear equations. Ideally, one can find the arbitrary damping function by the method proposed by Rabeson et al. (2008) and take into account the non-Lorentzian damping function for solving the problem.

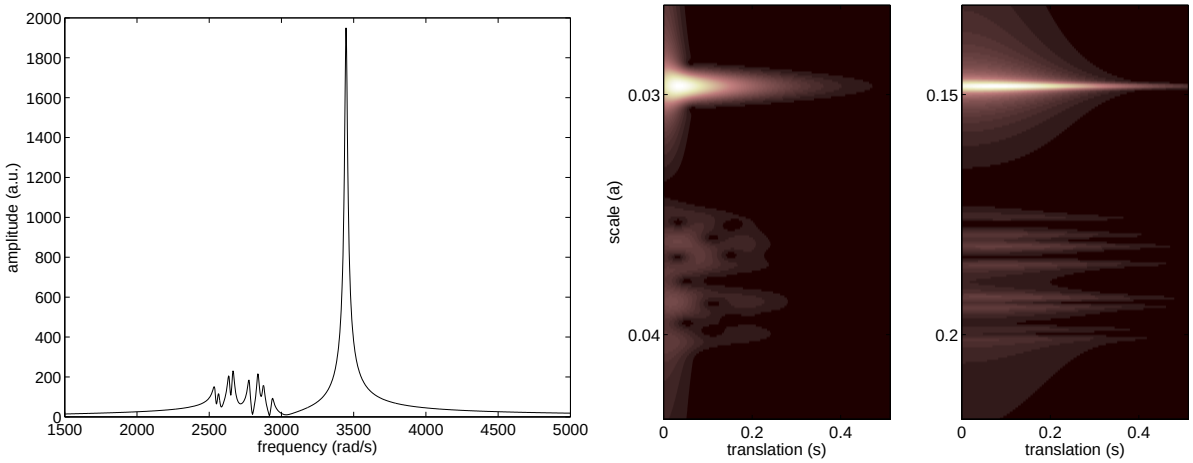

(a) (b)

Figure 2.19: (a) Frequency response of NAA, composed of the high, single peak (NAA–acetyl part) and a group of overlapping frequencies (NAA–aspartate part); (b) The Morlet wavelet transfrom of NAA when $\omega_0 = 100$ rad/s (left) and $\omega_0 = 500$ rad/s (right).

2.3 Working in a real life environment

By real life environment, we mean genuine acquired data, either *in vitro* or *in vivo*, rather than simulated ones. In that case, the ideal Lorentzian or Gaussian lineshape of individual peaks gets distorted. To give an example, we show in Figure 2.21 the analysis of an *in vitro* Creatine signal. We see that intermittent noise appears, in the form of many disrupted, horizontal bands in the WT. Thus the noise occurs for a while at some particular frequencies and then disappears.[8] Such characteristics differ from the Gaussian white noise that usually appears as vertical bands in the WT. It is also possible that the Gaussian white noise at that duration has the same intensity. The analysis of this *in vitro* Creatine signal shows that the frequency distribution at each peak is broad and the *almost* stationary Gaussian damping factor indicates that the acquired signal has a lineshape close to that of the Gaussian function. Nevertheless, deriving the amplitude using the Gaussian assumption may lead to an inaccurate estimation.

When the acquisition is made in an *in vivo* environment, the exponential decay of an MRS signal is severely distorted. This is due to the inhomogeneity of the applied static magnetic field in the tissues and to eddy currents induced in the magnet walls by switching magnetic gradient-fields on and off. Apart from the problem of overlapping frequencies in each metabolite, an *in vivo* MRS signal is composed of several metabolites. Therefore, the challenge is to find a good combination of the derived amplitude that the Morlet WT derives at each frequency. This is yet to be solved.

[8] We don't know the origin of that noise, which in fact represents the part of the signal that we cannot identify in terms of specific, known contributions.

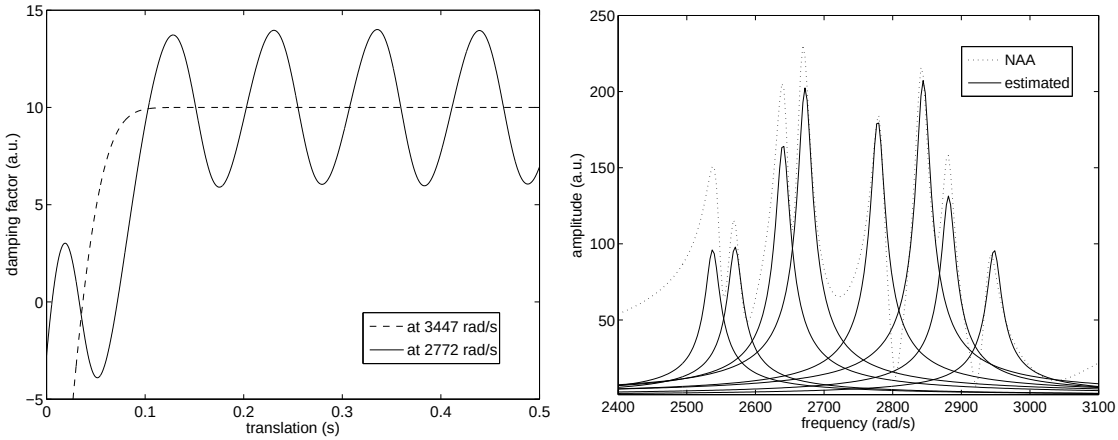

(a) (b)

Figure 2.20: (a) Damping function of NAA, derived by Eq. (2.12); (b) Amplitudes of NAA – aspartate part, derived by the linear equations (with zero phase).

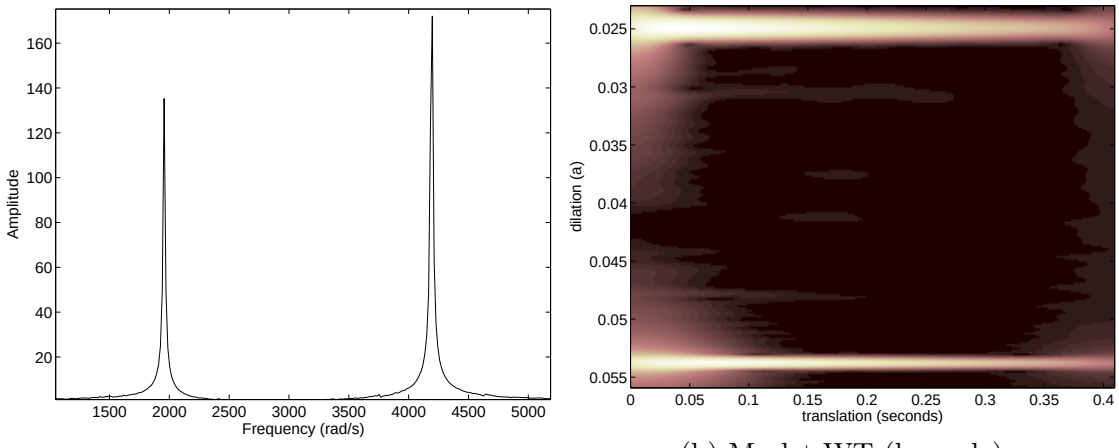

(a) Frequency response (b) Morlet WT (logscale)

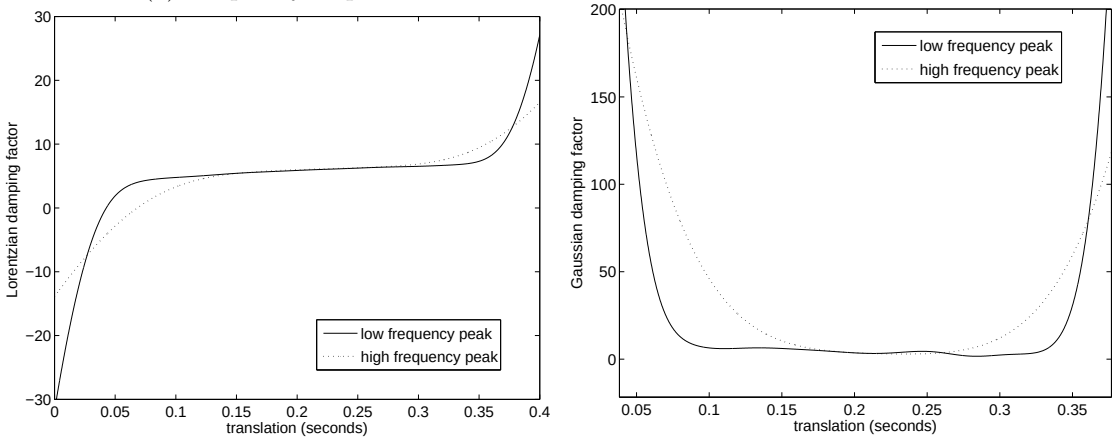

(g) derived Lorentzian damping factor (h) derived Gaussian damping factor

Figure 2.21: Characteristics of *in vitro* Creatine at 9.4 T (acquired by EPFL, Lausanne) which is composed of two frequencies (ω_h and ω_l) is analysed by the Morlet WT. The almost constant Gaussian damping factor indicates that the lineshape of the *in vitro* signal is likely to be Gaussian.

Chapter 3

Wavelet analysis in MRS: Autocorrelation wavelets

3.1 Introduction

In the previous chapter, we have used exclusively the Morlet wavelet in the analysis of MRS signals. One of the issues we pointed out is the analysis of signals with two or more frequency peaks too close to each other. Also, the presence of noise in the signal can be a problem in the estimation of the signal parameters, in particular if the signal contains doublets or multiplets. Because of this separation problem (or metabolite identification), it was suggested in (Suvichakorn et al., 2009) to use *a priori*knowledge to construct wavelet functions more adapted to the signals to be analysed. In particular, it was mentioned that a "two-humped" or even a "multi-humped" wavelet could be better to analyse MRS signals containing doublets or multiplets, respectively (Grossmann et al., 1990).

Thus, in order to construct a wavelet whose spectrum is more similar to the metabolite spectrum to be investigated, large enough to have a good frequency resolution and sufficient robustness to noise, we propose to use an autocorrelation function estimator. The procedure then consists in choosing a known signal, for example a model FID or an *in vitro* MRS signal, estimating its autocorrelation function and using it as a wavelet function in a CWT analysis, instead of the Morlet or another standard wavelet. With this procedure, we can try to identify the presence of that particular component in a more complex signal and separate it from the rest of the signal components, in order to better estimate its parameters.

In the next section we present some theoretical aspects related to this kind of wavelet construction, using MRS signal models. Then, we present some preliminary results showing the capability of this technique, the effects of windowing and discretization of the signal and wavelet and performance of this technique in presence of noise.

It should be noted that autocorrelation wavelets have been considered before, albeit in a totally different context (Shensa, 1992; Saito and Beylkin, 1993; Beylkin and Torrésani, 1996). Namely, these authors evaluate the autocorrelation function of a standard (Daubechies) wavelet, or the corresponding scaling function, and use it for interpolation purposes, all in the framework of a multiresolution analysis based DWT. Clearly, this approach is completely foreign to the present one.

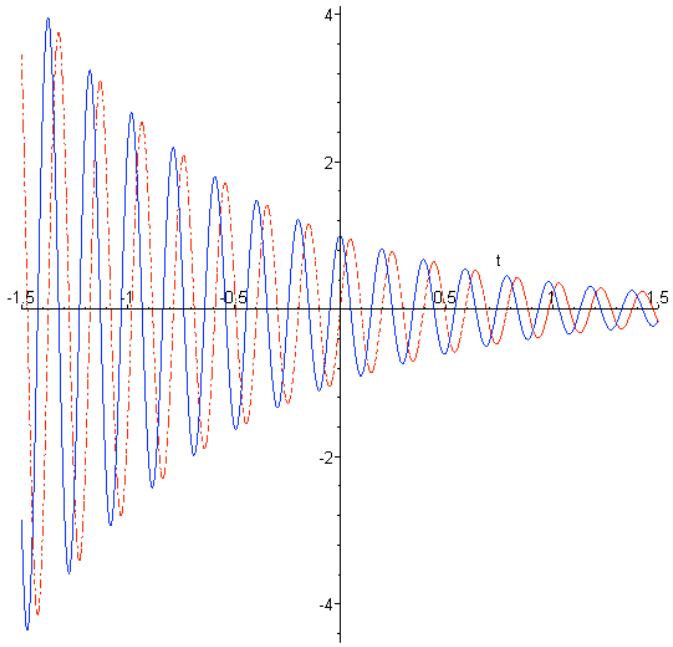

Figure 3.1: Real part (solid line) and imaginary part (dashed line) of $s(t)$ for $A_1 = 1$, $D_1 = 1$, $\omega_1 = 32$ rad/s, $\varphi_1 = 0$ and $t \in [-2, 2]$.

3.2 MRS autocorrelation wavelet: Theoretical analysis

We want to construct a wavelet function from the autocorrelation of a known MRS signal and see its capabilities as an analysis instrument. To that effect, we start by choosing a simple MRS signal model and we will build its associated wavelet function using autocorrelation estimators. Then we find the analytical expression for a CWT analysis of this signal by its associated wavelet function. Finally, we extend the expressions to a more complex signal model.

3.2.1 One frequency component signal

So, using the same approach as in the previous chapter, let us start by using as a MRS signal $s(t)$ a Lorentzian lineshape with a single frequency component, rewritten here for convenience, as:

$$s(t) = A_1 e^{-D_1 t} e^{i(\omega_1 t + \varphi_1)},\ A_1 > 0,\ D_1 > 0. \tag{3.1}$$

The graph of this signal is shown in Figure 3.1, for $A_1 = 1$, $D_1 = 1$ s, $\omega_1 = 32$ rad/s, $\varphi_1 = 0$ and $t \in [-2, 2]$.

As shown in the previous chapter, the Fourier transform of $s(t)$ is given by

$$S(\omega) = 2\pi A_1 e^{i\varphi_1} \delta(\omega - (\omega_1 + iD_1)), \tag{3.2}$$

where δ is the Dirac delta function.

The next step is to create the autocorrelation function of this signal. Given an ergodic process time series $x(t)$, its autocorrelation function estimator $R_{xx}(t)$ of is defined by

$$R_{xx}(t) = \int_{-\infty}^{\infty} x(\tau)\overline{x(\tau - t)}\,\mathrm{d}\tau \tag{3.3}$$

$$= \int_{-\infty}^{\infty} \overline{x(\tau)}x(\tau + t)\,\mathrm{d}\tau, \tag{3.4}$$

where $\overline{x(t)}$ denotes the complex conjugate of $x(t)$ (Papoulis and Pillai, 2002).

It is important to remark that the autocorrelation function should obey the following properties, among others:

- $R_{xx}(0) \in \mathbb{R}$;
- $R_{xx}(0) \geqslant |R_{xx}(\tau)|$;
- $R_{xx}(-t) = \overline{R_{xx}(t)}$, where $\overline{R_{xx}}$ denotes the complex conjugate of R_{xx}.

The autocorrelation estimator in the frequency domain $S_{xx}(\omega)$, sometimes called Autospectrum estimator, is defined as the Fourier transform of R_{xx} and can be evaluated by the Wiener-Khintchine relation (Bendat and Piersol, 2000; Papoulis and Pillai, 2002):

$$S_{xx}(\omega) = \mathcal{F}\left\{R_{xx}(t)\right\} = |X(\omega)|^2, \tag{3.5}$$

where $X(\omega)$ is the Fourier transform of $x(t)$.

However, applying directly (3.2) in (3.5) is clearly impossible, since $S(\omega)$ is a δ function. Instead, we use a slightly different, in fact more realistic, model for our *in vitro* signal. Indeed, every FID (Free Induction Decay) has a beginning, so that we better model the MRS FID signals as follows (since the phase φ_1 drops out in the autocorrelation function, we omit it):

$$s_1(t) = A_1 e^{-D_1 t} e^{i\omega_1 t}\,\theta(t),\ D_1 > 0, \tag{3.6}$$

where $\theta(t)$ is the Heaviside function (or step function), defined by

$$\theta(t) = \begin{cases} 0, & t < 0 \\ 1, & t \geqslant 0 \end{cases} \tag{3.7}$$

Now, the Fourier transform of (3.6) is given by:

$$S_1(\omega) = \int_0^{\infty} A_1 e^{-D_1 t} e^{i\omega_1 t} e^{-i\omega t}\,\mathrm{d}t$$

$$= \frac{A_1}{D_1 + i(\omega - \omega_1)}. \tag{3.8}$$

The autocorrelation function of the expression (3.8) can be obtained easily by substituting (3.8) in (3.5) by:

$$S_{s_1 s_1}(\omega) = \left|\frac{A_1}{D_1 + i(\omega - \omega_1)}\right|^2$$

$$= \frac{A_1^2}{D_1^2 + (\omega - \omega_1)^2} \tag{3.9}$$

To find the autocorrelation function in the time domain, one can use the inverse asymmetric Fourier transform of (3.9) or apply (3.6) into the definitions given by (3.3) and (3.4). In both cases the result is

$$R_{s_1 s_1}(t) = \frac{A_1^2}{2D_1} e^{-D_1|t|+i\omega_1 t},\ -\infty\ < t < \infty\,. \tag{3.10}$$

Taking $s_1(t)$ as our MRS *in vitro* signal, both (3.10) and (3.9) give us a good description of a function that can be used as a wavelet, in time or frequency domain, respectively, because it is an oscillatory, complex and localized function. Also, this function is strongly related to the signal of interest and is large enough to give us a good frequency resolution and insensitivity to noise. But this technique does not ensure yet that this function obeys the (weak) admissibility condition $S_{s_1 s_1}(0) = 0$ (Antoine et al., 2004; Daubechies, 1992).

In order to enforce this, we must apply an additive correction term to the expression (3.9). Using the same idea as for the Morlet wavelet correction term, it can be easily verified that the correction term in the frequency domain $H(\omega)$ may be taken as

$$H(\omega) = \frac{A_1^2}{D_1^2 + (\omega^2 + \omega_1^2)}\,. \tag{3.11}$$

Using this term, then the autocorrelation wavelet function $\Psi_{\text{adm}}(\omega)$ can be defined as:

$$\Psi_{\text{adm}}(\omega) = \frac{A_1^2}{D_1^2 + (\omega - \omega_1)^2} - \frac{A_1^2}{D_1^2 + (\omega^2 + \omega_1^2)}\,. \tag{3.12}$$

Although in this case the correction term is easy to find, in practice realistic values of D_1 and ω_1 make it numerically negligible, so that the correcting term can indeed be omitted, exactly as in the Morlet case. Thus, we can define the wavelet function by

$$\Psi(\omega) = \frac{A_1^2}{D_1^2 + (\omega - \omega_1)^2}\,. \tag{3.13}$$

In the time domain, this simplified wavelet is then defined by

$$\psi(t) = \frac{A_1^2}{2D_1} e^{-D_1|t|+i\omega_1 t},\ -\infty < t < \infty\,. \tag{3.14}$$

We show in Figure 3.2a the graph of Ψ_{adm} and Ψ for $A_1 = 1$, $D_1 = 1$ and $\omega_1 = 32$ rad/s. It can be seen that there is almost no difference between the two graphs and the value for the two functions for $\omega = 0$ is 0.0 and 0.0009756, respectively.

For arbitrary ω, the value of the correction term is of the order of 10^{-4} and it is indeed negligible. It is also interesting to remark that the expressions so obtained are real in the frequency domain and can be easily implemented in numerical software.

We show in Figure 3.2b the real part (solid line) and the imaginary part (dashed line) of $\psi(t)$, respectively, for $A_1 = 1$, $D_1 = 1$ and $\omega_1 = 32$ rad/s.

Once the wavelet function is defined, we can perform the CWT analysis of a MRS signal $s(t)$ using the time or the frequency domain definitions for the CWT given in (A.2) and (A.3), respectively. So, let us perform the CWT of the signal (3.1) using as a mother wavelet the function described in (3.13), in the frequency domain. From now on, this mother wavelet will be called the wavelet function associated to the signal (3.1), since it has the same frequency and damping

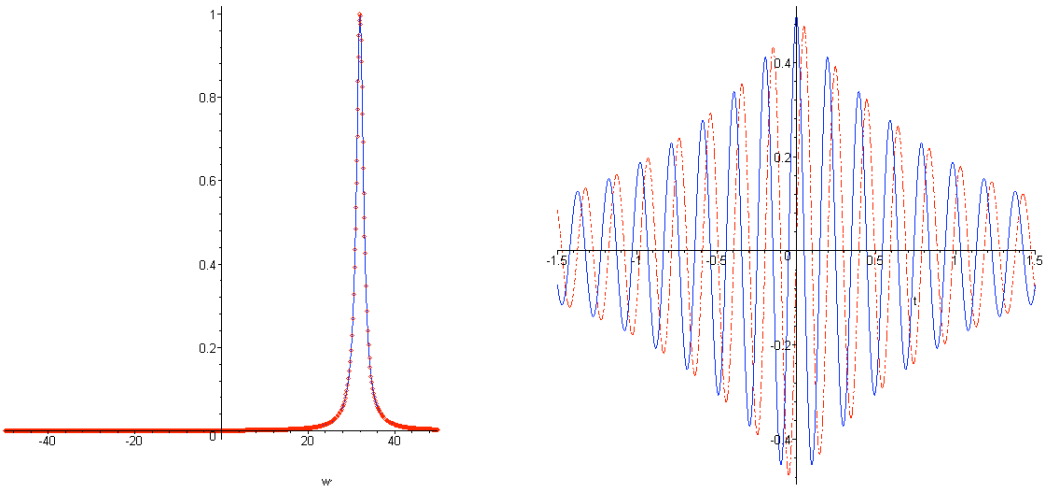

(a) (b)

Figure 3.2: (a)$\Psi_{\text{adm}}(\omega)$ (solid line) and $\Psi(\omega)$ (dotted line) for $A_1 = 1$, $D_1 = 1$ and $\omega_1 = 32$ rad/s; (b) $\psi(t)$, for $A_1 = 1$, $D_1 = 1$ and $\omega_1 = 32$ rad/s: real part (solid line) and imaginary part (dashed line).

factor as the signal to be analysed. Substituting (3.2) and (3.13) in the definition (2.1) or (A.3) of the CWT, we obtain:

$$\begin{aligned} S(\tau, a) &= \frac{1}{2\pi}\sqrt{a}\int_{-\infty}^{\infty} 2\pi A_1 e^{i\varphi_1}\delta(\omega - (\omega_1 + iD_1))\frac{A_1^2}{D_1^2 + (a\omega - \omega_1)^2}e^{i\omega\tau}\,\mathrm{d}\omega \\ &= \sqrt{a}A_1 e^{i\varphi_1}e^{(-D_1+i\omega_1)\tau}\frac{A_1^2}{D_1^2 + [a(\omega_1 + iD_1) - \omega_1]^2} \\ &= \sqrt{a}\; s(\tau)\frac{A_1^2}{D_1^2 + [\omega_1(a-1) + iaD_1]^2}\,. \end{aligned} \tag{3.15}$$

The absolute value of (3.15) is given by

$$\begin{aligned} |S(\tau, a)| &= \sqrt{a}\,|s(\tau)|\left|\frac{A_1^2}{D_1^2 + [\omega_1(a-1) + iaD_1]^2}\right| \\ &= \frac{\sqrt{a}\,e^{-D_1\tau}\,A_1^3}{\left[(a-1)^2(D_1^2 + \omega_1^2)[D_1^2(a+1)^2 + \omega_1^2(a-1)^2]\right]^{1/2}}\,. \end{aligned} \tag{3.16}$$

The graph of (3.16) is shown in Figure 3.3a for $A_1 = 1$, $D_1 = 1$, $\omega_1 = 32$ rad/s, $b \in [0, 2]$ and $a \in [0.5, 1.5]$, $a \neq 1$.

The phase of (3.15) is given by

$$\arg S(\tau, a) = \arctan\left(\frac{\sin\omega_1\tau\,[D_1^2(a+1) + \omega_1^2(1-a)] + 2aD_1\omega_1\cos\omega_1\tau}{\cos\omega_1\tau\,[D_1^2(a+1) + \omega_1^2(1-a)] - 2aD_1\omega_1\sin\omega_1\tau}\right)\,. \tag{3.17}$$

The graph of (3.17) was obtained numerically and the result is shown in Figure 3.3b, for $A_1 = 1$, $D_1 = 1$ and $\omega_s = 32$ rad/s, $\tau \in [0, 2]$ and $a \in [0.5, 1.5]$.

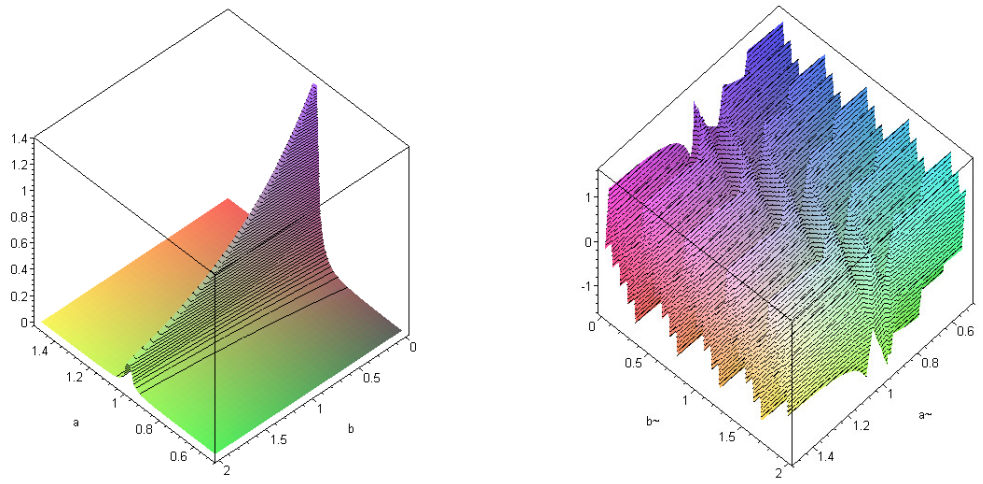

(a) (b)

Figure 3.3: (a) $|S(\tau, a)|$ and (b) $\arg S(\tau, a)$ for $A_1 = 1$, $D_1 = 1$, $\omega_s = 32$ rad/s, $\tau \in [0, 2]$ and $a \in [0.5, 1.5], a \neq 1$.

Now we see that the expressions (3.15) and (3.16) diverge for $a = 1$, and also that $|S(\tau, a)|$ increases steadily as $a \to 1$. This means that, when one analyses a Lorentzian MRS signal with its associated wavelet function, the maximum of the absolute value of the CWT transform should occur at $a = 1$, for all values of τ. The presence of this local maximum indicates that the component $s(t)$ is present on the signal. Also, if the signal $s(t)$ is shifted in frequency, e.g. $\omega_{1a} = \omega_1 + \Delta\omega_1$, but it is still analysed by the original wavelet function, exactly as in the Morlet wavelet case, the local maximum now will occur at $a = \omega_1/\omega_{1a}$. The infinite value of (3.15) and (3.16) at $a = 1$ is a consequence of the "perfect match" between the signal and its associated wavelet function, both with infinite duration. But, if we choose different damping factors for the signal and for the wavelet, namely D_1 for the wavelet function and D_{11} for the signal, then (3.15) will become:

$$S(\tau, a) = \sqrt{a}\, s(\tau) \frac{A_1^2}{D_1^2 + [\omega_1(a-1) + iaD_{11}]^2}\,. \tag{3.18}$$

Considering that $D_1 \neq D_{11}$, for $a = 1$, the expression (3.18) becomes

$$S(\tau, 1) = s(\tau) \frac{A_1^2}{D_1^2 - D_{11}^2}\,. \tag{3.19}$$

The absolute value of (3.19) will be

$$\begin{aligned} |S(\tau, 1)| &= |s(\tau)|\, \frac{A_1^2}{|D_1^2 - D_{11}^2|} \\ &= e^{-D_{11}\tau}\, \frac{A_1^3}{|D_1^2 - D_{11}^2|}\,. \end{aligned} \tag{3.20}$$

Taking the natural logarithm of both sides of (3.20), we get

$$\ln |S(\tau, 1)| = \ln e^{-D_{11}\tau} + \ln |A_1^3| - \ln |D_1^2 - D_{11}^2|\,. \tag{3.21}$$

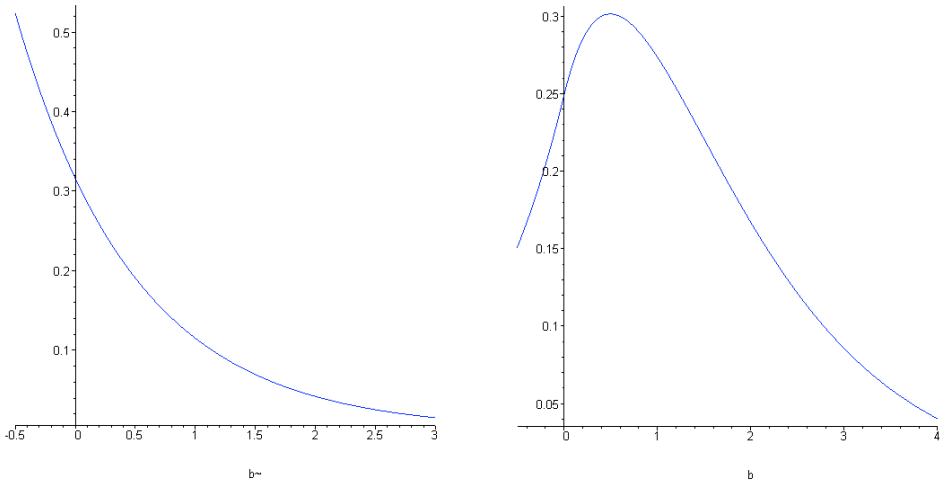

(a) (b)

Figure 3.4: (a) $|S(\tau, 1)|$ from (3.20) for $a = 1$ and; (b) $|S_1(\tau, 1)|$ of the signal (3.6) for $A_1 = 1$, $D_1 = 1$, $D_{11} = 1.01$ and $\omega_s = 32$ rad/s

Finally, if we derive (3.21) with respect to τ, we have

$$\frac{d}{d\tau} \ln |S(b, 1)| = -D_{11} \,. \tag{3.22}$$

With (3.22) one can estimate the damping factor for the signal by

$$D_{11} = -\frac{d}{d\tau} \ln |S(\tau, 1)| \,. \tag{3.23}$$

The behavior of the CWT at scale $a = 1$ should change slightly if we analyse a signal limited in time, such as $s_1(t)$ for instance. To test this effect, first we evaluate the expression (3.20) numerically for $A_1 = 1$, $\omega_1 = 32$ rad/s, $D_1 = 1$ and $D_{11} = 1.01$. The result can be seen in Figure 3.4a. Next we calculate an expression for the CWT of the signal (3.6), but with a damping factor D_{11} different from the one (D_1) used for the wavelet function, called here $S_1(\tau, 1)$. Then we evaluate its absolute value numerically for the same parameter values as in the former case, for $a = 1$. The result can be seen in Figure 3.4b.

Looking at these graphs, its interesting to notice that, in the $s_1(t)$ case, the maximum of the function does no longer appear at $\tau = 0$, the beginning of the signal, but it is slightly translated. Also, it does not have a sharp peak, but a rounded one instead. Still, one can use the expression (3.23) applied to $|S(\tau, 1)|$ of the signal (3.6) to estimate the damping factor, because, after the rounded peak, the function decays exactly as the former one.

3.2.2 Two-component signal

We will now extend the concept to more complex signals. Instead of only one component, let us assume that our signal is a sum of two Lorentzian components (we leave out the phases again):

$$\begin{aligned} s_2(t) &= A_1\, e^{-D_1 t} e^{i\omega_1 t} + A_2\, e^{-D_2 t} e^{i\omega_2 t},\ D_1, D_2 > 0, \\ &\equiv s^{(1)}(t) + s^{(2)}(t)\,, \end{aligned} \tag{3.24}$$

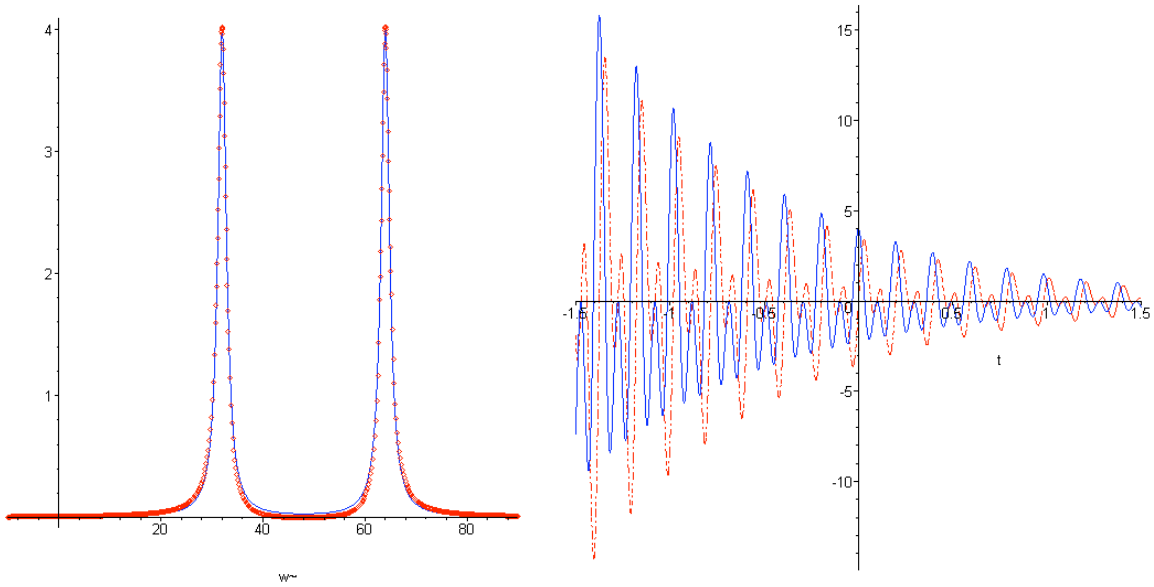

(a) (b)

Figure 3.5: (a) $\Psi_2(\omega)$ (dotted line) and $\widetilde{\Psi_2}(\omega)$ (solid line) and (b) Real part (solid line) and imaginary part (dashed line) of $s_2(t)$ for $A_1 = A_2 = 2$, $D_1 = D_2 = 1$, $\omega_1 = 32$ rad/s and $\omega_2 = 64$ rad/s.

where $s^{(k)}(t)$, $k = 1, 2$, denotes a single Lorentzian of the form (3.1), with parameters A_k, D_k, ω_k and $\varphi_k = 0$. The Fourier transform of this signal is:

$$S_2(\omega) = 2\pi \left[A_1\, \delta(\omega - (\omega_1 + iD_1)) + A_2\, \delta(\omega - (\omega_2 + iD_2))\right] . \tag{3.25}$$

Following the same procedure as before, we define the left truncated version of this signal:

$$s_2'(t) = \left[A_1\, e^{-D_1 t} e^{i\omega_1 t} + A_2\, e^{-D_2 t} e^{i\omega_2 t}\right] \theta(t),\ D_1, D_2 > 0\,. \tag{3.26}$$

where $\theta(t)$ is again the Heaviside function.

Then, it is easy to see that the Fourier transform of (3.26) is given by

$$S_2'(\omega) = \frac{A_1}{[D_1 + i(\omega - \omega_1)]} + \frac{A_2}{[D_2 + i(\omega - \omega_2)]}\,. \tag{3.27}$$

The autocorrelation of this function in the frequency domain, $S_{s_2's_2'}(\omega)$, is defined by:

$$\begin{aligned} S_{s_2's_2'}(\omega) &= \left| \frac{A_1}{[D_1 + i(\omega - \omega_1)]} + \frac{A_2}{[D_2 + i(\omega - \omega_2)]} \right|^2 \\ &= \frac{A_1^2}{[D_1^2 + (\omega - \omega_1)^2]} + \frac{A_2^2}{[D_2^2 + (\omega - \omega_2)^2]} + \frac{2A_1A_2[D_1D_2 + (\omega - \omega_1)(\omega - \omega_2)]}{[D_1^2 + (\omega - \omega_1)^2][D_2^2 + (\omega - \omega_2)^2]}\,. \end{aligned} \tag{3.28}$$

Again, if we choose properly the values of ω_n and D_n, the value of (3.28) can be considered numerically negligible at $\omega = 0$ and we can use this function as a wavelet function. In other words,

$$\Psi_2(\omega) = \frac{A_1^2}{[D_1^2 + (\omega - \omega_1)^2]} + \frac{A_2^2}{[D_2^2 + (\omega - \omega_2)^2]} + \frac{2A_1A_2[D_1D_2 + (\omega - \omega_1)(\omega - \omega_2)]}{[D_1^2 + (\omega - \omega_1)^2][D_2^2 + (\omega - \omega_2)^2]} \tag{3.29}$$

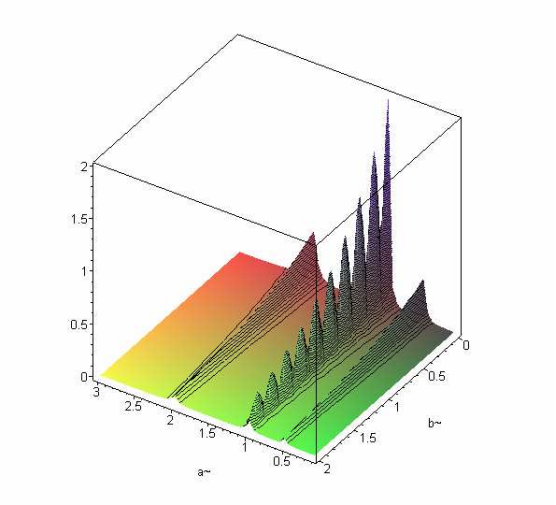

Figure 3.6: $|S_2(\tau, a)|$ for $A_1 = A_2 = 1$, $D_1 = D_2 = 1$, $\omega_1 = 32$ rad/s and $\omega_2 = 64$ rad/s, $b \in [0, 2]$ and $a \in [0.1, 3], a \neq 1.0$

In addition, the first two terms of (3.29) are the sum of absolute squared values of the two independent components. But if the peaks are sharp and far enough from each other, the third term (3.29) will cause only a slight change in the shape of the two-peak function without affecting the amplitude of the peaks. Thus we can safely drop it and define an approximate version of the wavelet function as

$$\widetilde{\Psi_2}(\omega) = \frac{A_1^2}{[D_1^2 + (\omega - \omega_1)^2]} + \frac{A_2^2}{[D_2^2 + (\omega - \omega_2)^2]}\,. \tag{3.30}$$

Figure 3.5a shows both the wavelet function from (3.29) (dotted line) and its approximate version from (3.30) (solid line) with frequencies $\omega_1 = 32$ and $\omega_2 = 64$ rad/s, phase $= 0$ for both components, amplitudes $A_1 = A_2 = 2$ and damping factors $D_1 = D_2 = 1$. In Figure 3.5b we present the two-peak signal $s_2(t)$, for the same parameter values. As can be seen, the removal of the third component does not affect dramatically the qualitative aspect of the analysis, since the peaks are not affected, but only the shape of the base function.

Now, proceeding as before, we can evaluate the CWT of the signal (3.24) using (3.30) as wavelet function, in frequency domain, and obtain

$$\begin{aligned} S_2(\tau, a) = \sqrt{a} \Bigg\{ & \frac{A_1^2\, s^{(1)}(\tau)}{D_1^2 + [a(\omega_1 + iD_1) - \omega_1]^2} + \frac{A_2^2\, s^{(2)}(\tau)}{D_2^2 + [a(\omega_2 + iD_2) - \omega_2]^2} + \\ & + \frac{A_1^2\, s^{(2)}(\tau)}{D_1^2 + [a(\omega_2 + iD_2) - \omega_1]^2} + \frac{A_2^2\, s^{(1)}(\tau)}{D_2^2 + [a(\omega_1 + iD_1) - \omega_2]^2} \Bigg\}\,. \end{aligned} \tag{3.31}$$

The first two terms in (3.31) diverge again for $a = 1$ and they will interact with each other. Also, the last two terms are cross-terms and they will give local maxima at $a = \omega_1/\omega_2$ and $a = \omega_2/\omega_1$. We can see this behavior in Figure 3.6, where $|S_2(\tau, a)|$ is numerically evaluated for $A_1 = A_2 = 1$, $D_1 = D_2 = 1$, $\omega_1 = 32$ and $\omega_2 = 64$ rad/s.

For this example of a two-peak signal, assume as before that the wavelet function has damping factors D_1 and D_2, but the signal has different ones, namely D_{11} and D_{22}. Then, if $D_1 \neq D_{11}, D_{22}$

and $D_2 \neq D_{11}, D_{22}$, then (3.31)will converge for $a = 1$ and yields (for $a = 1$):

$$S_2(\tau, 1) = \frac{A_1^2\, s^{(1)}(\tau)}{D_1^2 - D_{11}^2} + \frac{A_2^2\, s^{(2)}(\tau)}{D_2^2 - D_{22}^2} + \frac{A_1^2\, s^{(2)}(\tau)}{D_1^2 + [(\omega_2 + iD_{22}) - \omega_1]^2} + \frac{A_2^2\, s^{(1)}(\tau)}{D_2^2 + [(\omega_1 + iD_{11}) - \omega_2]^2}\,. \tag{3.32}$$

In this expression, the first two terms do not diverge, but they cannot be used to estimate the damping factors by taking the logarithm of $|S_2(\tau, 1)|$, as in the one peak example, because we have the logarithm of a sum of two components. The interaction between the two components causes oscillations around $a = 1$ as we can see in Figure 3.6. On the other hand, if we choose one of the two other local maxima of the CWT, for instance, $a = \omega_2/\omega_1$, and again considering that the other factors are small enough at this scale, then only the last term of (3.31) will be significative and we can estimate the damping factor as:

$$\begin{aligned} \frac{d}{d\tau} \ln |S(\tau, \frac{\omega_2}{\omega_1})| &\approx \frac{d}{d\tau} \ln |e^{-D_{11}\tau}| + \frac{d}{d\tau} \ln |A_1 A_2^2| - \frac{d}{d\tau} \ln |D_2^2 + [(\omega_1 + iD_{11}) - \omega_2]^2| = \\ &= -D_{11}\,. \end{aligned} \tag{3.33}$$

The same can be done for $a = \omega_1/\omega_2$ and in this case, we can estimate

$$\begin{aligned} \frac{d}{d\tau} \ln |S(\tau, \frac{\omega_1}{\omega_2})| &\approx \frac{d}{d\tau} \ln |e^{-D_{22}\tau}| + \frac{d}{d\tau} \ln |A_2 A_1^2| - \frac{d}{d\tau} \ln |D_1^2 + [(\omega_2 + iD_{22}) - \omega_1]^2| = \\ &= -D_{22}\,. \end{aligned} \tag{3.34}$$

In conclusion, if the peaks are far enough from each other and the damping factor provide sharp peaks in the frequency domain, then the damping factors can be estimated by

$$D_{11} \approx -\frac{d}{d\tau} \ln |S(\tau, \frac{\omega_2}{\omega_1})| \quad \text{and} \quad D_{22} \approx -\frac{d}{d\tau} \ln |S(\tau, \frac{\omega_1}{\omega_2})|.$$

3.2.3 Many-component signal

Exactly the same analysis can be made for a signal $S_3(\omega)$ with three frequency components, with the same results. The CWT with the corresponding autocorrelation wavelet is then the sum of three pure frequency terms and six cross-terms.

The three first terms will give local maxima at $a = 1$ (indeed, they diverge for $a = 1$, as in the other cases) and the six other terms will cause local maxima at $a = \omega_j/\omega_k$; $j \neq k$, $j, k = 1, 2, 3$. We show in Figure 3.7 the graph of the absolute value of the CWT, $|S_3(\tau, a)|$, computed numerically for $A_1 = A_2 = A_3 = 1$, $D_1 = D_2 = D_3 = 1$, and $\omega_1 = 30$ rad/s, $\omega_2 = 60$ rad/s and $\omega_2 = 90$ rad/s, where the parameters have the same meaning as in the two-peak case. One sees indeed the maxima at $a = 1$ caused by the three first terms and the other six local maxima at the scales $a = \omega_j/\omega_k$; $j \neq k$, $j, k = 1, 2, 3$. This will yield six horizontal ridges for analyzing the signal and estimating the damping factors, as we did in the two-peak example.

Following the same pattern, we can propose a general expression for a CWT using the autocorrelation wavelet.

Let the signal $s_N(t)$ be a weighted sum of N Lorentzian components:

$$s_N(t) = \sum_{n=1}^{N} A_n e^{-D_n t} e^{i\omega_n t};\, D_n > 0. \tag{3.35}$$

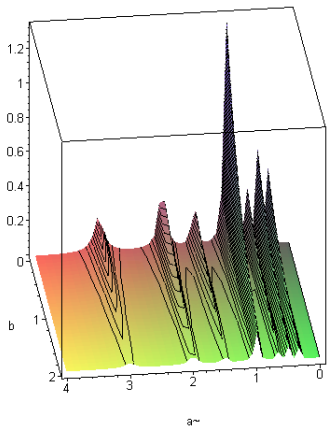

Figure 3.7: $|S_3(\tau, a)|$ for $A_1 = A_2 = A_3 = 1$, $D_1 = D_2 = D_3 = 1$, $\omega_1 = 30$ rad/s, $\omega_2 = 60$ rad/s and $\omega_2 = 90$ rad/s, $\tau \in [0, 2]$ and $a \in [0.1, 3], a \neq 1.0$

The Fourier transform of this signal is:

$$S_N(\omega) = 2\pi \sum_{n=1}^{N} A_n e^{i\varphi_n} \delta(\omega - (\omega_n + iD_n)). \tag{3.36}$$

The left truncated version of this signal reads as

$$s'_N(t) = \sum_{n=1}^{N} A_n e^{-D_n t} e^{i\omega_n t} \theta(t),\ D_n > 0\,. \tag{3.37}$$

Now the Fourier transform of (3.37) is given by

$$S'_N(\omega) = \sum_{n=1}^{N} \frac{A_n}{[D_n + i(\omega - \omega_n)]}\,. \tag{3.38}$$

Thus the autocorrelation of (3.37) in the frequency domain is

$$S_{s'_N s'_N}(\omega) = \left| \sum_{n=1}^{N} \frac{A_n}{D_n + i(\omega - \omega_n)} \right|^2\,. \tag{3.39}$$

Again, with the proper values of ω_n and D_n, the value of (3.39) can be considered numerically negligible at $\omega = 0$ and we can use this function as a wavelet function. Also, if the peaks are far enough from each other, we can make the approximation

$$\left| \sum_{n=1}^{N} \frac{A_n}{D_n + i(\omega - \omega_n)} \right|^2 \approx \sum_{n=1}^{N} \frac{A_n^2}{D_n^2 + (\omega - \omega_n)^2}\,, \tag{3.40}$$

so that the (approximate) autocorrelation wavelet function can be defined by

$$\Psi_N(\omega) = \sum_{n=1}^{N} \frac{A_n^2}{D_n^2 + (\omega - \omega_n)^2} \tag{3.41}$$

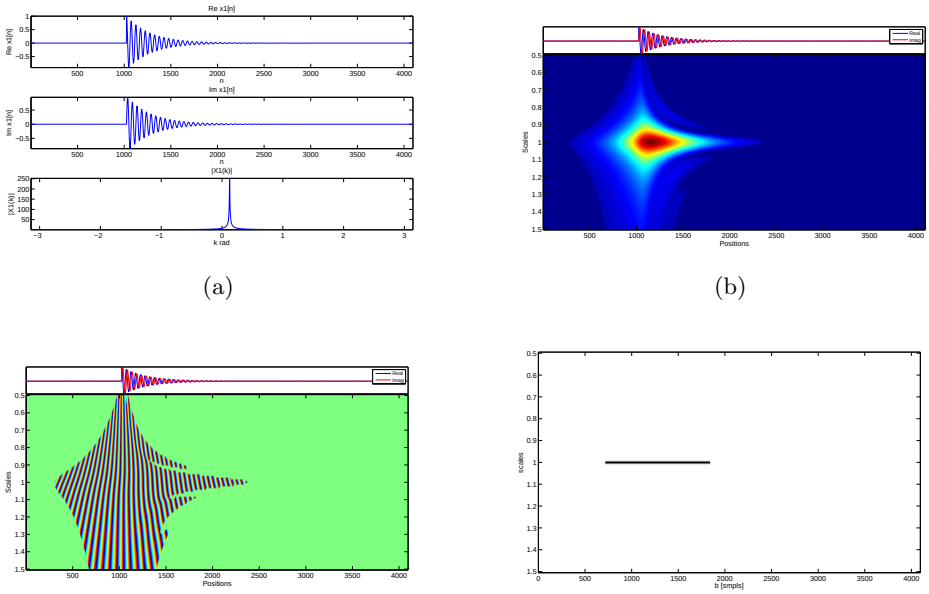

(a) (b)

(c) (d)

Figure 3.8: (a) Re $s_1[n]$, Im $s_1[n]$ and $|S_1[k]|$; (b) $|\mathrm{CWT}s_1[n]|$; (c) $\arg\{\mathrm{CWT}s_1[n]\}$ and (d) Skeleton of the CWT, for $A = 1$, $D_1 = 1$, $\omega_1 = 32$ rad/s, $n \in [1, 4096]$ and $a \in [0.5, 1.5]$ using the "Lorentz1d" wavelet.

The CWT of the signal (3.35), using (3.41) as wavelet function, is given in the frequency domain by

$$\begin{aligned} S_N(\tau, a) &= \sqrt{a} \int_{-\infty}^{\infty} \sum_{k=1}^{N} A_k e^{i\varphi_k} \delta(\omega - (\omega_k + iD_k)) \sum_{n=1}^{N} \frac{A_n^2}{D_n^2 + (a\omega - \omega_n)^2} e^{i\omega\tau} \, \mathrm{d}\omega \\ &= \sqrt{a} \sum_{k=1}^{N} s^{(k)}(\tau) \sum_{n=1}^{N} \frac{A_n^2}{D_n^2 + [a(\omega_k + iD_k) - \omega_n]^2} \end{aligned} \tag{3.42}$$

As in the previous section, this expression has a local maximum (or horizontal ridge) at $a = 1$ if the damping factors of the signal components are different from the wavelet components. In addition, the function $|S_N(\tau, a)|$ will have horizontal ridges at $a = \omega_n/\omega_k$, $k \neq n, k, n = 1, 2, ..., N$. Finally, one can estimate the damping factors from the lateral horizontal maxima lines at the scales $a \neq 1$, using the same procedure as before, under similar assumptions. And with them one can estimate the amplitudes as well.

Many assumptions were made in order to obtain the expression for CWT using the autocorrelation wavelet function from a FID signal model. One complicating factor arises if the frequency components are too close to each other, or some damping factor yields an unsharp peak in the frequency domain. Other difficulties occur if the signal is a sum of many multiplet metabolites with frequencies too close of each other, very different amplitudes between the components and/or the presence of strong noise. But theoretically, one can use the CWT to detect and quantify the parameters of the metabolite component.

In the next section we will analyse the numerical behavior of the CWT, for a truncated signal and in the presence of noise.

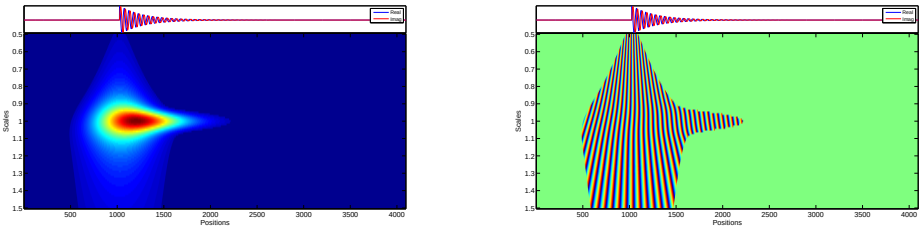

(a) (b)

Figure 3.9: (a) $|\mathrm{CWT}s_1[n]|$ and (b) $\arg\{\mathrm{CWT}s_1[n]\}$ for $A = 1$, $D_1 = 1$, $\omega_s = 32$ rad/s, $n \in [1, 4096]$ and $a \in [0.5, 1.5]$ using the Morlet wavelet.

3.3 Numerical analysis

In order to see what could happen when we analyse limited, discretized and noisy signals, we perform an evaluation using the YAWTB toolbox (Jacques et al., 2007), suitably expanded.

First we created a function called "Lorentz1d" which implements the expression given by (3.13), for $A_1 = 1$. This function was added to the YAWTB toolbox wavelet definitions. We also created a two peak and a three peak version of this function, called "Lorentz2Pk1d" and "Lorentz3Pk1d", respectively.

After that, we defined a discrete exponential signal (we use square brackets for emphasizing that the variable n is discrete)

$$s_1[n] = \begin{cases} 0, & 0 \leqslant n \leqslant \frac{N}{4} - 1, \\ A\, e^{-D_1(n-\frac{N}{4})t_s}\, e^{i\omega_1(n-\frac{N}{4})t_s}, & \frac{N}{4} \leqslant n \leqslant \frac{3N}{4} - 1, \\ 0, & \frac{3N}{4} \leqslant n \leqslant N - 1, \end{cases}$$

where $t_s = 1/f_s$ is the sampling period in seconds. We evaluate this function for $A = 1$, $D_1 = 1$, $\omega_1 = 32$ rad/s, $t_s = 1/256$ and $N = 4096$. We observe here that two new variables can be extracted from this expression. One is called D and is defined by $D = D_1 t_s = D_1/f_s$. The other one is the angular frequency k_0 defined by $k_0 = \omega_s t_s = \omega_s/f_s$. This can be important when one wants to use other wavelet functions defined in the YAWTB toolbox. Figure 3.8a presents the real part, the imaginary part and the absolute value of the Fast Fourier Transform (FFT) of this signal.

Next we calculate the CWT of this signal using the "Lorentz1d" function, with the same frequency and damping factor as the signal, for $a \in [0.5, 1.5]$. The absolute value, the argument and the skeleton of the CWT can be seen in the Figures 3.8b, 3.8c and 3.8d, respectively.

These figures show that the behavior predicted in the previous section indeed takes place. We can clearly see a local maximum at scale $a = 1$. In order to compare the result with a known wavelet, we also analyse this signal with the Morlet wavelet with the same frequency as the signal ($k_0 = \omega_1/f_s$) and with a width σ which reproduces approximately the width of the "Lorentz1d" wavelet (in this case, $\sigma = 250$). The absolute value of the CWT and its skeleton can be seen in Figures 3.9a and 3.9b.

As expected, we see the same local maximum at $a = 1$. But the first wavelet was tailor-made for the signal under analysis, so it amounts to a matched filter that can be used for detecting the presence of this component inside of a more complex signal. This application will be seen in more details in the next chapter.

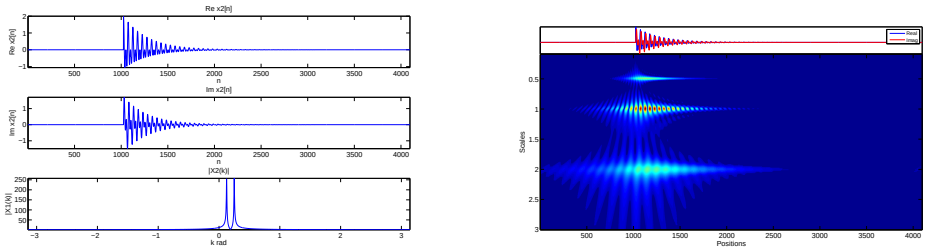

(a)

(b)

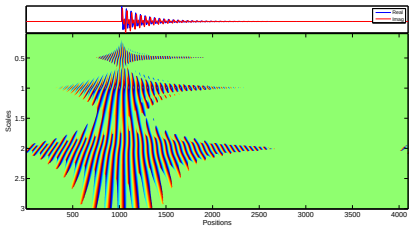

(c)

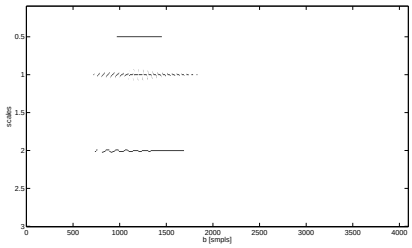

(d)

Figure 3.10: (a) $\mathrm{Re}\, s_2[n]$, $\mathrm{Im}\, s_2[n]$ and $|X2[k]|$; (b) $|\mathrm{CWT} s_2[n]|$; (c) $\arg\{\mathrm{CWT} s_2[n]\}$ and (d) Skeleton of CWT for $A_1 = A_2 = 1$, $D_1 = D_2 = 1$, $\omega_1 = 32$ rad/s and $\omega_2 = 64$ rad/s, $t_s = 1/256$ and $N = 4096$, using the "Lorentz2Pk1d" wavelet.

The next step is to define a two-peak signal $s_2[n]$ by:

$$s_2[n] = \begin{cases} 0, & 0 \leqslant n \leqslant \frac{N}{4} - 1, \\ A_1\, e^{-D_1(n-\frac{N}{4})t_s}\, e^{i\omega_1(n-\frac{N}{4})t_s} + A_2\, e^{-D_2(n-\frac{N}{4})t_s}\, e^{i\omega_2(n-\frac{N}{4})t_s}, & \frac{N}{4} \leqslant n \leqslant \frac{3N}{4} - 1, \\ 0, & \frac{3N}{4} \leqslant n \leqslant N - 1, \end{cases}$$

where $t_s = 1/f_s$ is the sampling period in seconds. We evaluate this function for $A_1 = A_2 = 1$, $D_1 = D_2 = 1$, $\omega_1 = 32$ rad/s and $\omega_2 = 64$ rad/s, $t_s = 1/256$ and $N = 4096$. Figure 3.10a shows the real part, the imaginary part and the absolute value of the FFT of this signal.

Then, we perform the CWT of this signal, using the "Lorentz2Pk1d" function with the same frequencies and damping factors as the signal, for $a \in [0.5, 1.5]$. The absolute value, phase and the skeleton of the CWT can be seen in Figures 3.10b, 3.10c and 3.10d, respectively.

Again we can see a strong local maximum at $a = 1$ and two smaller horizontal ridges at $a = \omega_1/\omega_2 = 0.5$ and $a = \omega_2/\omega_1 = 2$, as was predicted in the theoretical analysis. Moreover, the local maximum at $a = 1$ is truncated, as an effect of the interaction between the two frequency components at this scale, as we have seen in Figure 3.6. For the sake of comparison, we perform the analysis of $s_2[n]$ using Morlet wavelet, for $k_0 = \omega_1/f_s$, the frequency of the first component, and $\sigma = 250$. One should expect now only two local maxima at $a = 0.5$ and $a = 1.0$. The result can be seen in Figures 3.11a and 3.11b.

The same computations were made in order to test the three component signal $s_3[n]$ and the corresponding wavelet mentioned in the previous section, with entirely analogous results, but we will not reproduce them here.

Finally, we tried to verify the behavior of the CWT of the two signals $s_1[n]$, $s_2[n]$, constructed using the same frequencies and damping factors as the previous analysis, using their associated

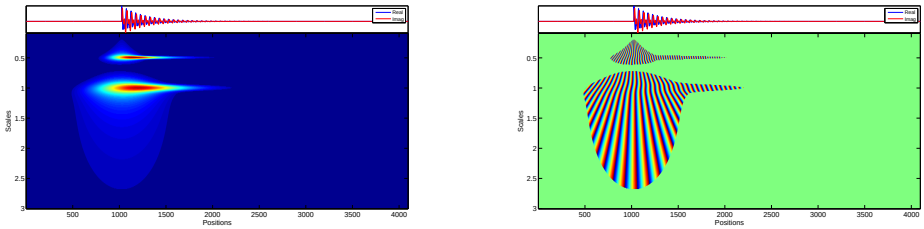

(a) (b)

Figure 3.11: (a) $|\mathrm{CWT}s_2[n]|$ and (b) $\arg\{\mathrm{CWT}s_2[n]\}$ for $A_1 = A_2 = 1$, $D_1 = D_2 = 1$, $\omega_1 = 32$ rad/s and $\omega_2 = 64$ rad/s, $t_s = 1/256$, $n \in [1, 4096]$ and $a \in [0.5, 1.5]$ using the Morlet wavelet.

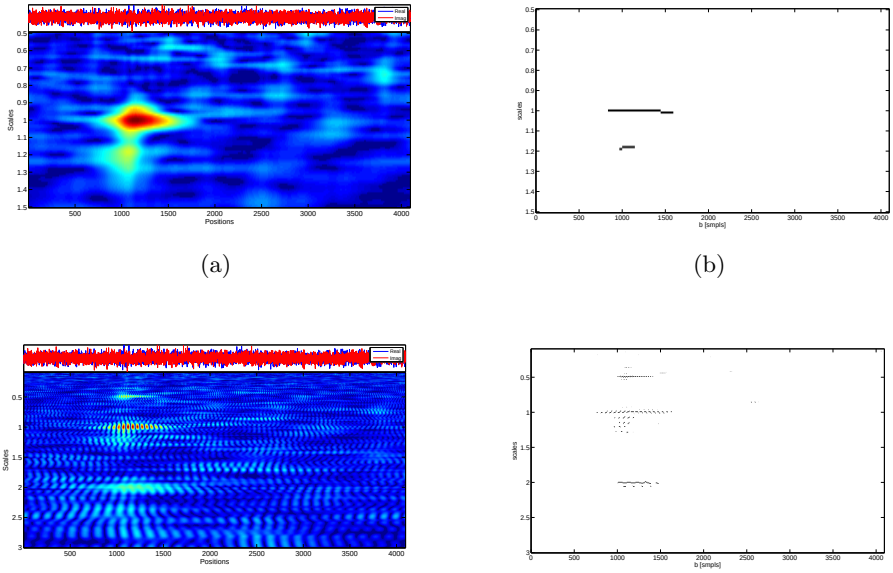

(a) (b)

(c) (d)

Figure 3.12: (a) $|\mathrm{CWT}\{s_1[n] + \text{noise}\}|$ and (b) its skeleton; (c) $|\mathrm{CWT}\{s_2[n] + \text{noise}\}|$ and (d) its skeleton; in all cases, we put SNR = -20dB and use the same parameters as in the previous analysis using the corresponding associated Lorentzian wavelet functions (Figures 3.8b and 3.10b).

wavelet functions, but now in the presence of noise. We decreased the signal to noise ratio (SNR) up to the limit of detection of the signals by the CWT (or when the local maximum still appears at $a = 1$). This happened when SNR $\geqslant$ -20dB in all cases. In Figures 3.12a and 3.12c we can see the absolute values of the CWT for the signals $s_1[n]$ and $s_2[n]$ and their skeletons, both with SNR ≈ -20dB, analysed with the corresponding associated wavelets (compare Figures 3.8b and 3.10b).

Although the performance of the detection proposed is good, we obtain a similar performance for the same signals, using the Morlet wavelet with "matched frequency and width" to the signals analysed, as above. This happens because here the Morlet wavelet used is large enough in time to have a good frequency resolution and noise discrimination. In Figures 3.13a - 3.13d we can see the absolute values of the CWT and its skeleton of the noisy signals using the Morlet wavelet for $k_0 = \omega_1/f_s$, and $\sigma = 250$.

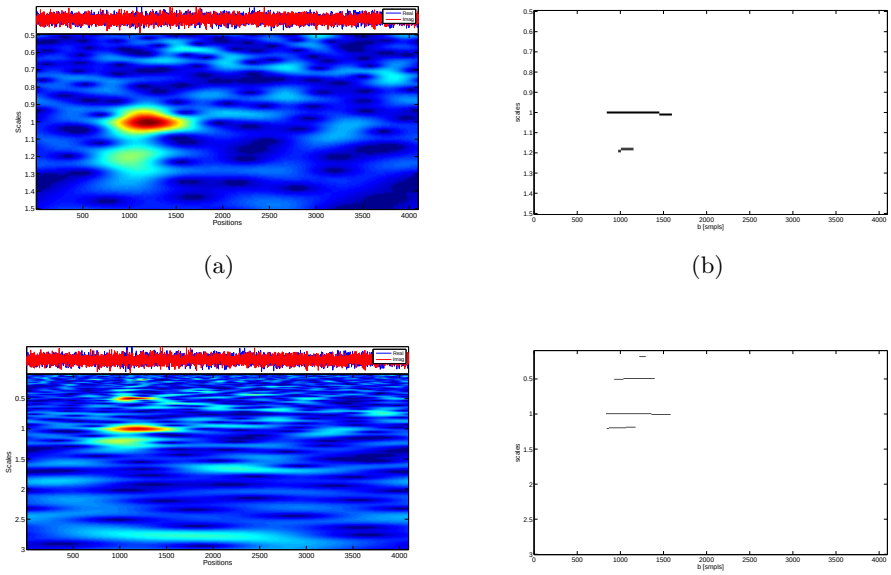

(a) (b)

(c) (d)

Figure 3.13: (a) $|\mathrm{CWT}\{s_1[n] + \text{noise}\}|$ and (b) its skeleton; (c) $|\mathrm{CWT}\{s_2[n] + \text{noise}\}|$ and (d) its skeleton, for the same parameters used in the previous analysis (Figures 3.9a and 3.11a, and SNR = -20 dB, using the Morlet wavelet.

3.4 Conclusion

Here we presented a way to construct wavelet functions based on the component to be detected in a more complex signal. We derived analytical expressions for the CWT when using a Lorentzian lineshaped signal as a starting point for the associated wavelet function. We also performed a numerical analysis with the YAWTB toolbox.

The first point is that, although we have an analytical expression for the CWT, we cannot yet estimate the signal parameters from it. Some effort should be made in order to investigate if those expressions can be simplified and then provide efficient estimators, as in the Morlet case presented in the previous chapter.

The second point is that, when a multiplet signal is used to create an autocorrelation wavelet, the cross-terms can make the detection of the signal more difficult in a more complex MRS signal, in particular if the amplitude of the components are very different from each other.

Finally, the numerical analysis with YAWTB and synthetic signals proved be consistent with the theoretical analysis. Also, the technique proved to be very efficient in the presence of noise, but using a Morlet wavelet with same width as the Lorentzian wavelet, we reached similar results.

We conclude this chapter with the obvious question: Will this technique work when more realistic signals are used to create wavelet functions, such as taken from a metabolite database for example? This will be answered in the next chapter.

Chapter 4

Wavelet analysis in MRS: Metabolite-based Wavelets for MRS

4.1 Introduction

So far, we have explored the well-known Morlet wavelet and derived more complex wavelets using the autocorrelation function of a given function to analyse MRS signals. The autocorrelation approach allowed us to obtain wavelets with two or more peaks in the spectrum. These new wavelets respond to the fact that most metabolite spectra are composed from several spectral peaks.

After the analytical description of the autocorrelation approach from a model signal given in the last chapter, we make here one step further, namely, we use the autocorrelation of metabolite profile sets to construct new wavelets and to identify metabolites in a MRS signal numerically. The idea is that those new wavelets reflect even better the spectral characteristics of the individual metabolites than the model functions used in the previous chapter. The resulting wavelets are supposed to work as a matched filter and to be able to identify metabolites in a complex MRS signal.

The problem that arises in this chapter is that only discrete data are available, no analytical description of the metabolite profiles. Therefore, our derived wavelets are discrete, too. Nevertheless, we show how to perform a continuous wavelet transform anyway by using interpolation. After that we present results of applying our metabolite-based wavelets for MRS.

4.2 Construction of metabolite-based wavelets

We derive our metabolite-based wavelets from metabolite profiles, which could have been acquired by MRS measurements of phantoms filled with single metabolites or by simulation in jMRUI. Each of those wavelets is supposed to be sensitive to one metabolite. It is thus necessary to construct mother wavelets with spectral characteristics similar to the ones of a certain metabolite. Therefore, we calculate the autocorrelation function (3.3) for the metabolite profile $s(t) = \phi_j(t)$, where $j = 1, \ldots, K$ refers to the index of a certain metabolite profile out of a number of K profiles.

The metabolite profile ϕ_j in MRS is a mixture of decaying, complex oscillations, so its autocorrelation values $R_j(t) \equiv R_{\phi_j\phi_j}(t)$ are complex, too. The magnitude of R_j rises from zero to the maximum before it decreases again, while R_j itself describes an oscillation. Out of that we obtain an admissible wavelet $\psi_j(t)$ by subtracting the mean,

$$\psi_j(t) = R_j(t) - \mathrm{E}\{R_j\}, \tag{4.1}$$

provided the mean $\mathrm{E}\{R_j\}$ is finite. Figure 4.1 shows an example wavelet. It has been derived from a simulated Creatine (Cr) profile (Figure 4.1a). The resulting Cr-based wavelet shows also two characteristic peaks like the original Creatine profile in the frequency domain (Figure 4.1b). In the time domain, however, the function is symmetrical with zero mean (Figure 4.1d) as required for an admissible wavelet.

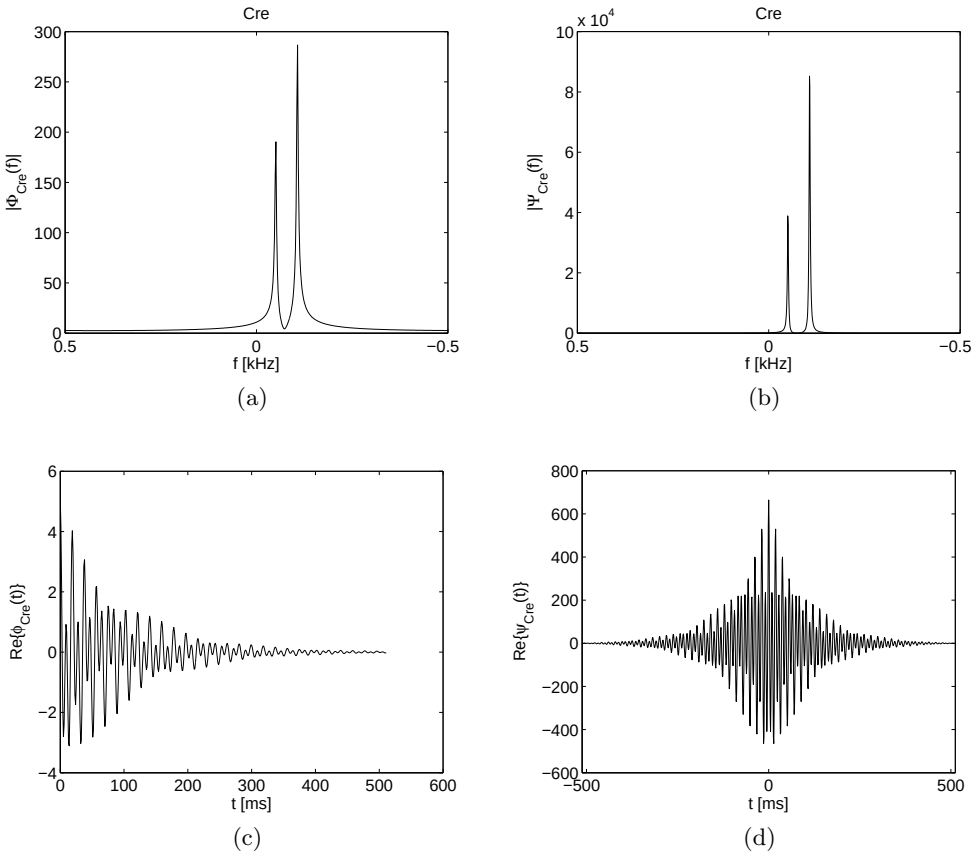

Figure 4.1: Wavelet constructed from Creatine (Cr) in vitro profile: (a) Modulus of the Cr profile spectrum (b) Cr-based wavelet spectrum, (c) Cr profile in the time domain, real part, and (d) Cr-based wavelet in the time domain, real part

This approach of using the autocorrelation function to find a new wavelet has already been explained in detail in Chapter 3. The difference is, however, that we do not use a model function for the metabolite profile $\psi_j(t)$ as in (3.6). Our metabolite profiles can be either measured or quantum mechanically simulated with NMRSCOPE (Graveron-Demilly et al. (1993)) and are hence both more complex and discrete. Thus we have to put in some more effort to apply the metabolite-based wavelets in the CWT.

4.3 Using metabolite-based wavelets

4.3.1 Performing the CWT with discrete mother wavelets

The outcome of measurements consists only of discrete data sets for the metabolite profiles. In order to perform the continuous wavelet transform, we need to dilate our constructed wavelets. Our solution is to upsample and downsample the mother wavelet according to the required scale

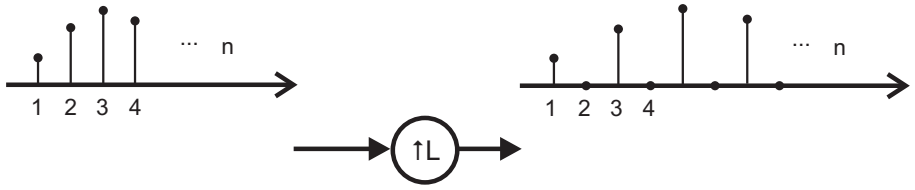

Figure 4.2: Interpolator: introduces zeros between the data points for upsampling by rate $L = 2$.

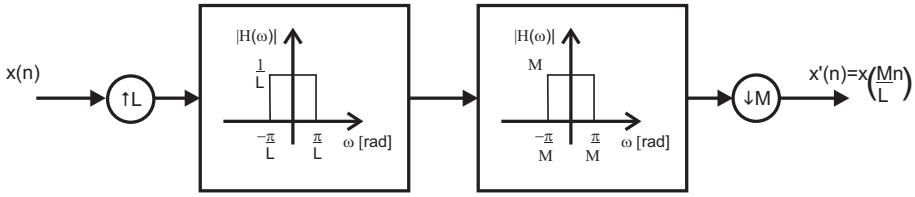

Figure 4.3: Complete upsampling and downsampling system to provide a function scaled by factor $a = L/M$.

$a = L/M$ as changing the scale corresponds to choosing another sampling frequency in the discrete case. This means that we have to design an algorithm different from the standard one for performing the CWT (Jacques et al., 2007). This new algorithm can be summarised as follows:

(a) First we generate the metabolite autocorrelation wavelet. After that we remove the mean value of that function;

(b) Now we have to generate the dilated versions of this wavelet in the time domain for all desired scales using the interpolator – decimator system proposed by Oppenheim et al. (1999). First, we expand the signal by an integer factor L using an interpolation scheme composed by inserting $L - 1$ zeros between the original samples and then interpolating these values by a low-pass digital filter with cutoff frequency of π/L rad, implemented by a Bartlett window of length $2L - 1$, as suggested in Oppenheim et al. (1999)). An example for upsampling by the integer factor of $L = 2$ is shown in Figure 4.2. Then, we decimate the signal by an integer factor M (keeping one sample for each M samples). In order to avoid aliasing, a low-pass filtering should be performed before the decimation operation. This is performed by a 128 tap Finite Impulse response (FIR) filter with cutoff frequency π/M rad using the MATLAB© function FIR1. The complete upsampling and downsampling concept is presented in Figure 4.3. With this procedure, our possible scales will be $a = L/M$.

(c) The next step is to make all versions of our wavelet aligned and zero padded in order to have the same size in a matrix, and perform a 1-D FFT to send them to the frequency domain;

(d) Finally we perform the CWT using a discretised version of (2.1), multiplying the signal spectra by all wavelet spectra and performing an IFFT.

Using the up- and downsampling approach, we can now dilate our discrete mother wavelets. For our example of the Cr-based wavelet from Section 4.2, we look at two different scales to show the effect. The time domain version at scale $a = 0.8$ and $a = 1.2$ can be seen in Figs. 4.4a and 4.4b, respectively.

4.3.2 Estimating the metabolite amplitude from the CWT

An *in vivo* MRS signal can be modelled as a linear combination of pure metabolite signal contributions s_j. Following Sima et al. (2009), we ignore lineshape distortions, baseline and water

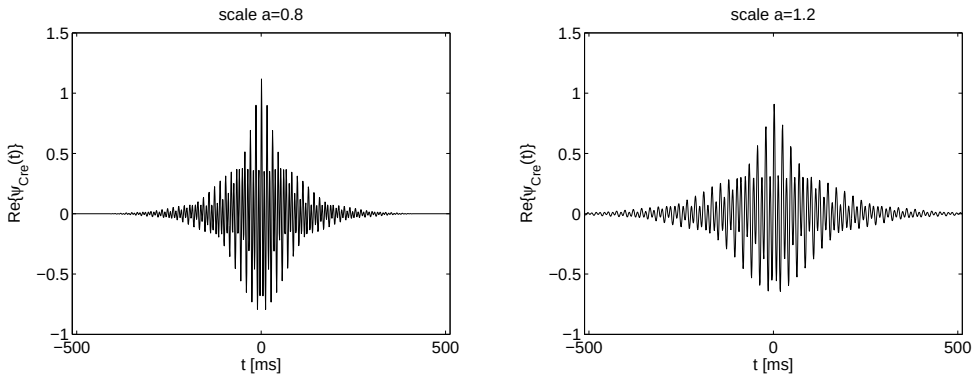

(a) (b)

Figure 4.4: Cr-based wavelet at (a) scale $a = 0.8$ and (b) $a = 1.2$.

contributions and describe an *in vivo* MRS signal by

$$s(t) = \sum_{j=1}^{M} s_j(t) + z(t) \equiv \sum_{j=1}^{M} A_j e^{-D_j t}\, e^{i(\omega_j t + \varphi_j)}\, \phi_j(t) + z(t) \tag{4.2}$$

where M is the number of metabolite signals, D_j is the Lorentzian damping correction, ω_j is the frequency shift, φ_j is the phase shift and A_j is the amplitude factor of the jth modelled metabolite signal. The term $z(t)$ models complex Gaussian white noise. The correction factors and shifts allow us to model the *in vivo* MRS signal from the metabolite basis set ϕ_j, which is either *in vitro* measured or quantum mechanically simulated.

If now each of our derived wavelets is assumed to be a matched filter for the corresponding metabolite, then the wavelet transform around a certain scale $a = a_r$ contains only a contribution of the metabolite of interest, let us say $s_m(t) = A_m e^{-D_m t}\, e^{i(\omega_m t + \varphi_m)}\, \phi_m(t)$, and thus we ignore all other metabolite terms in (4.2). So we can think of the following approximation:

$$\left| \int_{-\infty}^{\infty} S_{\tau,a_r} \{s(t)\}\, \mathrm{d}\tau \right| \approx \left| \int_{-\infty}^{\infty} S_{\tau,a_r} \{s_m(t)\}\, \mathrm{d}\tau \right|, \tag{4.3}$$

where m is the index of the metabolite of interest and $S_{\tau,a_r}\{s(t)\}$ denotes the WT of the signal $s(t)$ at translation τ and scale a_r. Then the amplitude A_m is calculated by

$$A_m \approx \frac{\left| \int_{-\infty}^{\infty} S_{\tau,a_r} \{s(t)\}\, \mathrm{d}\tau \right|}{\left| \int_{-\infty}^{\infty} S_{\tau,a_r} \left\{e^{-D_m t}\, e^{i(\omega_m t)}\, \phi_m(t)\right\} \mathrm{d}\tau \right|}. \tag{4.4}$$

Since we calculate the modulus of the wavelet transform, the phase $\exp(i\varphi_m)$ has dropped out. If the frequency shift is $\omega_m = 0$, the scale that matches the metabolite profile best is $a = 1$. In that case, (4.4) simplifies to

$$A_m \approx \frac{\left| \int_{-\infty}^{\infty} S_{\tau,a_r=1} \{s(t)\}\, \mathrm{d}\tau \right|}{\left| \int_{-\infty}^{\infty} S_{\tau,a_r=1} \{e^{-D_m t}\, \phi_m(t)\}\, \mathrm{d}\tau \right|} \tag{4.5}$$

As the metabolite profile ϕ_m is known and D_m can be estimated prior to the amplitude, the amplitude can be directly computed from (4.5).

However, this amplitude estimation is based on a number of assumptions such as the absence of frequency shift in the metabolite signal or a perfect filtering of the metabolite of interest by its corresponding wavelet.

In fact, (4.3) is a very rough approximation, since influences of other signal components than just the metabolite of interest are to be expected. Hence, it still needs to be generalised. We present now results of a Monte-Carlo simulation, which shows that our approach results in good estimation results for certain metabolites.

4.4 Analysing simulated data

The metabolite-based wavelets can be derived from either measured or simulated metabolite data. Examples for the latter case are presented in this section.

4.4.1 Metabolite database

For the examples shown in the sequel, we use a database that has been quantum mechanically simulated with NMRSCOPE (Graveron-Demilly et al. (1993)) using a PRESS sequence, an echo time of 30 ms, and a field strength of 1.5T. Within the database we have eight metabolites and two lipids which are summarised in Table 4.1.

NAA	N-Acetyl-Aspartate
Myo	Myo-Inositol
Cr	Creatine
Cho	Choline
Ala	Alanine
Tau	Taurine
Glu	Glutamate
Lac	Lactate
Lip1	lipid 1
Lip2	lipid 2

Table 4.1: Metabolite and lipid profiles included in our database.

Figure 4.5 shows the spectra of the profiles included in our database from which we have derived a metabolite-based wavelet for each metabolite. Using (4.2) we are also able to simulate specific *in vivo* spectra from the database and analyse them applying our metabolite-based wavelets.

4.4.2 Indicating the presence of metabolites in a signal

Figure 4.6a shows a noise free signal composed of all metabolites and lipids available from the database, Table 4.2 summarises the parameters used for modelling the signal as described by (4.2). The Lorentzian damping factor is set to be the same for all metabolite contributions. For simplicity, the frequency shift is set to zero and the phase shift is the same. Figure 4.6b shows exactly the same signal, but with the Lactate removed. The difference between the two spectra can be hardly seen. So, it is interesting to see what the metabolite-based wavelets can find in these signals.

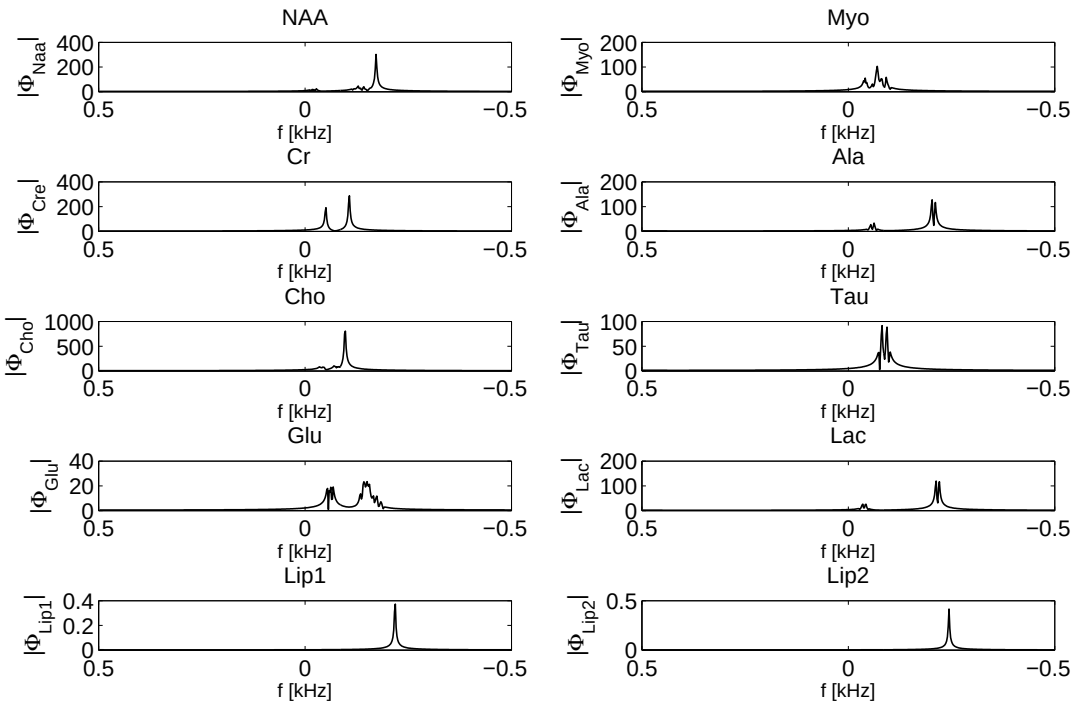

Figure 4.5: Spectra of the eight metabolites and two lipids included in the metabolite database.

profile	A_j	$D_j[\mathrm{s}^{-1}]$	$\omega_j[\mathrm{rad\,s}^{-1}]$	$\varphi_j[\mathrm{rad}]$
NAA	$44.5 \cdot 10^4$	0.012	0	-0.533
Myo	$31.7 \cdot 10^4$	0.012	0	-0.533
Cr	$44.4 \cdot 10^4$	0.012	0	-0.533
Ala	$25.3 \cdot 10^4$	0.012	0	-0.533
Cho	$37.9 \cdot 10^4$	0.012	0	-0.533
Tau	$0.02 \cdot 10^4$	0.012	0	-0.533
Glu	$8.1 \cdot 10^4$	0.012	0	-0.533
Lac	$36.9 \cdot 10^4$	0.012	0	-0.533
Lip1	$25.9 \cdot 10^4$	0.012	0	-0.533
Lip2	$0.12 \cdot 10^4$	0.012	0	-0.533

Table 4.2: Parameter values for amplitude A_j, Lorentzian damping factor D_j, frequency shift ω_j and phase shift φ_j for the simulation of the example *in vivo* MRS signal.

We perform a CWT on the composed signals for every metabolite-based wavelet that we have derived from our database (see Section 4.4.1). As a result, we have ten images of the CWT for each of the two composed signals from Figure 4.6. Additionally, we perform the analysis on pure metabolite-signals. More specifically, we use a specific metabolite-wavelet ψ_m and apply it to a signal $y_m = e^{-D_m t}\,\phi_m(t)$. We call y_m a pure metabolite signal as it is essentially the simulated *in*

vitro metabolite profile with *in vivo* damping. It serves as a reference for the transform obtained from the composed signals.

Here, we show three significant examples. These are the metabolites NAA, Cr and Lac. Their contributions to the composed signals are shown in Figure 4.7 and the appearences of the corresponding metabolite wavelets in Figure 4.8. While the major peak of NAA can be easily recognised in the spectra in Figure 4.6, the doublet Cr is well hidden under the other metabolite contributions. With Lac included in the spectrum (Figure 4.6a), we find peaks around frequencies of 0.25 kHz.

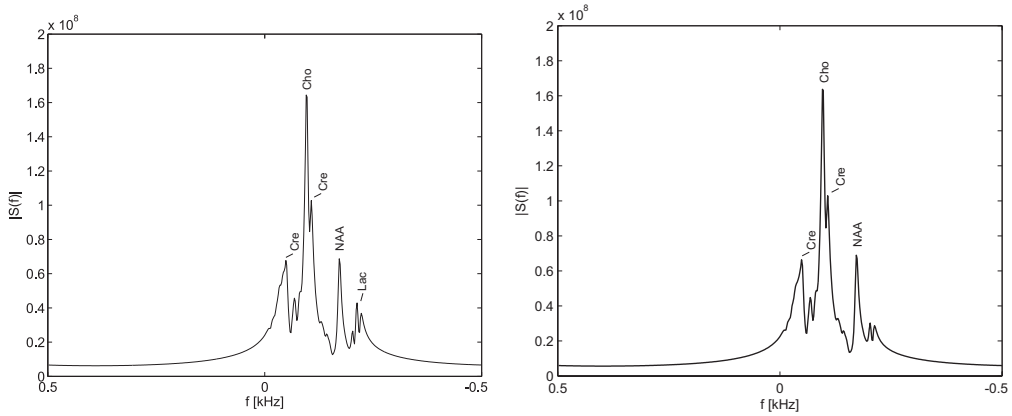

(a) (b)

Figure 4.6: Example of a simulated *in vivo* MRS signal: (a) including all metabolites and lipids from Table 4.1 and (b) the same as (a), but with the contribution of Lac removed.

Result for example with Lactate contribution

Figures 4.9 to 4.11 display the CWT on the pure metabolite signals and on the signal composed from all components available in our database including the contribution of Lactate. The wavelets used here are based on NAA, Cr and Lac. The upper panel of each figure presents the wavelet coefficients after the CWT in a scale-time representation. The lower panel shows the horizontal ridges as an indicator of local maxima of the coefficients along the time axis.

First, we look at the result for NAA. The CWT using the NAA-based wavelet on the pure NAA-reference signal (Figure 4.9a) shows a straight line of maxima at scale $a = 1$. We find a similar line when we look at the wavelet transform using the NAA-based wavelet on the composed signal (Figure 4.9b). Though there are some effects on lower scales, we have clear maxima values at scale $a = 1$, which indicate the presence of NAA in the analysed signal.

When applying the Cr-based wavelet on a Cr reference signal, local maxima result at scale $a = 1$ as shown in Figure 4.10a. That same characteristic maxima are present for the composed *in vivo* signal at scale $a = 1$ again, indicating the presence of Cr. Figure 4.10b shows presents that result. We find the same structure of local maxima at scale $a = 1.1$, too, as a response of the Cr-based wavelet on Cr-similar components in the composed signal, but for the identification of Cr in the signal only scale $a = 1$ is significant.

Finally, the Lac-based wavelet shows for the Lac reference signal and the composed signal a CWT result the same structure at scale $a = 1$. Again, this is how the presence of Lac in the composed signal is indicated. To verify this, we perform in the next section the analysis of the same composed signal, however, with the Lac contribution removed.

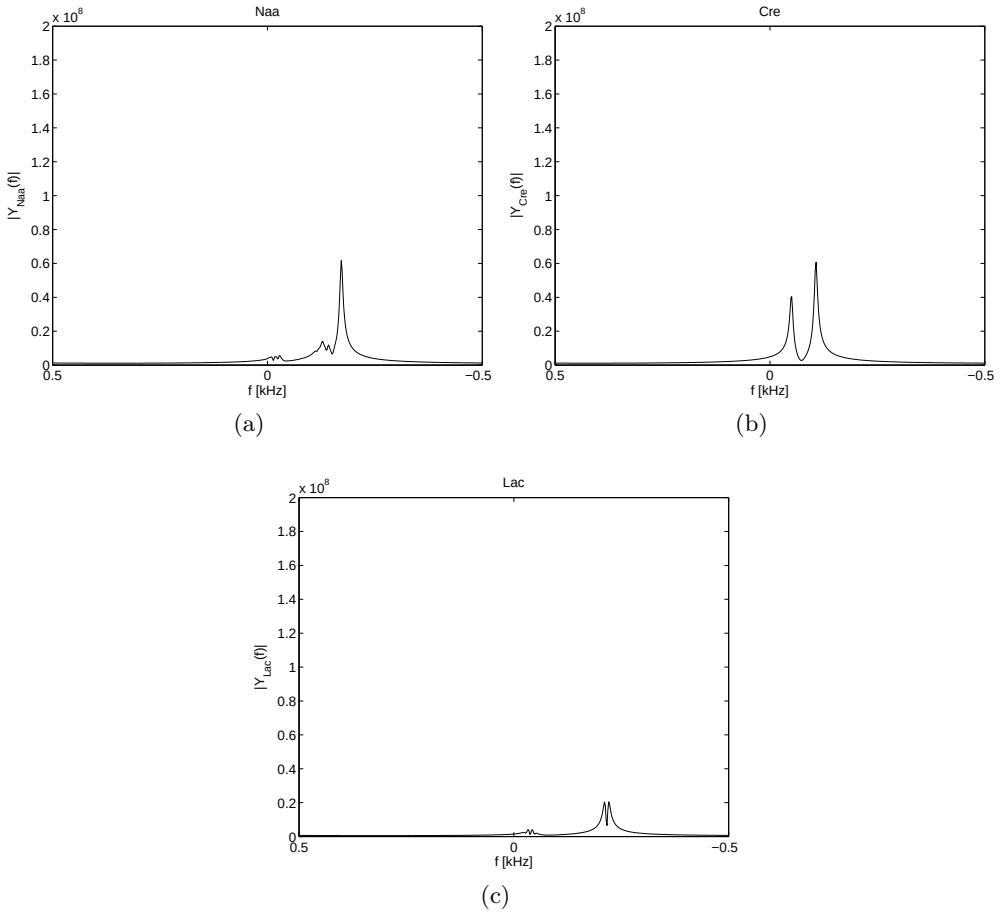

Figure 4.7: Just three of all components included in signal shown in Figure 4.6a. The Lac portion (c) is removed from the signal in Figure 4.6a and results in the signal seen in Figure 4.6b.

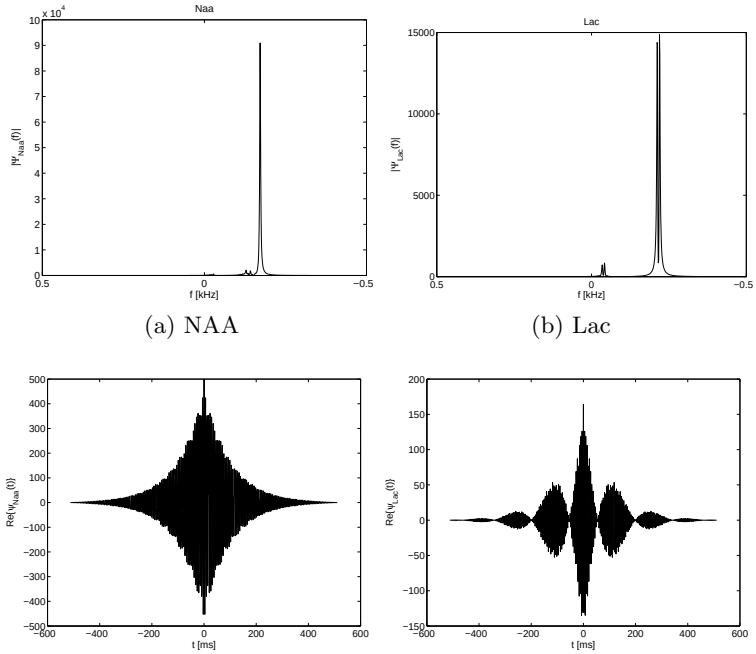

(a) NAA (b) Lac

(c) NAA (d) Lac

Figure 4.8: Example wavelets derived from the simulated metabolite profiles in frequency and time domain: (a,c) NAA-based wavelet and (b,d) Lac-based wavelet.

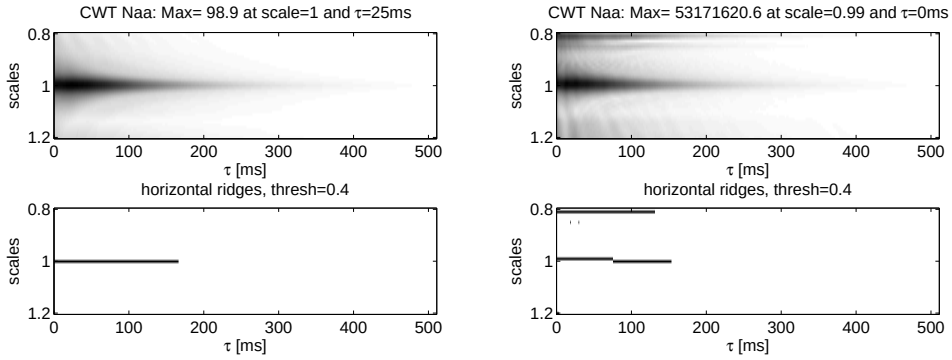

(a) (b)

Figure 4.9: CWT using the NAA-wavelet on (a) a pure NAA reference signal and (b) on the composed signal from Figure 4.6a. The presence of NAA is indicated by the local maxima at scale $a = 1$.

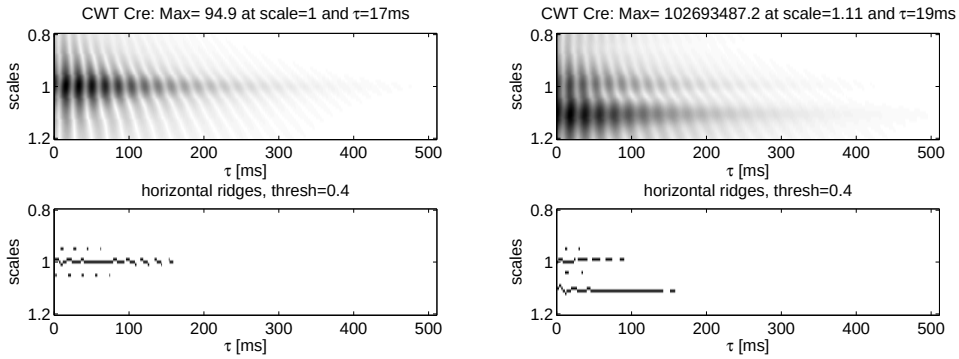

(a) (b)

Figure 4.10: CWT using the Cr-wavelet on (a) a pure Cr reference signal and (b) on the composed signal from Figure 4.6a. The presence of Cr is indicated by the local maxima at scale $a = 1$.

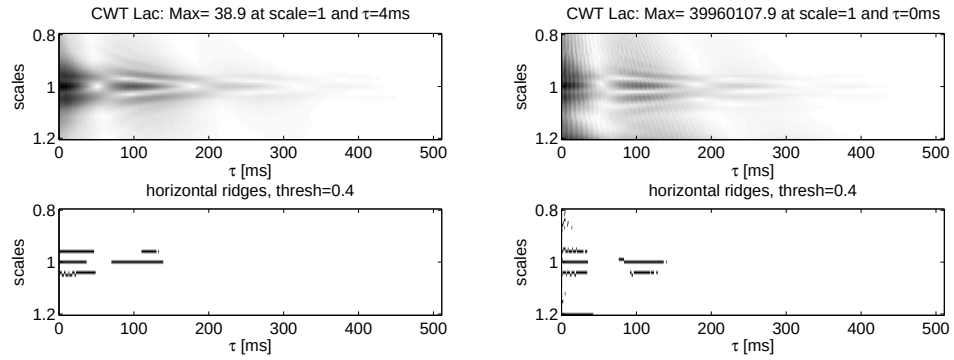

(a) (b)

Figure 4.11: CWT using the Lac-wavelet on (a) a pure Lac reference signal and (b) on the composed signal from Figure 4.6a. The presence of Lac is indicated by the local maxima at scale $a = 1$ both in (a) and in (b), as Lac is included in the composed signal.

Result for example without Lactate contribution

In this section, we look at what happens to our metabolite-based wavelet approach if we remove a metabolite contribution from a composed signal. Here, we analyse exactly the same signal as in Section 4.4.2, but after removal of the Lac contribution.

If we compare the results of the analysis of the signal with the NAA-based and the Cr-based wavelet (Figure 4.12 and Figure 4.13), respectively, we find the same behavior of the wavelet transform as in Section 4.4.2. There are only some minor differences in the amplitudes of the maximum CWT magnitude.

When it comes to performing the CWT with the Lac-based wavelet, although Lac is no longer included in the signal, we find that the transform behaves as in Figure 4.14. We see in 4.14b a structure similar to the local maxima as before in 4.11b. However, these are shifted in scale and belong actually to Alanine (Ala), as both metabolite profiles have a similar spectrum (see Figure 4.5). The high magnitudes at scale $a = 1$ are no longer present as Lac itself is not part of the composed signal. Thus, the use of the Lac-based wavelet is able to show us the presence of Lac in a signal.

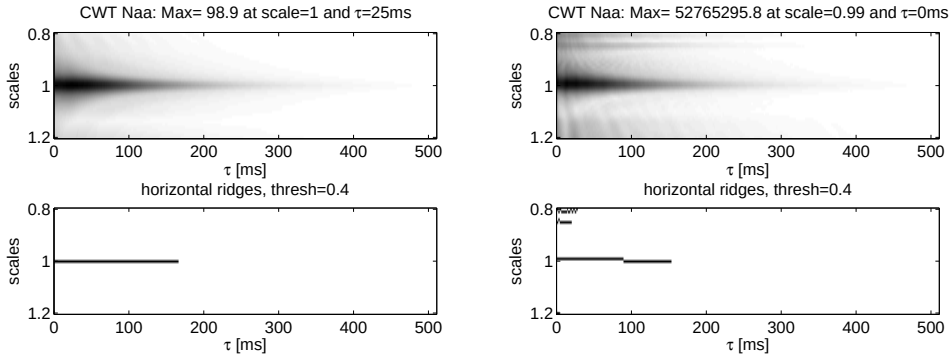

(a) (b)

Figure 4.12: CWT using the NAA-wavelet on (a) a pure NAA reference signal and (b) on the composed signal from Figure 4.6b. The presence of NAA is indicated by the local maxima at scale $a = 1.0$.

4.4.3 Estimating the metabolite signal amplitude

Up to here, we use the metabolite-based wavelets to indicate the presence of specific metabolites in a composed signal, simply by viewing local maxima in the wavelet transform. It is desirable to get more information out of the analysis. In this context, we have already discussed a way to estimate the amplitude of such a metabolite signal in Section 4.3.2. By means of a Monte Carlo simulation, we show that this is indeed possible.

Monte Carlo simulation setup

We simulated MRS signals according to the model (4.2) using the metabolite and lipid profiles from our metabolite data set. We have varied the amplitudes corresponding to mean values typical for normal tissues as in Sima et al. (2009). The phases have been chosen from the interval [-180°,180°] but set to be equal for all profile contributions per MRS signal simulated. The frequency shift

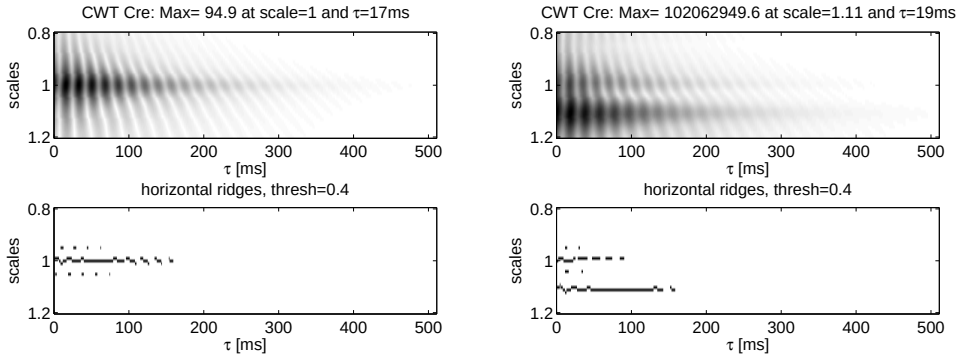

(a) (b)

Figure 4.13: CWT using the Cr-wavelet on (a) a pure Cr reference signal and (b) on the composed signal from Figure 4.6b. The presence of Cr is indicated by the local maxima at scale $a = 1.0$.

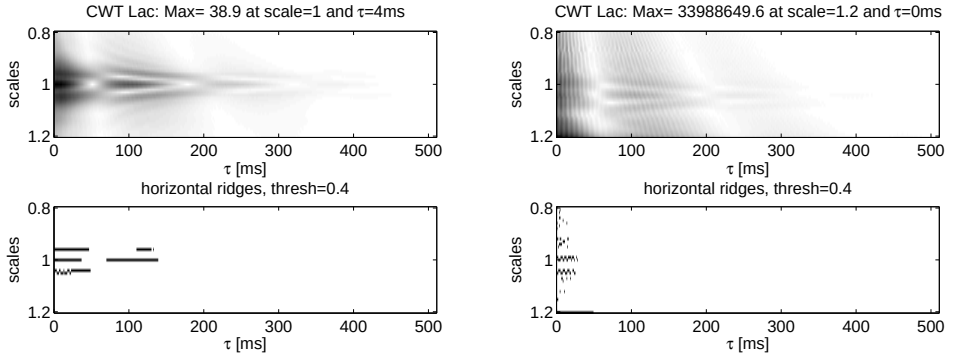

(a) (b)

Figure 4.14: CWT using the Lac-wavelet on (a) a pure Lac reference signal and (b) on the composed signal from Figure 4.6b. The presence or absence of Lac is indicated respectively by the local maxima at scale $a = 1.0$ both in (a) and (b) as Lac is not included in the composed signal.

were zero for simplicity reasons and the Lorentzian damping factor were varied around a mean value of $\mathrm{E}\{D\} = 0.0076$ with standard deviation $\sigma_D = 0.0030$.

To perform the Monte Carlo simulation we added complex Gaussian white noise to the composed signal and varied the signal-to-noise ratio between 0 dB and 40 dB. These values refer to

$$\mathrm{SNR} = 10\frac{P_S}{P_N}. \tag{4.6}$$

where P_N is the noise power and P_S is the signal power. The latter value is calculated from the square mean:

$$P_S = \frac{1}{N}\sum_{n=1}^{M} x^2[n] \tag{4.7}$$

where $x[n] = s[n] - z[n]$ is the discrete, noise free MRS signal from (4.2). As the signal $x[n]$ is composed from different metabolite profiles, the individual signal-to-noise ratio of the metabolite signals is thus different, but in general lower than that.

Monte Carlo simulation evaluation

For each value of the signal-to-noise ratio investigated, we created a set of $M = 2500$ signals and estimated the amplitudes of the metabolite signals. We focus on the results for the wavelet analysis based on the metabolites NAA, Cho, Cr, Lac and Myo. The amplitude is estimated following (4.5). However, as we have just discrete signals and wavelets available, we have to perform a discrete sum instead of an integral over the CWT values at scale $a = 1$.

$$A_m \approx \frac{\left| \sum_{q=1}^{Q} S(q,1) \right|}{\left| \sum_{q=1}^{Q} S_R(q,1) \right|}. \tag{4.8}$$

Here, $S_R(\tau, 1) = S_{\tau,1}\{\exp(-D_m t)\phi_m(t)\}$ is the reference CWT for the pure metabolite profile $\phi_m(t)$ and $S_R(q,1)$ is the discretised version, respectively, both at scale $a = 1$. How many values Q need to be summed up for an optimal result would be worth an independent investigation. We choose $Q_1 = 512$, which is the length of the original MRS signal, and we choose further half of it with $Q_2 = 256$.

For the estimated amplitude values we calculated the normalised mean square error (MSE). The MSE is

$$\text{MSE} = \frac{1}{M} \sum_{m=1}^{M} \frac{\left(\widetilde{A}_{j,m} - A_{j,m}\right)^2}{A_{j,m}} \tag{4.9}$$

where $j = 1 \ldots K$ is the index of the metabolite and lipid profiles, $\widetilde{A}_{j,m}$ is the estimated amplitude and $A_{j,m}$ is the true amplitude value.

Monte Carlo simulation results

The results of the Monte Carlo simulations for $Q_1 = 512$ and $Q_2 = 256$ is shown in Table 4.3 and Table 4.4. We see that in both cases the MRE values are generally decreasing with rising SNR. However, the results differ significantly from one metabolite to the other. While in Table 4.3 the MRE for NAA decreases from 10% down to 0.39%, for Cr the values go start at 71.14% and still show 39.16% at SNR= 40 dB. For Lac, too, the MRE remains 39.16% at SNR= 40 dB. For Myo, the errors are even higher. The best values are achieved for Cho, where the MRE goes down to 0.08%. Using just half the signal length with $Q_2 = 256$ for estimating the metabolite signal amplitudes, supplies similar values as seen in Table 4.4 and would thus be sufficient.

SNR	MSE [%]				
	NAA	Cho	Cr	Lac	Myo
0	10.02	1.47	71.14	360.00	4051.00
10	1.85	0.33	47.50	114.50	5057.00
20	0.31	0.04	16.72	28.68	464.40
30	0.44	0.10	34.96	44.72	4345.00
40	0.39	0.08	32.13	39.16	636.20

Table 4.3: Normalized Mean Square Errors in estimated amplitudes after $M = 2500$ iterations for each SNR, using $Q_1 = 512$ values to estimate the amplitudes.

SNR	MSE [%]				
	NAA	Cho	Cr	Lac	Myo
0	5.79	0.99	68.83	229.20	3340.00
10	1.07	0.21	46.03	66.78	2317.00
20	0.54	0.12	42.03	51.40	1128.00
30	0.28	0.04	20.72	35.29	444.60
40	0.50	0.13	42.48	50.43	624.70

Table 4.4: Normalized Mean Square Errors in estimated amplitudes after $M = 2500$ iterations for each SNR, using $Q_2 = 256$ values to estimate the amplitudes.

Looking at the results for Myo in Table 4.3, with MRE values between 4051 and 636, reveals that for this metabolite the amplitude estimation is not usable at all. The same is true for Cr and Lac. For these relatively weak contributions the influence of the other metabolites on the matched filter analysis using metabolite-based wavelets is too strong and thus cannot be ignored as suggested in Section 4.3.2. More complex estimation algorithms are required in that case. However, for strong metabolites signals such as NAA and Cho the amplitude estimation using the rough estimation algorithm presented here is successful.

4.5 Analysing *in vivo* spectra

The advantage of simulated data lies in the fact that it is if desired free of any distortion as presented earlier in this chapter. The current section now deals with examples from the real world as the metabolite profiles here are acquired by measurements and thus corrupted by noise.

4.5.1 *In vitro* metabolite database

In the sequel, we explore analysis examples exploiting a database from measured metabolite profiles. These *in vitro* metabolite profiles have been acquired on a 1.5 T Philips NT Gyroscan using a PRESS sequence with an echo time of 23 ms, and a PRESS box of 2x2x2 cm3. The data base has been used and described in further detail in Poullet et al. (2007). Figure 4.15 shows the profiles ordered like the simulated metabolite profiles in Figure 4.5. However, there is no *in vitro* Choline profile available in the database. So we use Phosphocholine (Pch) instead, which has a very similar spectrum. The two lipid were not measured but created from the Cr-profile. Again, we can derive a metabolite-based wavelet from each profile in Figure 4.15 and simulate specific *in vivo* spectra for further analysis.

4.5.2 Indicating the presence of a metabolite in *in vivo* signals

For our *in vivo* analysis example, we create a signal out of the metabolites in the database (4.15). In order to have the same amplitude range as in the example in Section 4.4.2 we multiply the *in vitro* metabolite profiles by a factor A_j given in Table 4.5. Also, we use the same damping, phase and frequency shifts as earlier in Section 4.4.2. Figure 4.16a shows the spectrum of the composed *in vivo* signal. As before, we focus on three metabolites – namely NAA, Cr and Lac – to perform an example analysis. The corresponding spectra of the composed signal lacking one of the three metabolites can be seen in Figure 4.16b to Figure 4.16d.

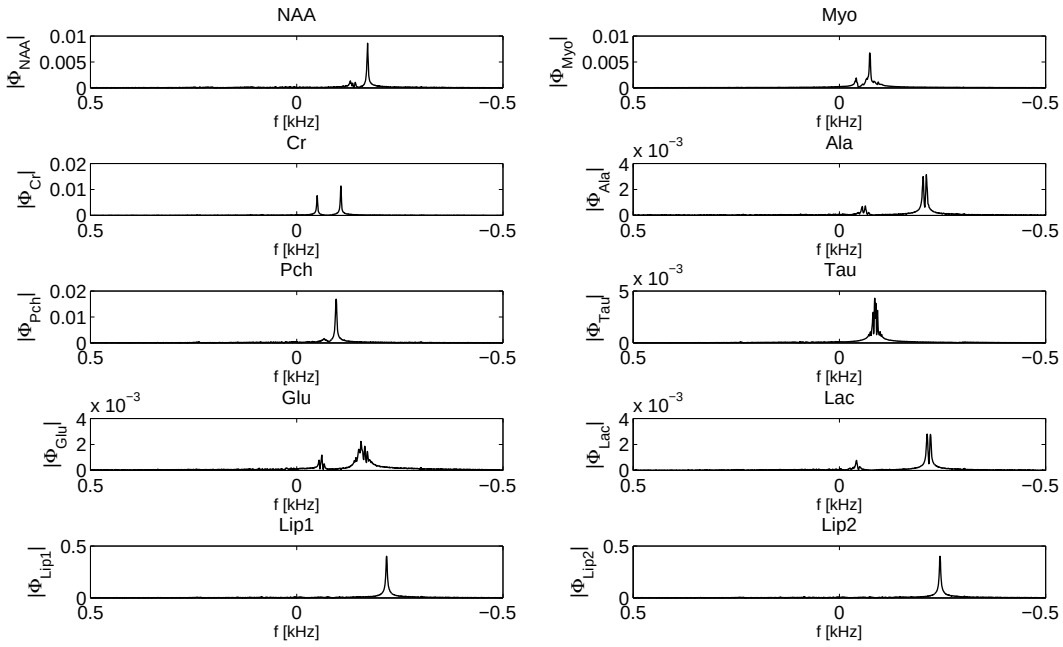

Figure 4.15: Spectra of the eight *in vitro measured* metabolites and the two derived lipids included in the *in vitro* database.

profile	A_j	$D_j[\mathrm{s}^{-1}]$	$\omega_j[\mathrm{rad\,s}^{-1}]$	$\varphi_j[\mathrm{rad}]$
NAA	$1.550 \cdot 10^{10}$	0.012	0	-0.533
Myo	$0.483 \cdot 10^{10}$	0.012	0	-0.533
Cr	$1.121 \cdot 10^{10}$	0.012	0	-0.533
Ala	$1.036 \cdot 10^{10}$	0.012	0	-0.533
Cho	$1.809 \cdot 10^{10}$	0.012	0	-0.533
Tau	$0.004 \cdot 10^{9}$	0.012	0	-0.533
Glu	$0.085 \cdot 10^{9}$	0.012	0	-0.533
Lac	$1.568 \cdot 10^{10}$	0.012	0	-0.533
Lip1	$0.239 \cdot 10^{6}$	0.012	0	-0.533
Lip2	$0.123 \cdot 10^{4}$	0.012	0	-0.533

Table 4.5: Parameter values for amplitude A_j for the simulation of the example *in vivo* MRS signal.

We perform the CWT on the composed signal using the NAA-based, the Cr-based and the Lac-based wavelet derived from the *in vitro* metabolite profiles. The wavelets are displayed in Figure 4.17. Serving as a reference for a true indication of the presence of the three metabolites, we remove each metabolite contribution separately and repeat the CWT. In addition, we apply the Lac-based wavelet that we derive from the simulated Lac profile in Section 4.4.1. The reason for the latter approach is that it would allow to use for various real life experiments wavelets built from the same metabolite database. Otherwise, a metabolite database would have to be acquired

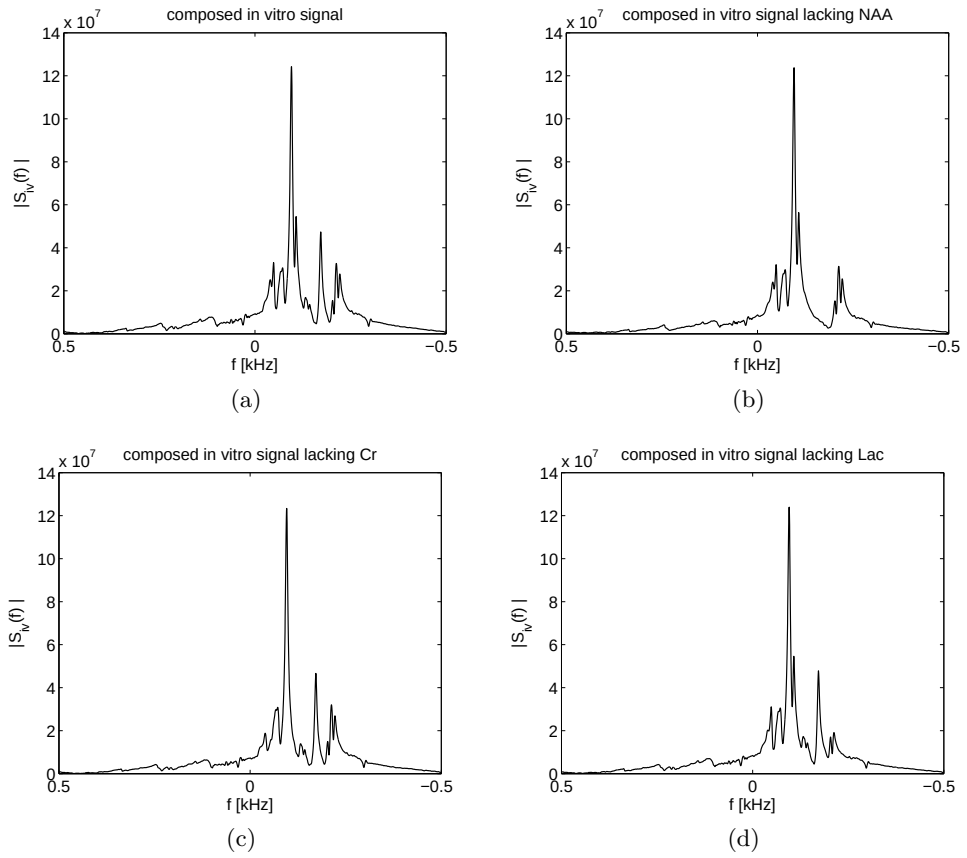

Figure 4.16: Example of an *in vivo* MRS signal: (a) including all metabolites and lipids from Table 4.5 and the same signal but lacking the contribution of (b) NAA, (c) Cr and (d) Lac .

for every individual MRS scanner.

Figures 4.18 to 4.21 show the results of the analysis. On the left in each figure, we see the CWT on the composed signal using a metabolite-based wavelet. On the right, the CWT is presented for the same signal, but lacking the metabolite for which the wavelet is specific to. The greyscale values are the same for all images. For NAA, we see a strong ridge at scale $a = 1$ if the metabolite is present (Figure 4.18a). That ridge is no longer present if the NAA contribution is removed (Figure 4.18b). The results for Cr in Figure 4.19 and Lac in Figure 4.20 share the same characteristic. The appearance of those results is similar to the figures for the example of simulated signals from Section 4.4.2.

However, strictly speaking, those results on the *in vivo* example are obtained here by using the metabolite-based wavelets on signals that originate from the same database. Therefore, it is interesting to see what happens if the wavelet is derived from a simulated metabolite profile and applied to the *in vivo* example. Figure 4.21 presents the outcome of that approach for Lac. When applied on the composed signal, the CWT yields the structure of local maxima characteristic for the Lac-based wavelet at scale $a = 1$ (Figure 4.20a). The analysis repeated on the same signal without any Lac contribution reveals that there is no Lac present any longer as the local maximum at scale $a = 1$ has disappeared (Figure 4.20b).

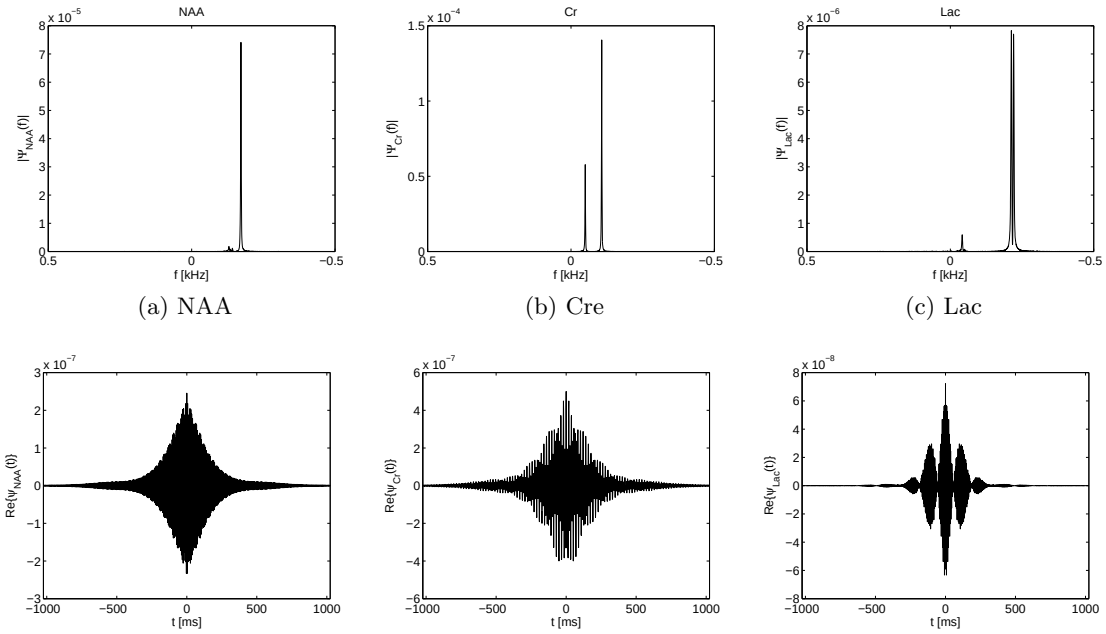

(a) NAA (b) Cre (c) Lac

(d) NAA (e) Cre (f) Lac

Figure 4.17: Example wavelets derived from the *in vitro* metabolite profiles in frequency and time domain: (a,d) NAA-based wavelet, (b,e) Cr-based wavelet, (c,f) Lac-based wavelet.

4.6 Conclusion

In Chapter 3, we have dealt with an analytical solution for using metabolite-based wavelets for synthetic signal models. Here, we took advantage of that approach and applied it to derive metabolite-based wavelets from two metabolite databases that have been acquired by simulation and *in vivo* derived from *in vitro* measured data, respectively.

We have shown that we can indicate the presence of a certain metabolite in a composed signal by using its specific metabolite-based wavelet. That signal can be either simulated or measured *in vitro*. However, this was based on visual evaluation of the wavelet coefficients. The next step would be a more automated analysis, based on a general criterion for the detection of a metabolite signal. The wish for that is based on the fact that, by using metabolite-based wavelets, we have a tool which identifies metabolite profiles of multiple spectral peaks at once. This differs from the usage of the well-defined single-peaked Morlet wavelet which has been presented in Chapter 2. The Morlet wavelet is capable of detecting single peaks in a composed signal spectrum and providing parameter estimates to describe the peaks, however, it does not separate different metabolite contributions.

Although there was no analytical expression for estimating the signal parameters from the general data-based solution presented in Chapter 3, we have found a rough approximation for estimating the amplitude of the metabolite signals. As a drawback, it depends heavily on the knowledge of the damping of the MRS signal. In addition, it is only applicable to the limited number of strong metabolite signals. Further efforts are necessary to combine all these findings into a complete algorithm that supplies information for quantifying the signals or at least contribute to other quantification algorithms.

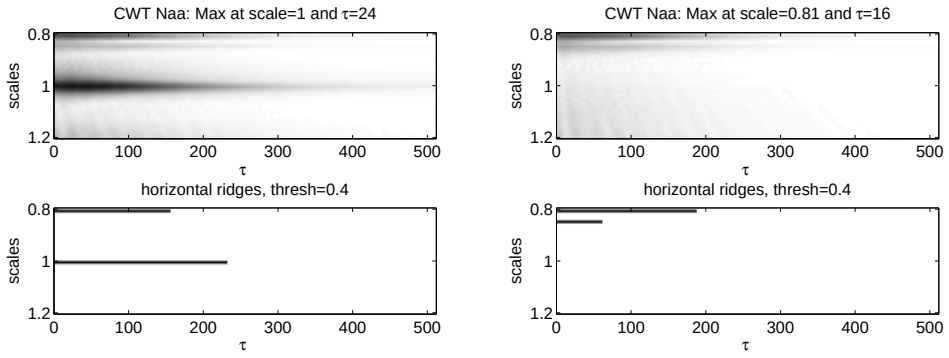

(a) (b)

Figure 4.18: CWT using the *in vitro* NAA-wavelet on (a) on the composed signal from Figure 4.16a and (b) on the composed signal lacking the NAA contribution. The presence of NAA is indicated by the local maxima at scale $a = 1$ in (a).

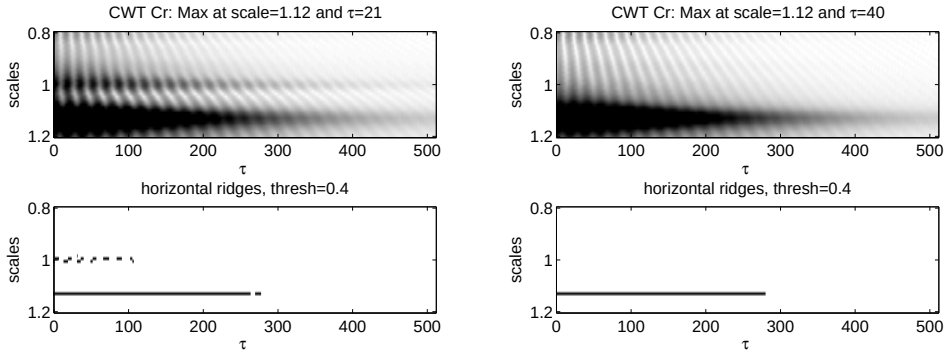

(a) (b)

Figure 4.19: CWT using the *in vitro* Cr-wavelet on (a) on the composed signal from Figure 4.16a and (b) on the composed signal lacking the Cr contribution. The presence of Cr is indicated by the local maxima at scale $a = 1$ in (a).

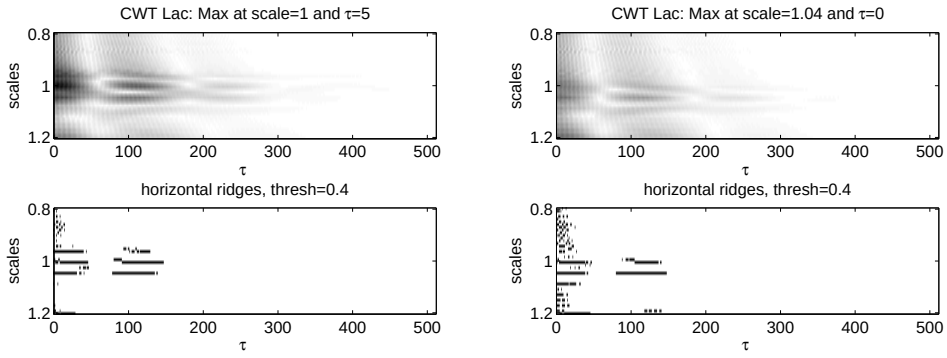

(a) (b)

Figure 4.20: CWT using the *in vitro* Lac-wavelet on (a) on the composed signal from Figure 4.16a and (b) on the composed signal lacking the Lac contribution. The presence of Lac is indicated by the local maxima at scale $a = 1$ in (a).

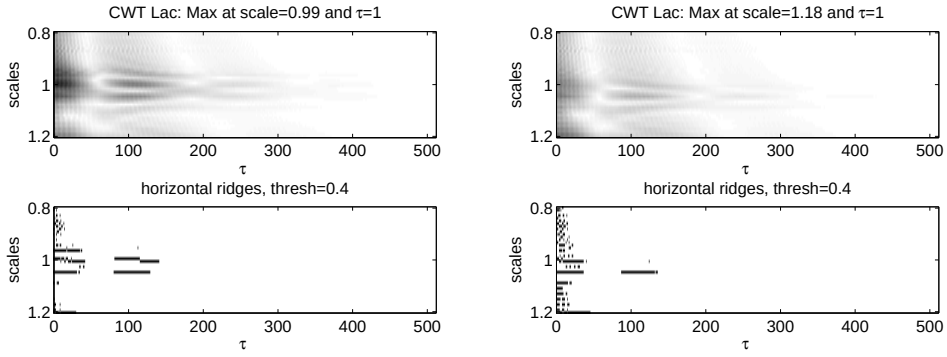

(a) (b)

Figure 4.21: CWT using the Lac-wavelet (from simulation) on (a) on the composed signal from Figure 4.16a and (b) on the composed signal lacking the Lac contribution. The presence of Lac is indicated by the local maxima at scale $a = 1$ in (a).

Chapter 5

Conclusion

In this e-book, we have presented three kinds of wavelets for use with the CWT in MRS application: the Morlet wavelet, the wavelets derived from the autocorrelation function of Lorentzian models and the wavelets derived from the autocorrelation function of the true metabolite signals. The performances of each type of wavelet are listed in Table 5.1.

In conclusion, which wavelet to use depends on the application one has in mind. The Morlet wavelet is good at analysing signals in the frequency domain, which is more familiar to a wider audience. However, using traditional time length sizes, it is severely influenced by noise and overlapping frequencies. Using longer wavelets, however, may alleviate the problem. In addition, the Morlet wavelet analyses the data at each frequency separately. Although this is beneficial if the signal is frequency-shifted, because there is no restriction on the form of the metabolites, it needs post-processing to find the right combination of amplitudes for each metabolite.

On the contrary, the wavelets derived from the autocorrelation of the Lorentzian model or from the metabolite signals are good at detecting the presence of a specific metabolite in an MRS signal by comparing the response at the scale $a = 1$ with other scales. It incorporates the information of the whole metabolite, not just one frequency as in the Morlet wavelet. Although, the *a priori* knowledge of metabolite profiles is needed for the detection, these wavelets work nicely on measured MRS signals even if a simulated profile is used to construct them. And theoretically, they can be used to estimate the signal parameters such as peak frequencies and damping factors. But before one can do that in practice, some work still needs to be done.

Morlet	Lorentzian Autocorrelation	Metabolite Autocorrelation
Sees frequency components $\Rightarrow$ easy to analyse signals in a familiar way	Information provided at scales $a = 1$ and $a = \omega_n/\omega_k$, $k \neq n, k, n = 1, 2, ..., N$, can be seen as an improvement of Morlet wavelet	Main information at scale $a = 1$, incorporates the shape of a metabolite = matched filter
Used as a standard method to compare signals from different experiments/simulations	Alternative method to find peaks in frequency or work as a matched filter. Interactive methods can be used to find the Lorentzian parameters (peak frequency and damping factor)	Could be an alternative method for detection of a specific metabolite
Easy to apply	Intermediate complexity of use, work better with some *a priori* information as number of peaks and its central frequency/damping factors	More complicated, higher time-consuming than the standard wavelets, needs *a priori* information (e.g. metabolite database)
Could be used as a benchmark of which damping function model is more appropriate for quantification	Theoretically can estimate damping factors	Estimate damping function is hard and depends on the metabolite
Able to derive amplitudes and damping function of each frequency component	Theoretically able to derive amplitudes and damping function of each frequency component	Able to derive amplitude if the damping function is known
Problems with overlapping frequencies/distinguishing between metabolites	Can identify frequency components	Can disentangle different metabolites in composed signals
Subject to noise/ sometimes needs denoising	Can detect components down to around -20dB SNR thanks to time length of the wavelet	Also robust against noise thanks to time length of the wavelet, could give good amplitude estimates to around +10dB SNR

Table 5.1: Comparison of the three kinds of continuous wavelets presented in this e-book.

Appendix A

The mathematics of the CWT

A.1 General definitions and properties

The continuous WT is a mathematical tool which permits to decompose a signal in terms of elementary contributions called wavelets. A large body of literature exists for wavelet analysis. We might refer the interested reader to the textbooks of Daubechies (1992), Torrésani (1995), Ali et al. (2000), Antoine et al. (2004), or the elementary introductions Antoine (1994) and Antoine (2000). These wavelets are obtained from a single function g by translations and dilations,

$$\psi_{(\tau,a)}(t) = \frac{1}{\sqrt{a}}\,\psi\left(\frac{t-\tau}{a}\right), \tag{A.1}$$

where the parameters of translation, $\tau \in \mathbb{R}$, and dilation, $a > 0$, may be continuous or discrete. The CWT of a signal s with the analysing wavelet g is the convolution of s with a scaled and conjugated wavelet $\psi_a(t) = \overline{\psi(-t/a)}/a$, where the overbar denotes complex conjugation :

$$\begin{aligned} S(\tau,a) \equiv S_{\tau,a}\{s(t)\} &= \psi_a * s(\tau) \\ &= \langle \psi_{\tau,a}, s\rangle = \frac{1}{\sqrt{a}}\int \overline{\psi\left(\frac{t-\tau}{a}\right)}\, s(t)\ \mathrm{d}t. \end{aligned} \tag{A.2}$$

It should be remarked that one uses often the so-called L^1-normalisation, with a factor $1/a$ in (A.1) and (A.2), instead of $1/\sqrt{a}$, in order to enhance small scales, where the finer details lie.

In the Fourier domain, the expression (A.2) takes the following form:

$$S(\tau,a) = \frac{\sqrt{a}}{2\pi}\int \overline{\Psi(a\omega)}\, S(\omega)\, e^{i\omega\tau}\ \mathrm{d}\omega, \tag{A.3}$$

where S and Ψ are the Fourier transforms[1] of the signal s and of the wavelet ψ, respectively. The equations (A.2) and (A.3) show clearly that the wavelet analysis is a time-frequency analysis, or, more properly, a time-scale analysis (the scale parameter a behaves as the inverse of a frequency). In particular, the relation (A.3) shows that the CWT of a signal s is a filter with a constant relative bandwidth $\Delta\omega/\omega = \text{const}$.

Then a straightforward calculation shows that this transform conserves energy (in the sense of signal processing), that is,

$$\iint |S(\tau,a)|^2\,\frac{\mathrm{d}a\ \mathrm{d}\tau}{a^2} = c_\psi \int_{-\infty}^{\infty} |s(t)|^2\ \mathrm{d}t. \tag{A.4}$$

[1] We use the asymmetric Fourier transform: $S(\omega) = \int s(t)\, e^{-i\omega t}\ \mathrm{d}t,\ s(t) = \frac{1}{2\pi}\int S(\omega)\, e^{i\omega t}\ \mathrm{d}\omega$

Clearly we must require the wavelet ψ to satisfy the so-called admissibility condition, namely,

$$c_\psi \equiv 2\pi \int |\Psi(\omega)|^2 \frac{\mathrm{d}\omega}{|\omega|} < \infty. \tag{A.5}$$

Eq. (A.4) means that the CWT is an isometry from the space of signals onto a closed subspace $\mathcal{H}_\psi$ of $L^2(\mathbb{R}^2_+, \mathrm{d}a\,\mathrm{d}\tau/a^2)$, where $\mathbb{R}^2_+$ denotes the scale-position half-plane $\mathbb{R}^2_+ = \{(\tau, a), \tau \in \mathbb{R}, a > 0\}$. Therefore, the CWT may be inverted on its range $\mathcal{H}_\psi$ by the adjoint map – and this gives an *exact* reconstruction formula:

$$s(t) = c_\psi^{-1} \iint \psi_{(\tau,a)}(t)\, S(\tau, a)\, \frac{\mathrm{d}a\,\mathrm{d}\tau}{a}. \tag{A.6}$$

This formula may also be interpreted as an expansion of the signal into the wavelets $\psi_{(\tau,a)}$, with (wavelet) coefficients $S(\tau, a)$.

A necessary (and almost sufficient) condition for admissibility is that the wavelet have no DC component:

$$\Psi(0) = 0 \quad \Longleftrightarrow \quad \int g(t)\ \mathrm{d}t = 0. \tag{A.7}$$

This is in fact the admissibility condition that is used in practice.

This transform is very general in the sense that there is one CWT for each choice of the analysing wavelet g. For each application, one should select an analysing wavelet adapted to the type of signal at hand. For instance, in order to detect and to characterize the singularities of a signal (Muzy et al., 1993) or a curve (Antoine et al., 1997), it is advantageous to use as analysing wavelet a derivative of the Gaussian, for instance, the familiar *Mexican hat*,

$$\psi_{_H}(x) = (1 - x^2)\, e^{-x^2/2} \quad \Leftrightarrow \quad \Psi_{_H}(\omega) = \sqrt{2\pi}\, \omega^2\, e^{-\omega^2}. \tag{A.8}$$

In our case, MRS signals are relatively well defined in frequency, so it is more interesting to use analysing wavelets which are well localized in frequency space. This is the case of the Morlet wavelet, defined by

$$\psi_{_M}(t) = e^{i\omega_0 t}\, e^{-t^2/(2\sigma^2)} + h(t) \quad \Leftrightarrow \quad \Psi_{_M}(\omega) = \sqrt{2\pi}\, \sigma\, e^{-(\omega-\omega_0)^2\sigma^2/2} + H(\omega), \tag{A.9}$$

where the correction term h is necessary to enforce the admissibility condition. If $\omega_0\sigma$ is sufficiently large (typically $\omega_0\sigma > 5.5$), then h is numerically negligible, and will indeed be omitted. The Morlet wavelet can be interpreted as a bandpass linear filter centered around $\omega = \omega_0/a$ of weight $1/(\sigma a)$ (Figure A.1).

All the results presented in Chapter 2 have been obtained with the Morlet wavelet, but they can easily be generalized to any analysing wavelet whose Fourier transform has a single maximum at $\omega = \omega_0$, or even to the Short Time Fourier Transform (STFT)[2] (Delprat et al., 1992).

Another class of wavelets, incorporating as much *a priori* information as possible, is that of the autocorraltion wavelets, developed in Chapter 3. On the theoretical side, the idea is simply to start from the autocorrelation function of a signal and substract its mean, assuming it is finite. The resulting function is an admissible wavelet, well adapted to the signal in question. Note that this idea is very close to that of the subtraction wavelets, obtained by taking the difference between a scaling function h (a bump) and a slightly dilated version of it, that is,[3]

$$\psi_h^{(a)}(t) = h(t) - \frac{1}{a} h\Big(\frac{t}{a}\Big)\ (a > 1).$$

[2]The STFT is obtained by replacing scaling by modulation in the definition of the wavelets, that is, replacing Eq. (A.1) by $\widetilde{\psi}_{(\tau,a)}(t) = e^{it/a}\, \psi(t - \tau)$.

[3]This technique goes back to astronomers, who call it "fuzzy masking".

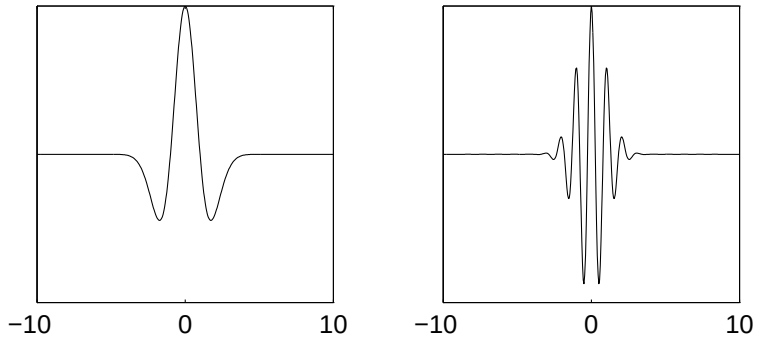

Figure A.1: Two usual one-dimensional wavelets: (left) The Mexican hat or Marr wavelet; (right) The real part of the 1-D Morlet wavelet, for $\omega_0 = 5.6$.

The prototype is the Difference-of-Gaussians or DOG wavelet, obtained by choosing for $h(t)$ a Gaussian, which is a good substitute for the the Mexican hat wavelet, frequently used in psychophysics works (Daugman, 1980; Valois and Valois, 1988; Grossmann et al., 1990) However, applying the same technique to a realistic MRS signal, as we did in Chapter 4, requires an extra interpolation step, in order to obtain a discrete wavelet adapted to the metabolite data, which are discrete by necessity.

An important fact is the so-called reproduction property. Indeed it may be shown that the orthogonal projection P_ψ from $L^2(\mathbb{R}^2_+,\, \mathrm{d}a\,\mathrm{d}\tau/a^2)$ onto the closed subspace $\mathcal{H}_\psi$ (the space of wavelet transforms) is an integral operator, with kernel

$$K(\tau', a'; \tau, a) = c_\psi^{-1} \langle \psi_{(\tau',a')} | \psi_{(\tau,a)} \rangle. \tag{A.10}$$

In other words, a function $f \in L^2(\mathbb{R}^2_+,\, \mathrm{d}a\,\mathrm{d}\tau/a^2))$ is the WT of some signal iff it satisfies the reproduction identity

$$f(\tau', a') = \iint K(\tau', a'; \tau, a)\, f(\tau, a)\, \frac{\mathrm{d}a\,\mathrm{d}\tau}{a^2}. \tag{A.11}$$

For this reason, K is called the *reproducing kernel* of ψ. It is also the autocorrelation function g and as such it plays an essential role in calibrating the CWT (Antoine, 1994).

Remark: Notice that the measure $\mathrm{d}a\ \mathrm{d}\tau$ on $\mathbb{R}^2_+$ is invariant under dilations and translations. This is no accident. Indeed the CWT may be derived by considering the group of dilations and translations of the real line. The relation $\big(U(\tau, a)\psi\big)(t) = a^{1/2}\psi_{(\tau,a)}(t)$ defines a unitary representation of this group in the space $L^2(\mathbb{R})$ of signals, and this representation is *square integrable*, which means that there exists nonzero functions $g \in L^2(\mathbb{R})$ such that the matrix element $\langle U(\tau, a)\psi | \psi \rangle$ is square integrable with respect to the invariant measure $\mathrm{d}a\,\mathrm{d}\tau/a^2$. These are precisely the admissible wavelets, since a direct calculation shows that

$$\iint |\langle U(\tau, a)\psi | \psi \rangle|^2\, \frac{\mathrm{d}a\,\mathrm{d}\tau}{a^2} = c_\psi\, \|\psi\|^2, \tag{A.12}$$

i.e., ψ is admissible iff $c_\psi < \infty$. All the properties of the CWT described above follow from these facts (Daubechies, 1992; Antoine, 1994).

Now the relation (A.11) shows that the CWT is enormously redundant (the signal has been unfolded from one variable t to two variables (τ, a)). Thus it is not surprising that the whole information is already contained in a small subset of the values of $S(\tau, a)$. An example of such

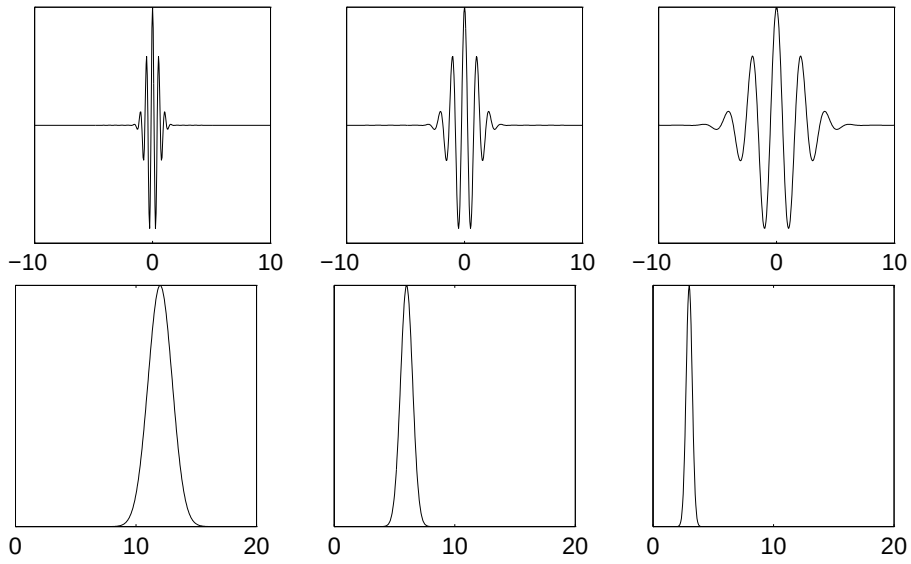

Figure A.2: Support properties of the Morlet wavelet g_M: for $a = 0.5, 1, 2$ (left to right), $\psi_{(\tau,a)}$ has width 3, 6, 12, respectively (top), while $\Psi_{(\tau,a)}$ has width 3, 1.5, 0.75, and peaks at 12, 6, 3 (bottom).

a subset is the so-called *skeleton*, that is, the set of *ridges*, which are essentially the lines of maxima of the modulus of the WT (in the case of a monochromatic signal, the ridges become horizontal lines $a = a_r$, as we have seen in Section 2.1). Another example is obtained by taking an appropriate discrete subset $\Gamma = \{a_j, \tau_k\}$ of the half-plane $\mathbb{R}^2_+$, as it is necessary in any case for numerical evaluation of the integrals. However, for most wavelets g, the resulting family $\{\psi_{(a_j,\tau_k)}\}$ is *never* an orthogonal basis (for the Morlet wavelet, for instance, the kernel K is a Gaussian, thus it never vanishes). At best, it is an overcomplete set of vectors, technically called a *frame*, provided Γ contains sufficiently many points (Daubechies, 1992).

A.2 Localization properties and interpretation

The main virtues of the CWT follow from the support properties of ψ. Assume g and G to be as well localized as possible (compatible with the Fourier uncertainty principle). More specifically, assume that ψ has an 'essential' support of width L, centered around 0, while Ψ has an essential support of width Ω, centered around ω_0. Then the transformed wavelets $\psi_{(\tau,a)}$ and $\Psi_{(\tau,a)}$ have, respectively, an essential support of width aL around τ and an essential support of width Ω/a around ω_0/a. This behavior is illustrated in Figure A.2, which shows the Morlet wavelet in the time and frequency domains, for three successive scales $a = 0.5, 1$ and 2, from left to right.

Notice that the product of the two widths is constant. We know it has to be bounded below by a fixed constant, by the (Fourier) uncertainty principle. We illustrate this vital fact in Figure A.3, which is a time-frequency representation. Remember that $1/a$ behaves like a frequency. Therefore:

- if $a \gg 1, \psi_{(\tau,a)}$ is a wide window, whereas $\Psi_{(\tau,a)}$ is very peaked around a small frequency ω_0/a: this transform is most sensitive to *low frequencies*.
- if $a \ll 1, \psi_{(\tau,a)}$ is a narrow window and $\Psi_{(\tau,a)}$ is wide and centered around a high frequency

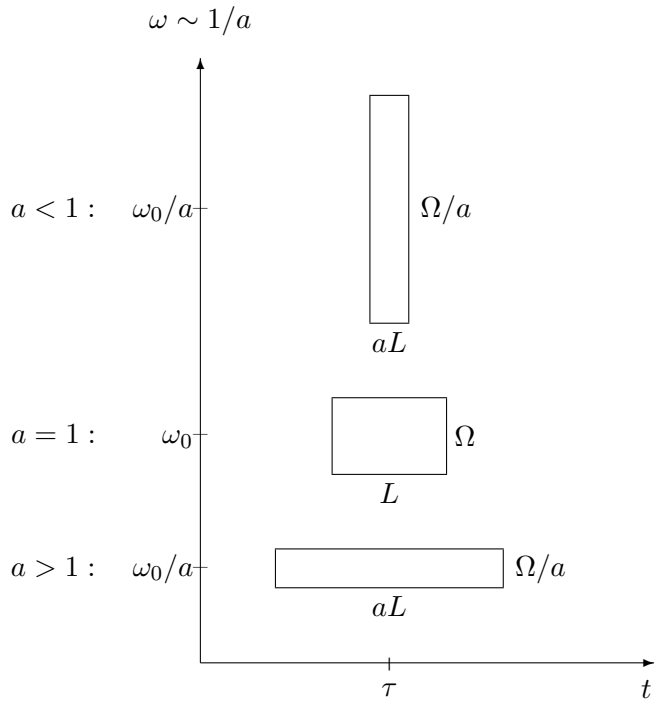

Figure A.3: Support properties of $\psi_{(\tau,a)}$ and $\Psi_{(\tau,a)}$.

ω_0/a: this wavelet has a good localization capability in the space domain and is mostly sensitive to *high frequencies*.

Combining now these localization properties with the zero mean condition and the fact that $\psi_{(\tau,a)}$ acts like a filter (convolution), we see that the CWT performs a *local filtering*, both in time and in scale. The WT $S(\tau, a)$ is nonnegligible only when the wavelet $\psi_{(\tau,a)}$ matches the signal $s(t)$, that is, it filters the part of the signal, if any, that lives around the time τ and the scale a.

Taking all these properties together, one is naturally led to the interpretation of the CWT as a *mathematical microscope*, with optics g, position τ and global magnification $1/a$ (Arnéodo et al., 1991). In addition, the analysis works at constant relative bandwidth ($\Delta\omega/\omega =$ constant), so that it has a better resolution at high frequency, i.e., small scales. This property makes it an ideal tool for detecting *singularities* (for instance, discontinuities in the signal or one of its derivatives), and also scale dependent features, in particular, for analysing *fractals* (Arnéodo et al., 1991).

A.3 Implementation questions

Faced with this new tool, one must begin by learning the rules of the trade, that is, one must learn how to read and understand a CWT (Grossmann et al., 1990). The simplest way is to get some practice on very simple academic signals, such as a simple discontinuity in time or a monochromatic signal (pure sinusoid). We note that it is natural to use a logarithmic scale for the scale parameter a. The visual effect is that the lines, $\tau/a =$ constant, are not straight lines, but hyperbolic curves; at the same time, the horizon $a = 0$ recedes to (minus) infinity (see Figure A.4 below).

The analysing wavelet ψ is supposed to be complex, so that we may treat separately the modulus and the phase of the transform. The scale axis, in units of $\ln a$, points downward, so that high frequencies (small a) correspond to the top of the plots, and low frequencies (large a) to the

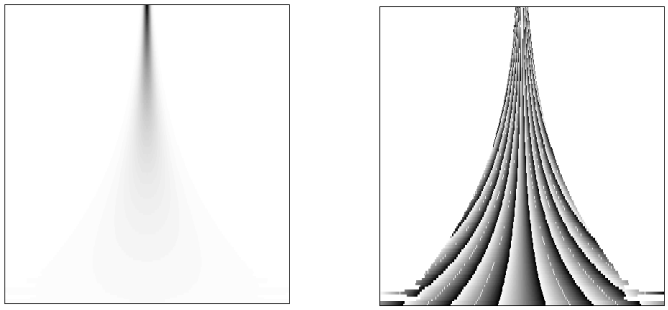

Figure A.4: Morlet WT of a δ function: (left) modulus; (right) phase.

bottom. The results are presented by coding the height of the function by density of points (12 levels of grays, from white to black). The phase is 2π-periodic. When it reaches 2π, it is wrapped around to the value 0. Thus the lines of constant phase with value $2k\pi$ are lines of discontinuity, where the density of points drops abruptly from 1 (black) to 0 (white). In addition, the functions plotted are thresholded at 1% of the maximum value of the modulus of $S(\tau, a)$. We will now analyse the two academic signals mentioned above.

(i) *A simple discontinuity*

The simplest signal is a simple discontinuity in time, at $t = t_0$, modelled by $s(t) = \delta(t - t_0)$. The WT is obtained immediately and reads

$$S(\tau, a) = a^{-1/2}\, \overline{\psi\,(a^{-1}(t_0 - \tau))}. \tag{A.13}$$

The following features may be read off Eq. (A.13):

- The phase of $S(\tau, a)$ is constant on the lines $\tau/a =$ constant, originating from the point $\tau = t_0$ on the horizon. These lines point towards the position of the singularity, like a finger.
- On the same lines of constant phase, the modulus of $S(\tau, a)$ increases as $a^{-1/2}$ when $a \to 0$, so that the singularity is enhanced. The effect is even more pronounced if one uses the L^1 normalisation.

This is illustrated on Figure A.4, which presents the modulus and phase of the WT of a δ function, using a standard Morlet wavelet (but the result is independent of the choice of ψ).

The interesting point is that this behavior is extremely robust. For instance, the 'finger' pointing to a δ-singularity remains clearly visible when the latter is superposed on a continuous signal (even if the amplitude of the δ function is too small to be visible on the signal itself), or even in the presence of substantial background noise. Similarly, the discontinuity corresponding to the abrupt onset of a signal is readily identified with the CWT (a situation common in seismology, for example). We refer to (Grossmann et al., 1990) for several spectacular examples.

This is the origin of the *edge* or *boundary effects* that we have encountered in Section 2.2.1. The first notion is that of cone of confidence or *cone of influence*. Let the wavelet ψ vanish outside the interval $I_\psi = [t_{\min}, t_{\max}]$. Then, given a point t_0 in the support of the signal, the region in which it influences the WT is the cone $\tau \in aI_\psi + t_0 = [-at_{\min} + t_0, at_{\max} + t_0]$. Thus the region of influence increases linearly with a. The effect is clearly seen in Figure 2.1: the cones of influence of the two endpoints of the spectrum are the regions where the phase of the WT differs from that of a pure sinusoid (see (ii) below). This is the region to be avoided, as discussed in Section 2.2.1.

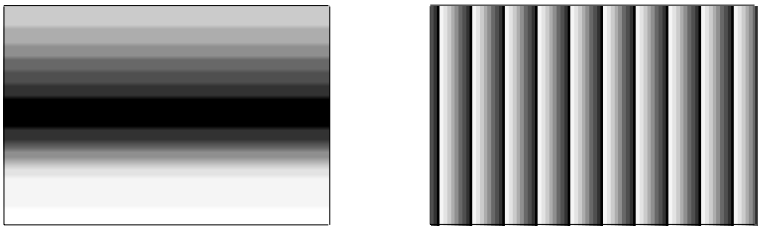

Figure A.5: Morlet WT of a single sinusoid: (left) modulus; (right) phase.

(ii) *A single monochromatic wave*

Equally simple is a single harmonic signal (monochromatic wave):

$$s(t) = e^{i\omega_s t} \;\Leftrightarrow\; S(\omega) = \frac{1}{\sqrt{2\pi}}\,\delta(\omega - \omega_s), \tag{A.14}$$

which gives

$$S(\tau, a) = \sqrt{\frac{a}{2\pi}}\,G(a\omega_s)\,e^{i\omega_s\tau} = S(a,0)\;e^{i\omega_s\tau}. \tag{A.15}$$

The same relations remain true for a real monochromatic signal, $s(t) = \sin\omega_s t$ or $s(t) = \cos\omega_s t$, if the wavelet ψ is progressive ($\Psi(\omega) = 0$ for $\omega \leqslant 0$).

Again two important properties may be read off immediately from Eq. (A.15):

• The modulus of $S(\tau, a)$ is independent of τ. Hence, the graph of $|S(\tau, a)|$ consists of horizontal bands and the profile for a fixed time τ essentially reproduces the profile of Ψ.

• The phase of $S(\tau, a)$ is linear in τ. Since the phase is 2π-periodic, the graph of $\Phi(\tau, a) := \arg S(\tau, a)$ is a linear sawtooth function:

$$\Phi(\tau, a) = \omega_s\tau \pmod{2\pi}. \tag{A.16}$$

These properties are illustrated on Figure A.5 for a single sine function analysed with a Morlet wavelet. This pattern of equidistant vertical black-to-white bands is the signature of a pure frequency signal. This can be seen already in Figure 2.1.

Both the modulus and the phase allow to determine the frequency ω_s of the signal. If the modulus of the wavelet $\Psi(\omega)$ has a single maximum for $\omega = \omega_0$, Eq. (A.15) gives immediately $\omega_s = \omega_0/a_r$, where a_r is the scale corresponding to the maximum in the profile of $|S(\tau, a)|$ for fixed τ. For instance, the (truncated) Morlet wavelet $\psi(t) = \exp(i\omega_0 t)\,\exp(-t^2/2)$ yields:

$$S(\tau, a) = \sqrt{a}\;e^{-\frac{1}{2}(a\omega_s - \omega_0)^2}\;e^{i\omega_s\tau}, \tag{A.17}$$

and the result is obvious. As for the phase, Eq. (A.16) gives, at least locally:

$$\frac{\partial\Phi(\tau, a)}{\partial\tau} = \omega_s = \frac{\omega_0}{a_r}\;. \tag{A.18}$$

A.4 The discrete wavelet transform

Notice that the discretized CWT which is used in practice, including in the present text, is totally different from the so-called *discrete WT* (DWT) that we now describe. Indeed, orthogonal bases

of wavelets may be constructed, but from a completely different approach. One starts with a *multiresolution analysis*, that is, an increasing sequence $\{V_j,\, j \in \mathbb{Z}\}$ of closed subspaces of $L^2(\mathbb{R})$ such that:

(1) $\bigcap_{j\in\mathbb{Z}} V_j = \{0\}$ and $\bigcup_{j\in\mathbb{Z}} V_j$ dense in $L^2(\mathbb{R})$;

(2) $f(t) \in V_j \Leftrightarrow f(2t) \in V_{j+1}$;

(3) There exists a function $\phi \in V_0$, called a *scaling function*, such that the family $\{\phi(t-k), k \in \mathbb{Z}\}$ of its integer translates is an orthonormal basis of V_0.

Condition (2) means that no scale is privileged. Combining (2) and (3), one gets an orthonormal basis of V_j, namely $\{\phi_{j,k}(t) := 2^{j/2}\phi(2^j t - k),\ k \in \mathbb{Z}\}$.

Each V_j can be interpreted as an approximation space. The approximation of $f \in L^2(\mathbb{R})$ at the resolution 2^j is defined by its projection onto V_j. The additional details needed for increasing the resolution from 2^j to 2^{j+1} are given by the projection of f onto the orthogonal complement W_j of V_j in V_{j+1}:

$$V_j \oplus W_j = V_{j+1}, \tag{A.19}$$

and we have, for any $j_o \in \mathbb{Z}$:

$$V_{j_o} \oplus \left(\bigoplus_{j \geqslant j_o} W_j \right) = \bigoplus_{j\in\mathbb{Z}} W_j = L^2(\mathbb{R}). \tag{A.20}$$

Then the theory asserts the existence of a function ψ, called the *mother* of the wavelets, explicitly computable from ϕ, such that $\{\psi_{j,k}(t) := 2^{j/2}\psi(2^j t - k),\ k \in \mathbb{Z}\}$ is an orthonormal basis of V_j, and thus $\{\psi_{j,k}(t),\, j, k \in \mathbb{Z}\}$ is an orthonormal basis of $L^2(\mathbb{R})$. These are the *orthonormal wavelets*. However the elements of that basis can seldom be obtained analytically, they tend to be highly irregular functions (sometimes nowhere differentiable or fractal). They are in fact obtained in an indirect fashion, through the theory of filters familiar in signal processing (see Daubechies (1992) for further details).

One may notice that this version of the WT, called the *discrete* or *dyadic* WT (DWT), is very rigid, and this explains why several generalizations have been proposed (biorthogonal wavelets, wavelet packets, ...), which are more flexible and hence more suitable for applications.

We emphasize that the DWT is totally different in spirit from the CWT, either truly continuous or discretized, and they have complementary ranges of applications:

- In the CWT, there is a lot of freedom in choosing the wavelet ψ, but one does not get an orthonormal basis, at best a frame. This is a tool for analysis and feature determination – as in MRS, or other problems where the scaling properties of the signal are unknown *a priori*, for instance in fractal analysis (Arnéodo et al., 1991).

- In the DWT, one insists on having an orthonormal basis, but the wavelet is *derived* from the postulated scaling function ϕ that generates the multiresolution analysis. Together with the generalizations mentioned above, this is the preferred tool for data compression and signal synthesis, and the most popular in the signal processing community.

More radically, one may even say that the kind of problems treated here can be solved only with the CWT, the DWT is simply not adapted to the underlying physics (Daubechies, 1992; Torrésani, 1995; Antoine et al., 2004), although it has been proposed for MRS (Neue, 1996). For instance, the algorithm for detecting spectral lines, as well as the ridge concept, rest upon a stationary phase

argument. The same is true for the determination of the instantaneous frequency (Suvichakorn and Antoine, 2008; Suvichakorn et al., 2009) and for the subtraction algorithm, that is used for removal of the water (or solvent) peak (Barache et al., 1997; Antoine et al., 2001; Antoine and Coron, 2001). Similarly, the determination of fractal exponents exploits the scaling behaviour of homogeneous functions or distributions and the covariance properties of the CWT. All these notions (and other ones) are foreign to the DWT, which is more a signal processing tool.

Appendix B

Programs

B.1 Morlet wavelet

As a convenience to the reader, we give below four MATLAB© programs: (P1) for computing the Morlet WT, (P2) for calculating the damping factor D in the case of a Lorentzian lineshape, (P3) for calculating the scaling parameter; and finally (P4) for estimating the baseline in terms of splines.

P 1 : morlet.m—Morlet wavelet transform

```
function f_mrl=morlet(in,Fs,dl,sigma,k_0,a)

% in: data
% Fs: sampling frequency (Hz)
% dl: for zero padding (times of signal's length)
% sigma:sigma for morlet
% k_0: morlet's central frequency (>5)
% a: scale
% f_mrl: morlet transform (complex number)

L     = length(in); % data length
ffs   = fftshift(fft([in zeros(1,dl*L) ]))/L;
f     = 2*pi*Fs/2*linspace(-1,1,length(ffs)); % frequency index
[F,A] = meshgrid(f,a);
mrl   = exp(- sigma^2 * (F.*A - k_0).^2 /2 ); % morlet function
[FS,A]= meshgrid(ffs,a);

f_mrl = ifft(fftshift( FS .* conj(mrl),2),[],2)*L;
```

P 2 : findD.m—Damping factor and frequency of a Lorentzian function

```
f_mrl = morlet(in,Fs,dl,sigma,k_0,a);
phi   = unwrap(angle(f_mrl),[],2); % morlet transform's phase

ohm   = diff(phi,1,2)*Fs;   % instantaneous frequency
L     = length(in); % data length
D     = -diff(log(abs(f_mrl(:,1:L+1))),1,2)*Fs; % damping factor
```

P 3 : finda.m—scaling parameter

```
% initialize parameters
err = 100;k = 1;
a_tmp = 0; % temporary scale
O = 0; % instantaneous frequency
eps = 100; % change in estimation of a
a = 0.06; % scale parameter
Fs = 800/(2*pi); % sampling frequency
T = 1/Fs;  % sample time
L = 1024;  % data length
t = (0:L-1)*T; % time index
f1= 55;f2=60; % signal frequencies
in=exp(sqrt(-1)*f1*t)+exp(sqrt(-1)*f2*t); % input signal

while abs(eps)>1e-30; %stop if change in estimation is less than 1e-30
f_mrl= morlet(in,Fs,dl,sigma,k_0,a); % morlet transform
phi  = unwrap(angle(f_mrl),[],2);
ohm  = diff(phi,1,2);
O(k) = mean(ohm(400:600))*Fs; % averaged ohm
a_tmp(k)=a;
a    = k_0/O(k);
eps  = a_tmp(k)-a;
k    = k+1;
end
```

P 4 : testSpline.m—spline as a baseline

```
a = 6e-3:1e-4:20e-3; % scaling factor
Fs= 4006.41;
T = 1/Fs;  % sample time
L = 2048;
t = (0:L-1)*T;
f1= 1056;

k_0 = 10; sigma=1;
f = Fs/2*linspace(-1,1,L); % frequency
in  = exp(sqrt(-1)*f1*t);
fss = fft(fftshift(in))/L;
fx  = min(f):1000:1.5e4;
fy  = spline(fx,0.5*rand(size(fx)),f); % spline

[F,A] = meshgrid(f,a);
mrl   = exp(- sigma^2 * (F.*A - k_0).^2 /2 );
[FS,A]= meshgrid(fss+fy,a);
f_mrl = ifft(fftshift( FS .* conj(mrl),2),[],2)*L;
```

B.2 Metabolite-based wavelets

In this section, we provide three MATLAB© programs for working with metaoblite-based wavelets: (P5) for constructing metabolite-based wavelets from discrete data, (P6) for calculating the CWT using the constructed metabolite-based wavelets, (P7) for scaling the metabolite-based wavelets as there is no analytical function to describe them.

P 5 : buildNewMetabolWavelet.m—construct metabolite based wavelets

```
  function psi = buildNewMetabolWavelet(s)

% Build wavelet from time domain signal s, based on autocorrelation.
%
% psi = buildNewMetabolWavelet(s)
%
% input
% s:        time domain signal (single signal or matrix of signals, one
%           signal per column)
%
% output
% psi:      new built wavelet or matrix of wavelets (one wavelet per column)
%
%
% Author: Christina Lemke

nRows = 2^nextpow2(size(s,1)+1);
nCols = size(s,2);
psi = zeros(nRows,nCols);
for k = 1:size(s,2)
    psi(:,k) = ifftshift(ifft(abs(fft(s(:,k),nRows).^2))); % now squared
    psi(:,k) = psi(:,k) - mean(psi(:,k));
end
```

P 6 : metacwt1d.m—1D-Continuous Wavelet Transform using metabolite-based wavelets

```
function [wt,PsiScaled] = metacwt1d(psi,signal,L,K)

% CWT (continuous wavelet transform) using wavelet psi, if psi is discrete
% and no analytical function for it is available.
%
% [wt,PsiScaled] = metacwt1d(psi,signal,L,K)
% [wt,PsiScaled] = metacwt1d(psi,signal,L,K,PsiScaled)
%
% input:
% psi:      wavelet samples in time domain (just one wavelet, no matrix)
% signal:   signal (time domain) to be analyzed
% L, K:     integer values to defines scales L/K. Usually, L would be a vector
%           and K a single value to define the scales.
%
% output:
% wt:   structure, including wavelet coefficients wt.coeff, further fields
%       may be added in the future
% PsiScaled: matrix of the scaled mother wavelet psi in the frequency domain
%
% Author: Christina Lemke, Prof. Dr. Adalberto Schuck jr.

N = length(psi)/2;
lastLength = 2^nextpow2((2*N-1)*L(end)/K);
psiScaled = zeros(length(L),lastLength);


% find scaled versions of the mother wavelet psi
for k=1:length(L)
   y=up_down_sampler(psi,L(k),K); % scale is L(k)/K
   y = (y-mean(y))./max(abs(y -5 mean(y))) * 1./sqrt(L(k)/K);
   psiScaled(k,:) = [zeros(1,ceil((lastLength-length(y))/2)), ...
   y, zeros(1,floor((lastLength-length(y))/2))];
end

PsiScaled = fft(psiScaled,[],2);


% perform CWT, calculate wavelet coefficients
nSignals = size(signal,2);
for imbl = 1:nSignals
        S = fft(signal(:,imbl),lastLength);
        [FS,A] = meshgrid(S,L./K);
        coeff = ifftshift(ifft(FS.*conj(PsiScaled),[],2),2);
        wt(imbl).coeff = coeff(:,1:N);
end
```

P 7: up_down_sampler.m—Scaling discretized wavelets to scale L/N

```
function y=up_down_sampler(x,L,N);

% Function that expands/shrinks the signal in a rate of
% L/N times, using the system described at Oppenheim and Schaffer's book
% Author: Prof. Dr. Adalberto Schuck, v. 1.2

%% First the expansion of the signal
comp=length(x);
xe=zeros(1,L*comp);
xe(1)=x(1);
for i=0:(comp-1),
    xe((L*i)+1)=x(i+1);
end

% Design the interpolation filter:
compfilt=(2*L)-1;
b=zeros(1,compfilt);
for i= 1:L,
    b(i)=i;
end
for i=1:L-1
    b(L+i)=b(L-i);
end
b=b/L;
y1=filter(b,1,xe);

%% Now the decimation part:
% Design the decimation filter:
b=fir1(128,1/N);

aux=filter(b,1,y1);
aux=aux*N;

fim=length(y1);

y=aux(1:N:fim);
```

Acknowledgements

A. Suvichakorn and C. Lemke have been (successive) Marie-Curie Research Fellows in the FAST (Advanced Signal Processing for Ultra-fast Magnetic Resonance) Marie-Curie Research Training Network (MRTN-CT-2006-035801) `http://fast-mrs.eu` from July 2007 to April 2010. A. Schuck Jr. thanks the Conselho Nacional de Pesquisa e Desenvolvimento - CNPq, Brazil, for its financial support.

The authors would like to express their gratitude to our partners: H. Ratiney, A. Bucur, and S. Cavassila from UCBL, C. Cudalbu from EPFL, and M-I. Osorio Garcia and D.Sima from KULeuven for a close collaboration and providing us the MRS signals used in the work. We would also like to thank Prof. D. Graveron-Demilly (UCBL), Prof. S. van Huffel (KULeuven), Prof. R. Gruetter (EPFL) and Prof. D. van Ormondt (TUDelft) for their invaluable advice.

Bibliography

P. Addison. *The Illustrated Wavelet Transform Handbook*. Inst. of Physics Publ., London, 2002.

S. T. Ali, J-P. Antoine, and J-P. Gazeau. *Coherent States, Wavelets and Their Generalizations*. Springer-Verlag, New York, Berlin, Heidelberg, 2000.

J-P. Antoine. Wavelet analysis of signals and images, a grand tour. *Revista Ciencias Matematicas (La Habana)*, 18:113–143, 2000.

J-P. Antoine. Wavelet analysis: A new tool in signal processing. *Physicalia Mag.*, 16:17–42, 1994.

J-P. Antoine and A. Coron. Time-frequency and time-scale approach to magnetic resonance spectroscopy. *Journal of Computational Methods Sci. & Eng. (JCMSE)*, 1:327–352, 2001.

J-P. Antoine, D. Barache, R. M. Cesar Jr., and L. da F. Costa. Shape characterization with the wavelet transform. *Signal Processing*, 62:265–290, 1997.

J-P. Antoine, A. Coron, and C. Chauvin. Wavelets and related time-frequency techniques in magnetic resonance spectroscopy. *NMR in Biomedicine*, 14:265–270, 2001.

J-P. Antoine, R. Murenzi, P. Vandergheynst, and S. T. Ali. *Two-Dimensional Wavelets and their Relatives*. Cambridge University Press, Cambridge (UK), 2004.

A. Arnéodo, F. Argoul, E. Bacry, J. Elezgaray, E. Freysz, G. Grasseau, J-F. Muzy, and B. Pouligny. Wavelet transform of fractals. In Y. Meyer, editor, *Wavelets and Applications*, pages 286–352. Masson, Paris and Springer-Verlag, Berlin, 1991.

A.R. Bahrampour, S. Izadnia, and M. Vahedi. A variational method for designing wavelets to match a specified signal. *Signal Processing*, 88:2417–2424, 2008.

D. Barache, J-P. Antoine, and J-M. Dereppe. The continuous wavelet transform, an analysis tool for NMR spectroscopy. *Journal of Magnetic Resonance*, 128:1–11, 1997.

K. L. Behar, D. L. Rothman, D. D. Spencer, and O. A. C. Petroff. Analysis of macromolecules ressonances in 1H NMR spectra of human brain. *Magnetic Resonance in Medicine*, 32(3): 294–302, 1994.

J. S. Bendat and A. G. Piersol. *Random Data: Analysis and Measurement Procedures*. Wiley, 3rd edition, 2000.

G. Beylkin and B. Torrésani. Implementation of operators via filter banks — Hardy wavelets and autocorrelation shell. *Applied and Computatonal Harmonic Analysis*, 3:164–185, 1996.

J.O. Chapa and R.M. Rao. Algorithms for designing wavelets to match a specified signal. *IEEE Transactions on Signal Processing*, 48:3395–3406, 2000.

C. Cudalbu, A. Bucur, D. Graveron-Demilly, O. Beuf, and S. Cavassila. Comparison of two strategies of background-accommodation: Influence on the metabolite concentration estimation from in vivo magnetic resonance spectroscopy data. In *Proceedings of the 29th IEEE EMBC*, pages 2077–2080, 2007.

I. Daubechies. *Ten Lectures on Wavelets*. SIAM, Philadelphia, 1992.

J. G. Daugman. Two-dimensional spectral analysis of cortical receptive field profiles. *Vision Research*, 20:847–856, 1980.

N. Delprat, B. Escudié, P. Guillemain, R. Kronland-Martinet, P. Tchamitchian, and B. Torrésani. Asymptotic wavelet and Gabor analysis extraction of instantaneous frequencies. *IEEE Transactions on Information Theory*, 38(2):644–664, March 1992.

S. Franzen. *Lecture Notes on Molecular Spectroscopy*. Department of Chemistry, NC State University, 2002. http://chsfpc5.chem.ncsu.edu/ franzen/CH795Z/.

D. Graveron-Demilly, A. Diop, A. Briguet, and B. Fenet. Product-operator algebra for strongly coupled spin systems. *Journal of Magnetic Resonance A*, 101(3):233–39, 1993.

A. Grossmann, R. Kronland-Martinet, and J. Morlet. Reading and understanding continuous wavelet transforms. In J-M. Combes, A. Grossmann, and Ph. Tchamitchian, editors, *Wavelets, Time-Frequency Methods and Phase Space (Proc. Marseille 1987), 2d ed.*, pages 2–20. Springer-Verlag, Berlin, 1990.

P. Guillemain, R. Kronland-Martinet, and B. Martens. Estimation of spectral lines with the help of the wavelet transform, applications in NMR spectroscopy. In Y. Meyer, editor, *Wavelets and applications – Proc. Int. Conf. Marseille, France, May 1989*, pages 38–60. Masson, Paris, and Springer, Berlin, 1992.

J. P. Hornak. *The Basics of NMR*. Department of Chemistry, Rochester Institute of Technology, Rochester, NY, 1997. http://www.cis.rit.edu/htbooks/nmr/.

L. Jacques, A. Coron, P. Vandergheynst, and A. Rivoldini. The YAWTb toolbox : Yet Another Wavelet Toolbox, 2007. http://rhea.tele.ucl.ac.be/yawtb.

R. Kubo. A stochastic theory of line shape. In *Advances in Chemical Physics: Stochastic Processes in Chemical Physics*, volume 15, pages 101–127, 1969.

L. T. Mainardi, D. Origgi, P. Lucia, G. Scotti, and S. Cerutti. A wavelet packets decomposition algorithm for quantification of in vivo 1H-MRS parameters. *Medical Engineering & Physics*, 24 (3):201–208, 2002.

S. Mierisov and M. Ala-Korpela. MR spectroscopy quantitation: a review of frequency domain methods. *NMR in Biomedicine*, 14(4):247–259, 2001.

J-F. Muzy, E. Bacry, and A. Arnéodo. Multifractal formalism for fractal signals: The structure function approach versus the wavelet-transform modulus-maxima method. *Physical Review E*, 47:875–884, 1993.

G. Neue. Simplification of dynamical NMR spectroscopy by wavelet transform. *Solid State Nuclear Magnetic Resonance*, 5:305–314, 1996.

A. Oppenheim, R. W. Schaffer, and J. R. Buck. *Discrete-Time Signal Processing*. Prentice-Hall, Englewood Cliffs, NJ, 2nd edition, 1999.

A. Papoulis and S. U. Pillai. *Probability, Random Variables and Stochastic Processes*. McGraw-Hill, Inc., NY, 4th edition, 2002.

J. B. Poullet, D. M. Sima, A. W. Simonetti, B. De Neuter, L. Vanhamme, P. Lemmerling, and S. Van Huffel. An automated quantitation of short echo time MRS spectra in an open source software environment: AQSES. *NMR in Biomedicine*, 20:493–504, 2007.

J. B. Poullet, D. M. Sima, and S. Van Huffel. MRS signal quantitation: A review of time- and frequency-domain methods. *Journal of Magnetic Resonance*, 195:134–144, 2008.

H. Rabeson, H. Ratiney, C. Cudalbu, S. Cavassila, E. Capobianco, R. de Beer, D. van Ormondt, and D. Graveron-Demilly. Signal disentanglement in *in vivo* MR spectroscopy by semi-parametric processing or by measurement? In *Proceedings of the Annual Workshop on Circuits, Systems and Signal Processing (ProISC)*, pages 176–183, The Netherlands, 2006. IEEE Benelux.

H. Rabeson, H. Ratiney, F. Fauvelle, C. Cudalbu, S. Cavassila, A. Bernard, P. Giraudon, D. van Ormondt, and D. Graveron-Demilly. Quantitation for in vivo and ex vivo NMR spectroscopy. *Journal of Optoelectronics and Advanced Materials*, 9(1):505–511, 2007.

H. Rabeson, E. Capobianco, R. de Beer, D. van Ormondt, and D. Graveron-Demilly. Lineshape estimation in *in vivo* MRS without using a reference signal. In *Proc. ISMRM 2008*, Toronto, 2008.

N. Saito and G. Beylkin. Multiresolution representations using the auto-correlation functions of compactly supported wavelets. *IEEE Transactions on Signal Processing*, 41:3584–3590, 1993.

H. Serrai, L. Senhadji, J. D. de Certaines, and J. L. Coatrieux. Time-domain quantification of amplitude, chemical shift, apparent relaxation time T_2^*, and phase by wavelet-transform analysis. application to biomedical magnetic resonance spectroscopy. *Journal of Magnetic Resonance*, 24:20–34, 1997.

M.J. Shensa. The discrete wavelet transform: Wedding the à trous and the Mallat algorithms. *IEEE Transactions on Signal Processing*, 40:2464–2482, 1992.

D.M. Sima, M.I. Osorio Garcia, J. Poullet, A. Suvichakorn, J.-P. Antoine, S. Van Huffel, and D. van Ormondt. Lineshape estimation for magnetic resonance spectroscopy (mrs) signals: self-deconvolution revisited. *Measurement and Science Technology*, 20, 2009.

A. Suvichakorn and J.-P. Antoine. Analyzing NMR spectra with the Morlet wavelet. In *Proc. EUSIPCO 08*, Lausanne, Switzerland, 2008.

A. Suvichakorn, H. Ratiney, A. Bucur, S. Cavassila, and J-P. Antoine. Toward a quantitative analysis of *in vivo* proton magnetic resonance spectroscopic signals using the continuous Morlet wavelet transform. *Measurement and Science Technology*, 20:paper #104029, 2009.

B. Torrésani. *Analyse continue par ondelettes*. InterEditions & CNRS Editions, Paris, 1995.

R. De Valois and K. De Valois. *Spatial Vision*. Oxford Univ. Press, New York, 1988. See in particular Chap.4, pp. 137–143.